Probing Quantum Confinement at the Atomic Scale with Optically Detected Nuclear Magnetic Resonance

Thesis by

James G. Kempf

In Partial Fulfillment of the Requirements

for the Degree of

Doctor of Philosophy

California Institute of Technology

Pasadena, California

2001

(Submitted September 20, 2000)

Acknowledgments

I am foremost grateful for those things that conspired to bring me to Caltech, where I have benefited from a wonderful opportunity to work with many talented scientists. The encouragement and confidence that my parents have always expressed to me provided the chance. The research and professional guidance I received as an undergraduate at Fredonia from Prof. Dan Jelski and other members of the chemistry faculty opened my eyes to the possibilities of a scientific career. Many others from as far back as high school (and beyond), and certainly including those with whom I have interacted non-academically, have taught me valuable and cherished lessons along the way. These opportunities have been wonderfully fulfilled in working with Prof. Daniel Weitekamp at Caltech. Dan has afforded me the freedom to struggle and succeed in an environment full of ideas and creativity. I greatly appreciate his scientific openness and the resulting flow of excitement and varied interests he brought to the group. Furthermore, Dan's willingness to send me out in the world to put a face on our research introduced me to great scientists beyond Caltech, gave me frequent reality checks on the quality and direction of my research and often stressed me out in the best possible way.

It has been my good fortune to work with many talented people who were similarly drawn by Dan's style of research. The trio of Paul Carson, John Marohn and Len Mueller were the foundation that encouraged me to join the Weitekamp group nearly six years ago. They worked hard, loved their research and took the time to listen to and answer many questions I posed them. It is my great pleasure to know that our scientific discussions will continue for years to come. I have shared the most time at Caltech with Lou Madsen and Gary Leskowitz, and that time never wanted for quality. Lou and Gary were great listeners to my ideas, struggles and successes in research, and provided me many of their own ideas to help out along the way, all the while inspiring and exciting me with their own research. Michael Miller has also been an excellent coworker in the same regard, but in his case, in projects on which we directly collaborated. Mike worked hard to lay much of the theoretical groundwork for our optical NMR studies. This gave me the freedom to play in lab and paid great dividends when then left to understand the results. I am additionally glad to see that the next generation of Bruce Lambert, Ramez

Elgammal and Valerie Norton is already running with the ball. Bruce provided me my first opportunity to pass a scientific torch and it is great to see how much he has learned, but well beyond that, Bruce has taught much to me with his considerable knowledge and drive, while he and Ramez have given the optical NMR apparatus a new life for future experiments. Special thanks go to Bruce, Ramez and Valerie for putting up with always-busy me over the last year, but also for making that time at work and away at conferences enjoyable.

Teaching experiences gained at Caltech are also of great value to me. In interaction with students as a TA, I am certain that I learned far more than I ever was able to teach. For this I am grateful to many motivated and supremely talented students I have encountered, and especially to Prof. Aron Kuppermann, who accepted my request to TA has class only one year after I had scored (almost) unspeakably as a student in the same. I thank Prof. John Baldeschwieler for similar confidence expressed in me and for the opportunity he granted me to instruct in his undergraduate course.

Many friendships at Caltech have been very important to me. Adrian Ponce and I started out together a bit uncertain as to how all of this grad-school business would play out, and, finally, we *found* the answer. I admire Adrian's spirit and cherish my time spent with him and Xenia Amashukeli. Claudine Chen has shared so much of her time and energy with me in the last few years, and I am especially grateful for the quality of that time. I feel that work has made this last year, in particular, hard, but her interjection with both assistance at work and fun times away, helped make this hard year one I will remember as great. Classmates, housemates and friends Helen Blackwell, Dave Lynn, Chantal Morgan and Mary Gin also helped to keep me sane in the beginning and happy over the years. Helen, what other Indians fan would ever root with me for the Yankees? Thanks. I also thank Jennifer Herek for many of my happiest memories from the early years at Caltech and for her continued friendship. While Jennifer wrote her thesis and I struggled to become a candidate for the Ph.D., stress could have ruled our worlds, but she helped me navigate a much better path, for which I will always be grateful. Many other co-dwellers of the Noyes subbasement have been great friends. For this I thank all of the Weitekamp group, and Christine Kaestle, Mary Mason, Arezoo Miller, Ravi Abrol,

Dmitri Kosakovski, Stephanie Rogers, Schubert Soares, Jennifer Johnson, and a host of Zewail group folks. Additionally, the Kicking Buck crew helped me clumsily learn a great game and provided many happy moments. Special thanks to Dmitri for roping me in to play long ago, to Gabriel Brandt for taking the team's helm and for setting the hook and, I must say, to Adrian for the bicycle kicks. Ravi, Catherine Baker, Isaac Carrico Derek Debe, Ivan and Jane Dmochowski, Akif Tezcan, and Niki Zacharias have been invaluable friends and teammates on and off the field. Also, great friends and reminders to me of my favorite, but often-neglected sport, running buddies Ivan, Liz Boer, Stephen Glade, Russel Todres and Brendan Crill have pushed me hard on the roads. I needed it.

Finally, in addition to my parents, I would like to thank the rest of my family. Through all this distance you have always felt close, given me a good phone call at the right time and had faith that I would get the job done right out here. These things mean very much to me, as do each of you.

Abstract

Near-band-gap circularly polarized excitation in III-V semiconductors provides spin-polarized electrons that transfer spin order to lattice nuclei via fluctuations in the contact hyperfine interaction. This process of optical nuclear polarization and the complementary technique of optical detection of nuclear magnetic resonance (NMR) provide extreme sensitivity enhancement and spatial selectivity in structured samples, enabling collection of NMR spectra from samples such as single quantum wells or dots containing as few as ~10^5 nuclei.

Combining these advances with novel techniques for high spectral resolution, we have probed quantum-confined electronic states near the interface of a single epitaxially grown $Al_{(1-x)}Ga_xAs/GaAs$ ($x = 0.36$) heterojunction. Using a novel strategy that we refer to as POWER (perturbations observed with enhanced resolution) NMR, multiple-pulse time suspension is synchronized with bandgap optical irradiation to reveal spectra of effective spin Hamiltonians that are *differences* between those of the occupied and unoccupied photoexcited electronic state. The underlying NMR linewidth is reduced by three orders of magnitude in these experiments, enabling resolution of an asymmetric line shape due to light-induced hyperfine interactions. The results are successfully fit with the coherent nuclear spin evolution and relaxation theoretically expected for sites distributed over the volume of an electronic excitation weakly localized at a point defect. This analysis establishes a one-to-one relationship, which can be used to follow nuclear spin diffusion, between optical Knight shift and the radial position of lattice nuclei.

We have also introduced POWER NMR techniques to characterize the change in electric field associated with cycling from light-on to light-off states via a linear

quadrupole Stark effect (LQSE) of the nuclear spins. Simulations of these NMR spectra in terms of the radial electric fields of either donor-bound electrons or excitons indicate differences, where the bound-exciton model provides a significantly better fit to the data. The same spin physics enabled our measurement of the heterojunction interfacial field, which we find to be less than 1.3 kV/cm at the sites responsible for optical NMR. Other simulations show the promise of optical NMR as a tool in future studies aimed at atomic-level characterization of quantum-confined systems such as quantum dots and wells.

Table of Contents

Standard Symbols, Terms and Abbreviations

NMR	nuclear magnetic resonance
ONMR	optical nuclear magnetic resonance
LBD	Larmor-beat detection
PL	photoluminescence
CP	circular polarization
LQSE	linear quadrupole Stark effect
rf	radiofrequency
FWHM	full width at half max

Constants and Parameters

$\mathbf{B}_0$	static magnetic field in NMR experiments
B_1	rf magnetic-field amplitude in NMR experiments
ω_0	nuclear Larmor frequency (rad s^{-1})
γ	nuclear gyromagnetic ratio
P_n	nuclear spin polarization (Zeeman order)
T_1, T_2	time constants of longitudinal, transverse nuclear spin relaxation
$T_{1\rho}$	time constant of relaxation of nuclear alignment from a spin-locking axis
$T_{1\rho}^{B}$	time constant of background nuclear spin relaxation from spin-locking axis
T_1^{opt}	time constant of optically induced (hyperfine) nuclear spin relaxation
τ_c	correlation time of fluctuations in the contact-hyperfine interaction
$J^{(1)}(\omega)$	spectral density of fluctuations in the contact-hyperfine interaction at $\omega/2\pi$
t_1	indirect dimension of NMR time evolution in a pointwise-detected experiment
t_2	duration of the spin-locked optical detection period
I_x, I_y, I_z	Cartesian components of dimensionless nuclear spin angular momentum operators
$T_{k,q}$	spherical-tensor nuclear spin operator
T_{1e}	electron spin relaxation time
T_{1e}^{*}	effective longitudinal electron spin relaxation time accounting for interruption of spin relaxation by radiative recombination
$\mathbf{B}_n^{\alpha}$	nuclear hyperfine field of a particular isotope α
$\mathbf{B}_n^{sig,ref,misc}$	hyperfine fields of the NMR signal nucleus, the reference nucleus used for LBD and any miscellaneous nuclei not filling either of these roles
χ_α	fractional isotopic abundance of the nuclear species α
σ_+, σ_-	right, left circularly polarized components of PL
ρ	circular polarization of PL

$\mathbf{B}_{\wedge}$	transverse field responsible for Hanle effect depolarization of PL
g_0	free-electron g factor
$\Psi(\mathbf{r})$	wave function of localized electron as a function of position $\mathbf{r}$
$\psi(\mathbf{r})$	envelope wave function of localized electron
d_i	modulus squared of electron Bloch function at i^{th} nucleus in GaAs lattice
Γ	occupancy of the electronic localization site
$\langle S \rangle$	time-averaged photoelectron spin
P_e	electron spin polarization
J_e, J_h	total spin angular momentum of photoexcited electron, hole
C_{14}	Bloembergen's constant relating induced field gradient to an electric field
E_{100}, E_{001}, E_{001}	electric field components along GaAs [001], [010], and [001] crystal axes
Q	nuclear quadrupole moment
$V_{k,q}$	spherical-tensor components of the electric field gradient tensor

Common-Usage Physical Constants

ε_0	permittivity of free space
μ_0	permeability of free space
μ_B	nuclear Bohr magneton
$\hbar$	Planck's constant divided by 2π
e	unit of electron charge

List of Figures

List of Tables

I. Introduction

Nuclear magnetic resonance (NMR) spectroscopy is a technique that rose from the independent basic research of physicists Edward M. Purcell[1] and Felix Bloch.[2] The pair later shared the 1952 Nobel prize in physics for their coincident discovery of NMR, which has since grown into the most widely used spectroscopic method, with applications in biology, chemistry, physics and medicine. For all its utility, however, the traditional approach to NMR experiments suffers from its inherent low sensitivity and its restriction as a probe of only bulk material properties, rather than local features in structured samples. These shortcomings are especially apparent with the ever-increasing demand for characterization of the tiny and ordered realms of nature, such as single-crystal proteins, and fabricated nanoscale materials, such as layered epitaxial semiconductors.

Optical NMR (ONMR) is one successful approach towards overcoming the noted limitations of the traditional spectroscopic technique. The key to ONMR is the coupling of photoexcited electrons to nuclear spin degrees of freedom. Its most widespread application is to III-V semiconductors such as GaAs, where circularly polarized optical excitation provides spin-polarized conduction-band electrons, which in turn transfer corresponding order to lattice nuclei.[3,4] This process of optical nuclear polarization (ONP) adds several orders of magnitude in sensitivity to the NMR experiment by providing a larger nuclear moment to measure. Additionally, photoluminescence (PL) in III-V's exhibits polarization response[4-9] and/or frequency shifts[10-12] according to the spin state of the same nuclei. Thus, an NMR signal, traditionally detected as a weak radiofrequency (rf) emission of the spin system, can be effectively amplified by encoding it in a much more energetic optical signal, yielding a further increase in

sensitivity.[5,7-9,11-13] The combination of ONP and optical detection has supplied signal-to-noise enhancement by a factor of up to 10^{12} in GaAs materials.[11,12] Furthermore, each of these processes provides spatial selectivity due to the locality of the electron-nuclear interactions on which they depend.

The ONMR experiment is a powerful probe of electronic states confined to quantum wells (QWs) and dots, and at point defects and material interfaces. These systems exhibit fundamental quantum behavior that is often unexpected,[14] and which can play important roles in device physics. However, orders-of-magnitude enhancement of spectral resolution over previous ONMR experiments[5,7-9,11,13,15-23] is needed to approach atomic-scale spatial resolution by NMR. One hurdle to improving resolution is particular to ONMR methodology: perturbation of the nuclear spin system by the optical detection process. Buratto, *et al*.[8] solved this problem by implementing a novel detection scheme that enabled separation of the ONP, NMR evolution and optical detection periods on the experiment timeline. Marohn, *et al*.[9] subsequently incorporated their more versatile Larmor beat detection (LBD) method in this time-sequenced approach.

A more general obstacle to obtaining high resolution in solid-state NMR is due to strong dipolar couplings between neighboring nuclei, which yield linewidths several orders of magnitude broader than those in liquid-state experiments. In this thesis, a novel methodology is presented which attacks this problem by synchronizing resonant irradiation of the nuclear spins with cyclic perturbations of the sample during the NMR evolution period.[24-26] Using this approach, which we refer to as POWER (perturbations observed with enhanced resolution) NMR, the sequence of rf pulses and cycled

perturbations is arranged in such a way that line broadening due to magnetic field inhomogeneity and unresolved spin couplings is removed, while the spin Hamiltonian due to the perturbation interaction remains as the dominant source of spectral structure.

The remainder of this thesis is organized as follows. In Section A of the current chapter, the basic physics and apparatus of traditional NMR spectroscopy are introduced. The photophysics of ONP and optical detection of NMR in III-V semiconductors are presented in Section B, while multiple-pulse POWER NMR techniques are detailed in Section C. Chapter 2 contains a detailed description of our ONMR experimental procedures and apparatus. In Chapter 3, I discuss experiments where optical spectroscopy was used to probe the so-called *H*-band photoluminescent states in an AlGaAs/GaAs heterojunction. These states have received recent attention due to their relation to the material interface in high-quality epitaxially grown samples,[27-30] and are relevant to our ONMR investigations of such a sample, including, in Chapter 3, characterization of the electric field at the heterojunction interface via a linear quadrupole Stark effect (LQSE) of the lattice nuclei. Additionally, in Chapter 4, the first experimental applications of the POWER NMR approach are detailed, in which we have obtained a radially resolved image of the electron wave function corresponding to the *H*-band states and characterized the combined electron and hole distributions through their electric field. Finally, in Chapter 5, I present a third application of POWER NMR, in which an electric field applied normal to the plane of an *n*-type GaAs QW induces a polarization response in the quantum-confined carrier population. Simulations of this response in the quantum-confined dimension indicate the practicality of measuring the polarization field with atomic-layer resolution in an isotopically diluted 10 nm QW.

A. Nuclear Magnetic Resonance Spectroscopy

Nuclear magnetic resonance (NMR) experiments probe the properties of atomic nuclei and their local environment by recording the transitions between nuclear spin energy levels. The energy separation of these levels is determined primarily by the Zeeman interaction, which is linear in the strength of an applied magnetic field $\mathbf{B}_0$, as depicted in Fig. 1.1(a). The magnitude of the Zeeman splitting for a given value of $\mathbf{B}_0$ is a property of the nuclear isotope alone. However, the local environment of the nucleus is also probed by NMR, since the *observed* energy splitting also reflects the response of the local electronic system to the applied field, the magnetic coupling of the nucleus to nearby spins, and, for a nucleus with spin $I \geq 1$, the orientation-dependent coupling of the nucleus to an electric field gradient. Because NMR probes this diverse set of observables, it is the premier spectroscopic tool for chemical and structural analysis at the atomic level.

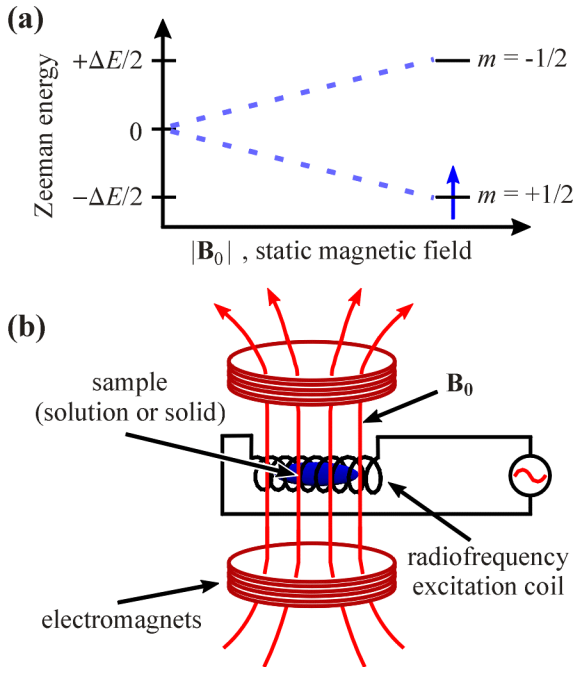

FIG. 1.1 **(a)** Zeeman energy splitting of nuclear spin states, which are labeled according to the allowed values of m, the projection of the dimensionless nuclear spin angular momentum $\mathbf{I}$ along $\mathbf{B}_0$, for the case where $I = |\mathbf{I}| = \frac{1}{2}$. **(b)** Basic NMR experimental apparatus.

The basic experimental apparatus used in NMR experiments is shown in Fig. 1.1(b). Typically, electromagnets provide a large, homogeneous $\mathbf{B}_0$ at the sample position, while a coil of conducting wire surrounding the sample serves as the source of

radiofrequency (rf) irradiation used to induce NMR transitions. An oscillating voltage applied across the coil circuit at angular frequency ω provides an identically time-dependent magnetic field with amplitude $2B_1$ directed orthogonal to $\mathbf{B}_0$. When the irradiation frequency matches the nuclear Larmor frequency

$$\omega_0 = \Delta E / \hbar = -\gamma_n B_0 , \tag{1.1}$$

where $\hbar$ is Planck's constant h divided by 2π and γ_n is the nuclear gyromagnetic ratio, it induces transitions between Zeeman energy levels. This is the condition known as resonance. The static field must be homogeneous over the sample volume in order to ensure that the width and relative energies of spin transitions for a set of like nuclei are determined only by their local environment, as opposed to variation of the Zeeman interaction across the sample.

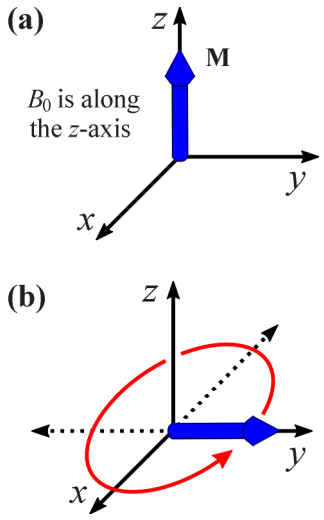

FIG. 1.2 **(a)** The nuclear magnetic moment **M** resulting from net alignment of the spins along $\mathbf{B}_0$. **(b)** Precession of **M** about $\mathbf{B}_0$ following a $\pi/2$ pulse.

The thermal population difference between spin energy levels, which determines the net strength of absorption or emission, increases with B_0; therefore, high fields are advantageous in the NMR experiment. However, in modern NMR spectroscopy, simple absorption or emission measurements in the frequency domain are replaced by a time-domain experiment, where pulses of broadband irradiation excite coherent spin transitions that yield subsequent time evolution of the nuclear magnetic moment **M**.

Thermal populations of the spin-$\frac{1}{2}$ Zeeman levels exhibit net alignment along $\mathbf{B}_0$, yielding a corresponding nuclear magnetic moment,

$$\mathbf{M} = N \gamma_n \hbar \langle \mathbf{I} \rangle , \tag{1.2}$$

in the same direction, as shown in Fig. 1.2(a), where N is the number of spins in the ensemble and $\mathbf{I}$ is the dimensionless nuclear spin angular momentum operator. A short, resonant rf pulse turns $\mathbf{M}$ away from $\mathbf{B}_0$ and, in the case where the pulse duration t_p is such that $(-\gamma_n B_1 t_p) = \pi/2$, this rotation is by 90° and places $\mathbf{M}$ in the transverse plane. Following this $\pi/2$ pulse, $\mathbf{M}$ precesses about $\mathbf{B}_0$, as shown in Fig. 1.2(b), a time-dependence that is traditionally detected via Faraday Law induction of a voltage proportional to $\frac{d}{dt}\mathbf{M}$ in the nearby coil. This signal voltage is given by

$$S(t) = A \cos(\omega_0 t) e^{-t/T_2} \tag{1.3}$$

where A is a scaling factor proportional $\mathbf{M}$, $\omega_0 = \Delta E / \hbar$ is the nuclear Larmor frequency and T_2 is the transverse nuclear spin relaxation constant. The Larmor frequency of precession exactly matches the frequency that corresponds to the energy splitting between nuclear spin levels. This suggests an equivalence of time and frequency-domain NMR signals, which is made clear by executing a Fourier transformation of the time-domain NMR signal. The result of this operation is illustrated in Fig. 1.3, where $S(t)$ transforms into a single Lorentzian peak at ω_0 in the frequency domain and with a full width at half max (FWHM) of $(\pi T_2)^{-1}$.

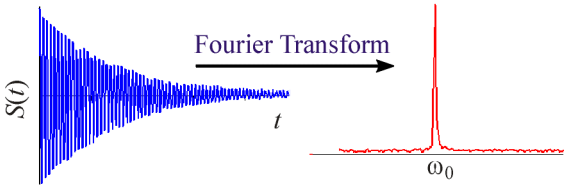

FIG. 1.3 An example time-domain NMR signal $S(t)$, which is converted into a frequency domain signal shown at right by the mathematical operation known as Fourier transformation.

The greatest advance provided with time-domain NMR is the ability to coherently control the orientation of **M** over the course of the experiment.[31-33] Sequences including trains of resonant rf pulses with various phase and duration can be arranged to yield a combination of free and driven evolution of the spins that averages the effects of certain interactions to zero, placing others in greater prominence. With such control, a tremendous variety of multiple-pulse sequences have been designed to narrow NMR spectral features. This provides otherwise inaccessible spectroscopic resolution, while additionally sorting spin interactions according to the interests of experimenter. In contrast, frequency-domain NMR experiments are almost completely lacking in this sophistication.

Finally, two factors that determine the sensitivity in a traditional NMR experiment are highlighted in the basic overview above: the degree of thermal spin polarization and the inductive coupling of the time-dependent **M** to a detection coil. Thermal polarization of nuclear spins is notoriously weak, as dictated by the small energy splitting dominated by the Zeeman interaction. Consider the example of ^{71}Ga ($I = \frac{3}{2}$), which has the largest splitting among the isotopes present in GaAs. The Zeeman polarization of a spin-$\frac{3}{2}$ nucleus is

$$P_n = \frac{\frac{3}{2} + \frac{1}{2}\zeta - \frac{1}{2}\zeta^2 - \frac{3}{2}\zeta^3}{\frac{3}{2} + \frac{1}{2}\zeta + \frac{1}{2}\zeta^2 + \frac{3}{2}\zeta^3}, \tag{1.4}$$

where $\zeta = e^{-(\hbar\omega_0/k_BT)}$, k_B is the Boltzmann constant and T is the temperature. Even in a large 11.75 T field at $T = 2$ K, this yields only 0.5% ^{71}Ga spin polarization. In contrast, ONP in bulk GaAs, which does not depend on high field, has yielded ^{71}Ga polarization of ~10% at 2 K with $B_0 \sim 250$ mT,[9] while still greater optically induced polarization is

possible in QW samples.[17] Additionally, inductive coupling of the spins to the detection coils is much weaker than hyperfine coupling between the nuclear spins and photoexcited electrons. The latter can be used to encode an NMR signal into the PL response of such electrons with a coupling efficiency that is dramatically increased relative to the inductive approach. In the following section, I present the basic III-V photophysical processes that govern ONP, for generation of large, nonequilibrium **M**, and optical detection, for more efficient detection of its evolution.

B. Optical NMR Methodology

As noted above, two of the most common pitfalls of traditional NMR spectroscopy are low signal sensitivity and poor spatial selectivity for samples that are inhomogeneous or structured. The *sensitivity* of traditional solid-state NMR spectroscopy is such that a minimum of $\sim 10^{17}$ spins are required to obtain a discernable NMR signal, whereas individual semiconductor quantum dots, for example, may contain only $\sim 10^{5}$ spins. The failing of traditional NMR as a *spatially selective* technique resides in its inability to separate the signal of scarce local regions within a sample from that of the same nuclei in the bulk material, thus, possibly obscuring the signal of interest with a large, mundane companion. The utility of ONP and optical detection for defeating these limitations was noted above. In this section, I describe the photophysical processes that are generally relevant for ONP and optical detection in III-V semiconductors with the zincblende crystal structure, which excludes GaN. The time-sequenced and Larmor-beat-detection ONMR methodologies, which complete the picture of techniques developed earlier and used for all experiments presented in this thesis, are also described.

1. Optical Nuclear Polarization

The optical selection rules and subsequent photoelectron spin relaxation that govern ONP in bulk III-V semiconductors is depicted in Fig. 1.4. The two-step process of ONP is a transfer of angular momentum from circularly polarized (CP) photons to photoexcited electrons and, finally, to lattice nuclei. The first step is the production of spin-polarized conduction-band electrons by a CP excitation beam with unit propagation vector $\hat{n}_e$ along the direction of an external magnetic field $\mathbf{B}_0$. The spin-polarization follows from conservation of angular momentum and the oscillator strengths of allowed transitions, as shown at the right of Fig. 1.4.[4] The valence holes and conduction electrons thus generated are labeled in the figure according to their spin-plus-orbital angular momentum, J_e and J_h, respectively. The difference (J_e - J_h) for a given electron-hole pair must be equal to the unit of angular momentum supplied by the exciting photons. Thus, right CP light (σ_+), which carries +1 unit of angular momentum projected along $\mathbf{B}_0 // \hat{n}_e$, is capable of generating electron-hole pairs with $(J_e, J_h) = (-\frac{1}{2}, -\frac{3}{2})$ or $(+\frac{1}{2}, -\frac{1}{2})$. However, the matrix elements that determine the relative strengths of these transitions favor generation of the $(-\frac{1}{2}, -\frac{3}{2})$ pair in a 3:1 ratio. This ratio results in an initial electron spin polarization

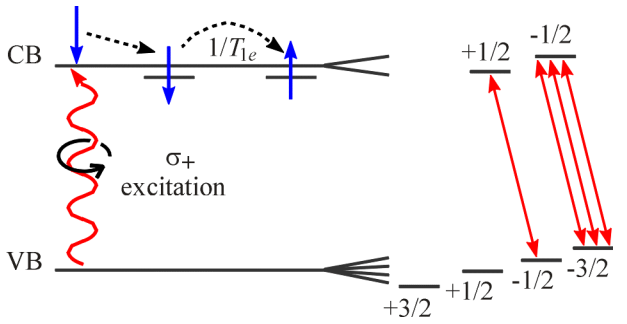

FIG. 1.4 The basic photophysical processes underlying ONP in a III-V semiconductor. Valence-band (VB) and conduction-band (CB) sublevels are shown at right with labels denoting spin-plus-orbital angular momentum projected onto the axis of $\mathbf{B}_0 // \hat{n}_e$. The number of arrows connecting electron hole pairs at right indicates the relative strength of corresponding allowed transitions.

$$\mathbf{P}_e^{init} = \frac{N_{+1/2} - N_{-1/2}}{N_{+1/2} + N_{-1/2}} = -\tfrac{1}{2}\,\hat{n}_e, \tag{1.5}$$

which, at 2 K in a 250 mT field, is far greater in magnitude than the thermal value of ~ 0.02. Including electronic relaxation and allowing arbitrary circular polarization,

$$\vec{\rho}_{ex} = \frac{\sigma_+ - \sigma_-}{\sigma_+ + \sigma_-}\,\hat{n}_e = \rho_{ex}\,\hat{n}_e, \tag{1.6}$$

of the excitation beam provides the more general result[6]

$$\mathbf{P}_e = \xi\left(T_{1e}/T_{1e}^*\right)\rho_{ex}\,\hat{n}_e, \tag{1.7}$$

where $\xi = \frac{1}{2}$, according to the selection rules for bulk III-V materials, T_{1e} is the electron spin relaxation time, and

$$T_{1e}^* = \left(T_{1e}^{-1} + \tau_r^{-1}\right)^{-1}, \tag{1.8}$$

where τ_r^{-1} is the radiative recombination rate. We also note that in a region of a III-V that exhibits quantum confinement, such as a QW, the degeneracy of light ($J_h = \pm\frac{1}{2}$) and heavy ($J_h = \pm\frac{3}{2}$) holes is lifted.[34] When the energy splitting of these holes is sufficient for resolved excitation, production of only $(J_e, J_h) = (+\frac{1}{2}, +\frac{3}{2})$ electron-hole pairs is possible, yielding $\xi = 1$, and thus electrons which are even further from thermal equilibrium, as is favorable for ONP.

The final step in the ONP process is the transfer of the photoelectron spin order to lattice nuclei via contact hyperfine coupling, which is most efficient where photoelectrons localize at shallow trapping sites in the crystal lattice. The Hamiltonian governing this interaction between a single electron-nuclear pair is

$$\mathcal{H}_{hf}^{C,\,i} = -\tfrac{2}{3}\,\Gamma\,\mu_0\,g_0\,\mu_B\,\gamma_n^i\,\left|\Psi(\mathbf{r}_i)\right|^2\,\mathbf{I}^i\cdot\mathbf{S}, \tag{1.9}$$

in units of Hz, where Γ is occupancy of the electronic localization site, **S** is the dimensionless electron spin angular momentum operator, g_0 is the free-electron g-factor,[1(a)] and $\Psi(\mathbf{r}_i)$ is the value of the electronic wave function at the i^{th} nuclear center. The spectral density of fluctuations in $\mathcal{H}_{hf}^{C,i}$ at the difference between the electron and nuclear Larmor frequencies induces mutual electron-nuclear spin flips, thus transferring spin order into the nuclear population. Such fluctuations may be due, for example, to scattering of the electron spin by free electrons.[6]

At low temperatures, where thermal phonons are scarce, the process described above dominates photoelectron spin relaxation, and the prescribed optical pumping yields ONP. Furthermore, according to Eq. (1.9), the effects of ONP are appreciable only for nuclei near the center of electronic localization, since $\Psi(\mathbf{r}_i)$ vanishes elsewhere. This provides spatial selectivity in the optical NMR experiment. Finally, it is noteworthy that spin-polarized holes are also produced in the above scheme; however, as concerns the ONMR experiment, the effect of the hole spins is generally negligible, since their hyperfine coupling to lattice nuclei is relatively weak and their spin exhibits rapid thermalization.[35,36]

2. Optical Detection of NMR via the Hanle Effect

The Hanle effect is the variation of PL polarization in response to a magnetic field $\mathbf{B}_{\wedge}$ oriented transverse with respect to the direction of electron spin polarization.[37] Its existence in III-V semiconductors may be understood beginning with the optical selection rules presented above in the context of ONP. As indicated in Fig. 1.5, the radiative decay

---

[1(a)] Paget, *et al*[6] have discussed the appropriateness of using the free-electron g-factor, rather than the

of spin-down (up) conduction-band electrons yields a 3:1 (1:3) ratio of σ_+ to σ_- photons. Thus, spin-polarized conduction-band electrons generated by CP excitation yield nonvanishing CP of luminescence ρ. Using an argument similar to that used for excitation in Section B.1 of this chapter, we obtain

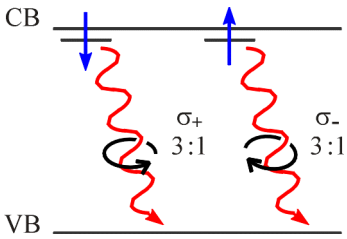

FIG. 1.5 The relation between the CP of luminescence ρ, and the photoelectron spin state.

$$\rho = \xi \mathbf{P}_e \cdot \hat{n}_d = 2\xi \langle \mathbf{S} \rangle \cdot \hat{n}_d , \tag{1.10}$$

where $\hat{n}_d$ is the unit propagation vector of the detected light. The effect of a transverse field $\mathbf{B}_\wedge$ on ρ is qualitatively understood according to the precession of $\mathbf{S}$ about the field, which reduces $\langle \mathbf{S} \rangle$, and hence ρ, according to Eq. (1.10).

A quantitative picture of the Hanle effect is derived from the steady-state solution to electron the Bloch equation

$$\frac{d}{dt}\langle \mathbf{S} \rangle = T_{1e}^{-1}\left(\langle \mathbf{S} \rangle - \langle \mathbf{S}_0 \rangle\right) - \gamma_e \left(\langle \mathbf{S} \rangle \times \mathbf{B}\right), \tag{1.11}$$

which describes the time evolution of $\langle \mathbf{S} \rangle$ in a magnetic field $\mathbf{B}$. In this expression,

$$\langle \mathbf{S}_0 \rangle = \tfrac{1}{2}\xi \left(T_{1e} / T_{1e}^*\right) \rho_{ex} \hat{n}_e \tag{1.12}$$

is the steady-state photoelectron spin [See Eq. (1.7)], $\gamma_e = g^* \mu_B / h$ is the electron gyromagnetic ratio, as determined by the effective conduction-band g-factor, $g^* = -0.44$, and equivalent longitudinal and transverse spin relaxation times are assumed. The steady-state solution[38] to Eq. (1.11) is valid when

---

conduction-band value, in Eq. (1.9).

$$\left| \frac{1}{B} \frac{dB}{dt} \right| \ll T_{1e}^{-1}. \tag{1.13}$$

Keeping this in mind, and inserting the steady-state result into Eq. (1.10) yields

$$\rho = \rho_0 \frac{B_H^{\,2} (\hat{n}_e \cdot \hat{n}_d) + B_H \mathbf{B} (\hat{n}_e \times \hat{n}_d) + (\mathbf{B} \cdot \hat{n}_e)(\mathbf{B} \cdot \hat{n}_d)}{B_H^{\,2} + \mathbf{B}^2}, \tag{1.14}$$

where

$$\rho_0 = \xi^2 \left(T_{1e} / T_{1e}^* \right) \rho_{ex} \tag{1.15}$$

is the initial polarization, and

$$B_H = \left(\gamma_e T_{1e} \right)^{-1} \tag{1.16}$$

is known as the intrinsic Hanle width. Taking $\hat{n}_e$ and $\hat{n}_d$ to be mutually parallel to the component $\mathbf{B}_{//}$ of $\mathbf{B} = (\mathbf{B}_{//} + \mathbf{B}_\wedge)$, Eq. (1.14) reduces to

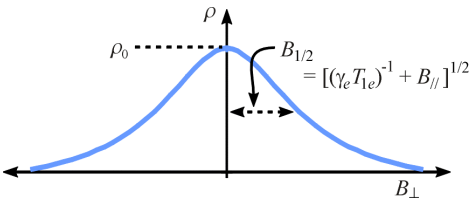

FIG. 1.6 The Hanle curve, describing the Lorentzian dependence of ρ on the magnitude $B_\wedge$ of the transverse magnetic field. The half-width at half-max is determined by the electron gyromagnetic ratio γ_e and spin relaxation time T_{1e}, and the component $B_{//}$ of magnetic field parallel to the electron spin.

$$\rho = \frac{\rho_0 \left(B_{1/2} \right)^2}{\left(B_{1/2} \right)^2 + \left(B_\perp \right)^2}, \tag{1.17}$$

where

$$B_{1/2} = \left(B_H^{\,2} + B_{//}^{\,2} \right)^{1/2} \tag{1.18}$$

is the half-width at half-max of this Lorentzian response to $\mathbf{B}_\wedge$, which is known as the Hanle curve and plotted in Fig. 1.6.

Nuclear spins are also capable of eliciting this Hanle response via their contact-hyperfine-mediated influence on the electron spin. The Hamiltonian that is the sum over all nuclear sites Eq. (1.9) governs this effect, and may be written as

$$\mathcal{H}_{hf}^{C} = \left(-\gamma_e \mathbf{S} \cdot \mathbf{B}_n \right) h^{-1}, \tag{1.19}$$

in units of Hz, where $\mathbf{B}_n$ is the sum of so-called nuclear hyperfine fields

$$\mathbf{B}_n^{\alpha} = \tfrac{2}{3}\mu_0 (g_0/g^*) h\, \gamma_n^{\alpha} \chi_{\alpha} \sum_i \left|\Psi(\mathbf{r}_i)\right|^2 \left\langle \mathbf{I}^{\alpha,i} \right\rangle \tag{1.20}$$

of isotopes present in the material, and where χ_α is the fractional abundance of the isotope α. Writing $\mathcal{H}_{hf}^{C}$ in this way, we see that each nuclear isotope presents an effective magnetic field to photoexcited electrons, and furthermore, this field may be up to *several Tesla* in magnitude.[6,7] If a component of $\mathbf{B}_n$ is oriented transverse to the direction of photoelectron spin polarization, then it provides $\mathbf{B}_\wedge$ and reduces ρ according to Eq. (1.17). Thus an NMR experiment, which involves just such a reorientation of nuclear spins, may be encoded as a Hanle response. Such an approach yields dramatically enhanced sensitivity and, according to the dependence of $\mathbf{B}_n^{\alpha}$ on $\Psi(\mathbf{r}_i)$ in Eq. (1.20), further solidifies the spatial selectivity of the ONMR experiment.

In early optically detected experiments, cw NMR spectroscopy was used to probe the nuclear spin system. At resonance, the reorientation of nuclear spins, and hence the corresponding $\mathbf{B}_n^{\alpha}$, away from $\mathbf{B}_0$ provided $\mathbf{B}_\wedge$, and in turn a decrease in ρ as the NMR signal. However, this is not the optimum approach to optical detection. First, it suffers from the lack of coherent control of the nuclear spin system inherent in cw NMR, and second, this approach encodes the NMR signal at a poor location on the Hanle curve: its center, where the signal response is most nonlinear, and where the minimized slope represents the minimum sensitivity to a transverse field of nuclear origin. Finally, NMR line shapes obtained in this manner are distorted by inhomogeneity of the hyperfine interaction, since continuous optical irradiation is required to provide the PL signal while exciting spin transitions. To overcome these difficulties, a new ONMR scheme is needed: one that allows temporal separation and individual optimization of the processes

of ONP, NMR evolution, and optical detection. Sections B.3 and B.4 review the advances in these areas made in the Weitekamp group at Caltech.

3. Time-Sequenced ONMR Methodology

Buratto, *et al*.[8,39,40] provided two major advances in ONMR with their development of the time-sequenced methodology. The first is due to the arrangement of separate periods for ONP, *arbitrary* time-domain NMR evolution, and optical detection, as shown in Fig. 1.7. An important result of this simple modification of previous experiments is that NMR evolution is free from concurrent optical detection, and thus from the corresponding perturbation of inhomogeneous hyperfine interactions. Additionally, since this segmentation incorporates time-domain NMR evolution, one may use the most sophisticated NMR techniques to probe nuclear spin interactions. These include multiple-pulse experiments, which may incorporate any perturbation to the spin system, including optical excitation, if measurement of the corresponding effects is desirable. The noted segmentation of the ONMR timeline is generally applicable with a variety of optical detection methods, including those that rely on an Overhauser shift of PL lines[11,12] or on Faraday rotation[13] to encode NMR; however, these, and other recent experiments that rely on the Hanle effect, were executed without time sequencing. One goal of the research presented in this thesis is to demonstrate that the most informative NMR experiments must be obtained using an approach based on time sequencing.

The second advance provided by the time-sequenced approach is due to the use of a transverse reference field $\mathbf{B}_{\perp}^{ref}$ for improved Hanle-effect optical detection. At the end of the timeline shown in Fig 1.7, a signal field,

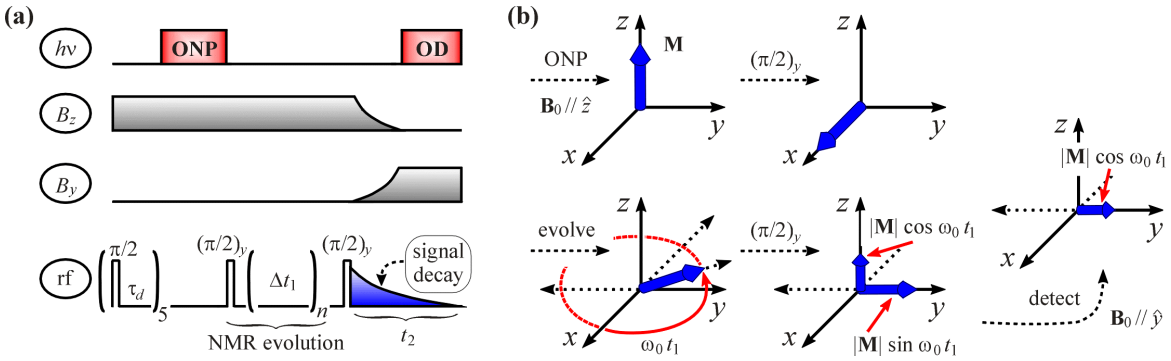

FIG. 1.7 **(a)** Timeline of the time-sequenced ONMR experiment with CP laser ($h\nu$) irradiation along the z-axis, magnetic fields along the lab-frame y- and z-axes, and rf irradiation orthogonal to z shown. **(b)** The corresponding trajectory of nuclear spin magnetization **M**.

In the first step, depicted only in (a), residual spin magnetization is killed with a sequence of 5 $\pi/2$ rf pulses with intervening delays τ_d p T_2, the transverse nuclear spin relaxation time. This ensures an equivalent shot-to-shot starting point for repetition of the experiment. A $(\pi/2)_y$ pulse following ONP initiates the NMR evolution period of time $t_1 = (n \times \Delta t_1)$, where n is an integer. A second $(\pi/2)_y$ pulse stores the x-component, $|\mathbf{M}| \cos \omega_0 t_1$, of remaining spin magnetization along $\mathbf{B}_0 // z$, leaving the y-component in the xy-plane, where it quickly dephases to zero. The stored spin magnetization is the NMR signal and next follows $\mathbf{B}_0$ as it is cycled adiabatically to the y-axis. Optical detection (OD) for time t_2 ensues, where the Hanle effect response to the total field $|\mathbf{B}_y + \mathbf{B}_n^{\alpha}|$ in the transverse plane is observed. [Recall from Eqs. (1.2) and (1.20) that $\mathbf{B}_n^{\alpha} \propto \mathbf{M}$, and thus follows the trajectory shown in (b).] $\mathbf{B}_y$ serves as the reference field $\mathbf{B}_{\perp}^{ref}$ discussed in the text.

A time-domain NMR spectrum is obtained by repeating the experiment several times while incrementing n. A set of dc transients in t_2 results, each of which is integrated to yield a single point in the time-domain interferogram in t_1. Fourier transformation of this so-called "pointwise" spectrum yields the frequency domain.

$$\mathbf{B}_n^{sig}(t_1) = \mathbf{B}_n^{\alpha} \cos \omega_0 t_1 , \tag{1.21}$$

is collinear with an external field, $\mathbf{B}_y = \mathbf{B}_{\perp}^{ref}$. The vector sum of these fields determines the PL polarization response shown in Fig. 1.8. The reference contribution to the total transverse field effectively shifts the Hanle curve such that polarization response to the nuclear component is approximately about the half-width, rather than the peak, of the Lorentzian. This improves both the linearity and the sensitivity of the NMR signal response by encoding it in a region with a larger, flatter slope.

At this point, we note that another innovation is required in order to obviate the need for cycling the external field, which is a desirable modification since incorporating field cycling delays reduces valuable throughput in these cryogenic experiments, and because extra apparatus is required to provide a second external field. Furthermore, the approach of Buratto, *et al*.[8,39,40] requires pointwise detection of the time-domain NMR signal via a set of transient signals at dc. *Real-time* detection of precession of $\mathbf{B}_n^{\alpha}$ as a modulation of ρ would require differentiation of the in-plane orientation of $\mathbf{B}_n^{\alpha}$, while the Hanle effect depolarization of PL discussed in this and the previous section depends only on the *magnitude* of the transverse field. The following section is a review of the most recent advance in ONMR methodology: Larmor beat detection, which encodes real-time NMR evolution in the Hanle depolarization of luminescence and does not require field cycling.

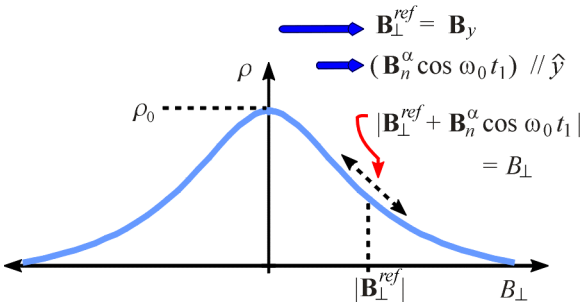

FIG. 1.8 The Hanle response of PL polarization ρ to the total transverse field $(\mathbf{B}_{\perp}^{ref} + \mathbf{B}_n^{\alpha} \cos \omega_0 t_1)$ during optical detection. This encodes the time-domain NMR signal.

4. The Larmor Beat Detection Method

The Larmor beat detection (LBD) method of Marohn, *et al*.[9,41-43] relies on a transverse reference field that is constant in magnitude, as with the approach of Buratto, *et al*., but which, in distinction, leaves the nuclear quantization axis along $\mathbf{B}_0 \; // \; \hat{z}$ such that precession remains in the transverse plane and the hyperfine field $\mathbf{B}_n^{sig}(t)$ of Eq. (1.21) is a function of real time *t*. Thus, in order to elicit a Hanle response, the

reference field must appear to luminescent electrons as an effective field, but not to lattice nuclei. This is exactly the case with a nuclear hyperfine field. Aside from the species providing $\mathbf{B}_n^{sig}(t)$, such a field is available from the other NMR active (i.e., $I \neq 0$) isotopes present in the III-V alloy studied. For example, in GaAs, the principle isotopes present are spin-$\frac{3}{2}$: ^{69}Ga, ^{71}Ga and ^{75}As with $\chi_\alpha = 0.604$, 0.396 and 1, respectively. These nuclei can provide, in any combination, signal $\mathbf{B}_n^{sig}$ and reference $\mathbf{B}_n^{ref}$ hyperfine fields, with the remaining principle isotope and any dilute species contributing $\mathbf{B}_n^{misc}$ to the total hyperfine field.

The timeline used with the LBD method of real-time detection is shown in Fig. 1.9. During both ONP and optical detection, $\mathbf{B}_0$ is conveniently oriented collinear with the propagation axes of optical excitation and detection. A $\pi/2$ pulse on the signal nucleus initiates NMR evolution, which is concurrent with optical detection and off-resonance spin locking (i.e., rf irradiation that is in phase with nuclear precession) of the reference isotope. The off-resonance lock places reference nuclei in an effective magnetic field

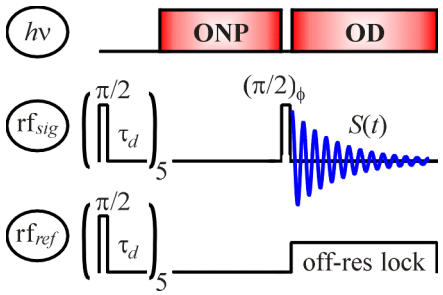

FIG. 1.9 The timeline for *real-time* optical detection of NMR using Larmor-beat detection. Irradiation of signal and reference nuclei is shown on two lower lines, while that of miscellaneous nuclei is omitted here. The timeline opens with a kill sequence on all nuclei, followed by ONP, an arbitrary phase $\pi/2$ prep pulse, and finally real-time optical detection of the NMR signal $S(t)$. Use of an off-resonance spin lock on the reference nucleus is discussed in the text.

$$\mathbf{B}_{eff}^{ref} = -\left((\omega_0^{ref} - \omega_{lock})\,\hat{z} + \omega_1\,\hat{\tilde{x}}^{ref}\right)/\gamma_n^{ref}, \qquad (1.22)$$

where $\hat{\tilde{x}}^{ref}$ is the unit vector along the rotating-frame *x*-axis of the reference isotope with Larmor frequency ω_0^{ref}, and $(-\omega_1 / \gamma^{ref})$ is the magnitude of the rf irradiation at angular frequency ω_{lock}. Concurrent application of this rf irradiation and optical excitation results in a steady-state precessing hyperfine field $\mathbf{B}_n^{ref} // \mathbf{B}_{eff}^{ref}$, which has a component in the transverse plane that is used as the reference field for LBD.

Luminescent electrons provided by continuous optical excitation exhibit a Hanle response to the vector sum

$$\mathbf{B}_n^{tot}(t) \;=\; \left(\mathbf{B}_n^{sig}(t)\, e^{-t/T_2} \;+\; \mathbf{B}_n^{ref}(t) \;+\; \mathbf{B}_n^{misc}\right) \tag{1.23}$$

of hyperfine fields due to freely precessing signal nuclei, locked reference nuclei and static miscellaneous nuclei. First, $\mathbf{B}_n^{misc}$ and the component of $\mathbf{B}_n^{ref}(t)$ along $\hat{z}$ make an important contribution to the width of the Hanle curve as components of the field $\mathbf{B}_{//}$ in Eq. (1.18). Therefore, the longitudinal components of all hyperfine fields must be constant during optical detection and for shot-to-shot repetition of the experiment. Secondly, the precessing transverse components, $\mathbf{B}_n^{sig}(t)$ and $\left(\mathbf{B}_n^{ref}(t)\right)_\perp$, of the total field depolarize luminescence. The time dependence of these fields and of the projection of their vector sum into the plane are plotted in Fig. 1.10(a). The depolarizing field $\left(\mathbf{B}_n^{tot}(t)\right)_\perp$ is time dependent at the Larmor beat frequency

$$\omega_{sr} = \left(\omega_0^{sig} - \omega_0^{ref}\right). \tag{1.24}$$

The Hanle response to a vector field such as $\left(\mathbf{B}_n^{tot}(t)\right)_\perp$ is given by the surface of revolution obtained by turning the 2D Hanle curve about the vertical axis at its peak,

yielding the 3D Hanle surface shown in Fig. 1.10(b). Radiofrequency modulation of luminescence polarization $\rho(t)$ at ω_{sr} results from the combined effects of signal and reference hyperfine fields, as depicted in the figure by the projection of $\left(\mathbf{B}_n^{tot}(t)\right)_\perp$ onto the Hanle surface. Since $\mathbf{B}_n^{ref}(t)$ has constant magnitude, the process of LBD effectively mixes the NMR signal down to the Larmor beat frequency ω_{sr}, where $\rho(t)$ is the carrier. Marohn[42] derived this result by including the time dependence of signal and reference hyperfine fields at their respective Larmor frequencies in Eq. (1.17) and expanding the resulting expression in a Taylor series about $B_n^{sig} = 0$. Review of that derivation is beyond the scope of this thesis.

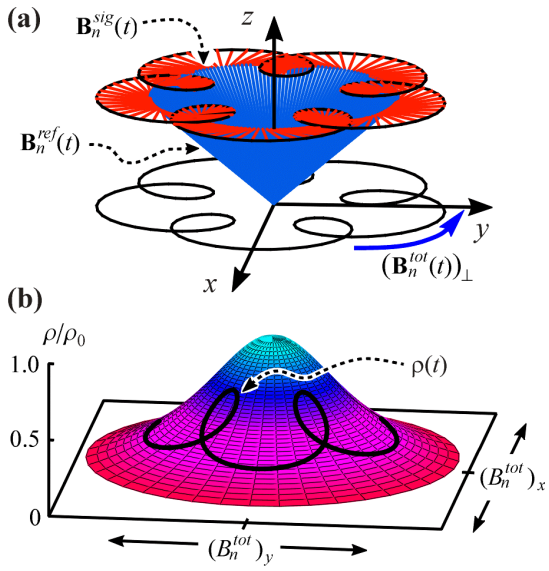

FIG. 1.10 **(a)** The vector sum of two precessing nuclear hyperfine fields, $\mathbf{B}_n^{ref}$ and $\mathbf{B}_n^{sig}$, due to distinct isotopes in the semiconductor lattice. **(b)** The projection of this sum on the 3D Hanle curve.

One aspect of the real-time LBD method, NMR evolution that is simultaneous with optical detection, may seem a backwards step to the state of affairs in ONMR that preceded the advances of time sequencing. However, because LBD involves time-domain NMR evolution, one may apply optical detection in selected windows as a periodic probe of the NMR evolution period, thus diminishing its perturbative effects. Such an approach, referred to as stroboscopic detection, is commonly used in conjunction

with NMR multiple-pulse techniques, and may even be employed such that unwanted perturbations are averaged to zero.

LBD may also be executed to yield a pointwise time-domain NMR spectrum in a way similar to that presented in Section B.3 in the general context of time sequencing (see especially Fig. 1.7). This approach is characterized by the timeline presented in Fig. 1.11 with separate periods for NMR evolution and optical detection. In this case, as with the real-time methodology, the $\mathbf{B}_0$ is along $\hat{z}$ during ONP and optical detection, but is arbitrary during NMR evolution, since the field may be cycled adiabatically at the breaks indicated in the pointwise LBD timeline. This freedom is useful for experiments in which one wishes to probe the angular dependence of nuclear spin interactions. Optical detection with pointwise LBD differs from the real-time approach in that the signal nucleus is subjected to a true (i.e., on-resonance) spin lock, which is simultaneous with the off-resonance lock of the reference isotope. This places the signal species in an effective field,

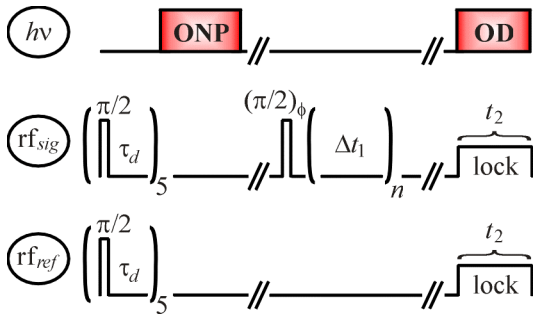

FIG. 1.11 The timeline for acquisition of a pointwise time-domain NMR spectrum in t_1 using Larmor-beat detection in t_2. During ONP and optical detection, $\mathbf{B}_0$ is parallel to the optical propagation axis, but may be cycled to a different orientation or magnitude at the breaks in the timeline, as desired for NMR evolution.

$$\mathbf{B}_{eff}^{sig} = -(\omega_1 / \gamma_n^{sig})\, \hat{\tilde{x}}^{sig}, \tag{1.25}$$

along $\hat{\tilde{x}}^{sig}$, its rotating frame x-axis. The NMR signal is encoded as the Hanle effect depolarization of luminescence by

$$\left(\mathbf{B}_n^{tot}(t)\right)_\perp = \mathbf{B}_n^{sig}(t)\, e^{-t/T_{1\rho}} + \left(\mathbf{B}_n^{ref}(t)\right)_\perp, \tag{1.26}$$

where $T_{1\rho}$ is the time constant for relaxation of signal magnetization along the spin-locking axis, and is on the order of the longitudinal nuclear spin-relaxation time T_1. Because $T_{1\rho}$ is much greater than the relaxation time constant (T_2) for free evolution, spin locking can be thought of as a sample and hold technique, which, in conjunction with LBD, yields a signal transient at ω_{sr}, which may be detected in a narrow bandwidth and mixed to dc. Integration of each member of the set of dc transients resulting from repeated application of the timeline with incremented n yields a pointwise time-domain spectrum in st_1. This pointwise acquisition of a 1D free-induction-decay signal in t_1 via spin-locked transients in t_2 is the optimum approach in terms of signal-to-noise,[1(b)] and is the sole optical detection scheme used in experiments presented in this thesis.

C. High-Resolution Solid-State NMR

In preceding sections of this chapter, much emphasis is placed on advances in ONMR methodology that enable high-resolution time-domain NMR experiments. The main goal in utilizing this capability of ONMR, along with its high sensitivity and spatial selectivity, is to measure the variation of electronic properties in the vicinity of local structures that control device function in epitaxial III-V samples. These include point defects, single heterojunctions, quantum wells, and quantum dots. The ideal experiment establishes a one-to-one relationship between an NMR observable, e.g., line position, and some character of the local electronic environment. Thus, for spatially varying electronic properties that bear upon NMR transition frequencies, spectral resolution translates to

spatial resolution, and sets the size scale at which material properties can be dissected. In the noted epitaxial structures, spatial variation is atomically abrupt, and the corresponding demand for NMR spectral resolution is at the state of the art in the field.

In the present section, multiple-pulse techniques for high-resolution solid-state NMR are discussed. Additionally, a novel method for high-resolution NMR measurement of perturbations to the sample is presented, in which the perturbations are cyclic and applied in synchrony with a multiple-pulse sequence. It is straightforward to implement each of the high-resolution techniques presented here in a time-sequenced ONMR experiment, and, in subsequent chapters, multiple-pulse ONMR experiments for the study of single epitaxial structures in GaAs materials are presented. Resolution in these experiments is *three orders of magnitude* better than in any previous ONMR experiment, and has enabled us to measure local electronic properties via a spectral response that is understood in terms of the site-by-site contributions of lattice nuclei.

1. Multiple-Pulse Line Narrowing

Solid-state NMR spectroscopy has notoriously poor spectral resolution due to the distribution of dipolar, quadrupolar and anisotropic chemical shift contributions to the internal rotating-frame spin Hamiltonian $\tilde{\mathcal{H}}_{int}$. [See, for example, Fig. 1.12(a).] This difficulty is especially apparent in comparison to liquid-state spectroscopy, where molecular motions are fast on the NMR timescale and average to zero the first-order effects of these spin interactions, routinely yielding sub-Hz linewidths. However, solid-state NMR has the advantage, in spite of its resolution problems, of directly measuring

---

[1(b)] See Weitekamp[44] Section III.B.2.*f*.

the influence of such couplings on NMR line positions. The difficult trick is to distill one or more interactions from among the myriad overlapping contributions to an NMR spectrum.

Two approaches have been developed for the purpose of selectively averaging spin interactions in solids. The first incorporates motional averaging, such as magic angle spinning (MAS) of the sample,[45-47] where the effects of orientation-dependent spin interactions are averaged to zero by making them time dependent during NMR evolution. The other approach, pioneered by Hahn's invention of the spin echo,[31] relies on a sequence of resonant rf pulses and intervening free-evolution windows that achieves similar averaging via coherently driven motions of nuclear spin magnetization.[48] For ONMR experiments, in which optical excitation and detection are directed along a fixed sample axis, schemes that utilize motional averaging are untenable; thus, experiments presented in this thesis employ the multiple-pulse approach exclusively.

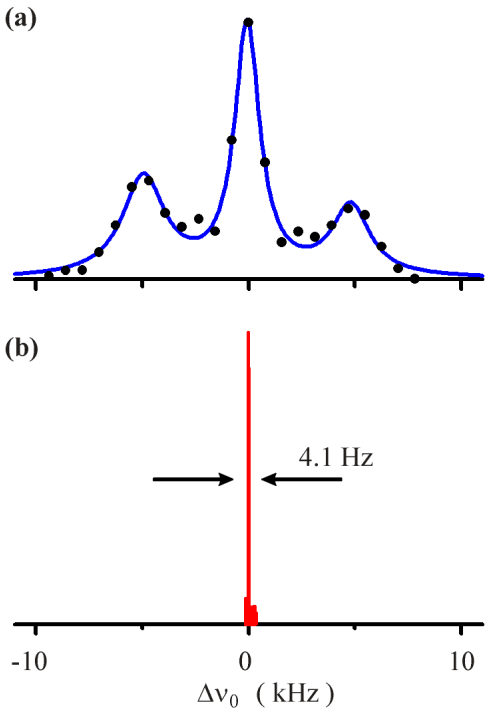

FIG. 1.12 **(a)** ^{71}Ga spin-echo ONMR spectrum from an AlGaAs/GaAs heterojunction sample, obtained with pointwise time-domain evolution and LBD. Linewidths of 1.5-3 kHz reflect a distribution of dipolar couplings and strain-induced quadrupole splittings. **(b)** ONMR spectrum, with indicated Lorentzian FWHM, obtained from the same sample. The enhanced resolution resulted from application of the CLSW-16 multiple-pulse line-narrowing sequence discussed in this section.

The time evolution of a nuclear spin system under the influence of a multiple-pulse sequence is analyzed using coherent averaging theory,[32,33,49] which replaces $\tilde{\mathcal{H}}_{int}$ with an effective Hamiltonian describing the net evolution of nuclear spins over integer multiples of a *cyclic* sequence. For well-designed sequences, the dominant contribution to the effective Hamiltonian is the time-average $\bar{\mathcal{H}}^{(0)}$ of $\tilde{\mathcal{H}}_{int}$ over the duration t_c of the sequence. Contributions to $\bar{\mathcal{H}}^{(0)}$ are transformations of rotating-frame operators into the so-called "toggling-frame" interaction representation. In the i^{th} evolution window of a pulse sequence, such transformation of an arbitrary rotating-frame operator $\tilde{O}$ is given by

$$O_{\mathrm{T},i} = U_{\mathrm{T},i}\,\tilde{O}\,U_{\mathrm{T},i}^{\dagger}, \tag{1.27}$$

where $U_{\mathrm{T},i}$ and its Hermitian conjugate $U_{\mathrm{T},i}^{\dagger}$ are the unitary propagation operators that perform the inverse action of the rf pulses preceding the i^{th} window. Finally, the contribution of $\tilde{O}$ to the average Hamiltonian is

$$\bar{\mathcal{H}}_{O}^{(0)} = t_{\mathrm{c}}^{-1}\sum\nolimits_{i}\tau_{i}\,O_{\mathrm{T},i}, \tag{1.28}$$

where τ_i is the duration of the i^{th} window.

The evolution governed by an average Hamiltonian is straightforward to interpret when one considers the cyclic nature of the multiple-pulse sequence, which requires that

$$U_{\mathrm{T},i}(n\,t_c) = \mathbb{1}, \tag{1.29}$$

where n is an integer number of cycles and $\mathbb{1}$ is the identity matrix with the dimensions of the Hilbert space that describes the spin system. This relation and Eq. (1.27) imply that the rotating and toggling frames are coincident at times $t = n\,t_c$, and thus one can interpret evolution of the spin system up to such times using the usual density matrix formalism

for analysis of evolution in the rotating frame. For example, the time-dependence of the observable corresponding to the operator $\hat{O}$ is given by

$$\langle \hat{O} \rangle(n t_c) = Tr\left[\hat{O}\rho(n t_c)\right], \tag{1.30}$$

where

$$\rho(n t_c) = \exp\left(-i \bar{\mathcal{H}}^{(0)} n t_c\right) \rho(0) \exp\left(+i \bar{\mathcal{H}}^{(0)} n t_c\right) \tag{1.31}$$

is the time-dependent density operator at time $t = n t_c$. Thus, to monitor real-time evolution under a cyclic sequence, one uses the method of stroboscopic detection, where spin magnetization is sampled only at integer multiples of the cycle duration, at which time $\rho(t)$ is given by Eq. (1.31). In addition, stroboscopic detection is naturally combined with pointwise detection of NMR evolution by using t_c as the increment time for the encoding period preceding signal detection.

In the present work, so-called time-suspension multiple-pulse sequences[50,51] are of interest. These yield $\bar{\mathcal{H}}^{(0)} = 0$ free of all dipolar, quadrupolar, chemical shift and heteronuclear indirect couplings. In particular, the CLSW-16 sequence of $\pi/2$ rf pulses,[50] shown in Fig. 1.13(a), is our high-resolution workhorse, regularly reducing the ~ 3.5 kHz dipolar linewidth of nuclei in GaAs to < 10 Hz. Comparison of the ^{71}Ga ONMR spectra in Fig. 1.12 illustrates this enhancement in striking fashion. Both were collected in a pointwise manner at ~ 2 K from identical samples. The spectrum in (a) was obtained using a spin-echo sequence, which refocuses heteronuclear dipolar couplings, but leaves homonuclear dipolar and quadrupolar interactions as the primary factors determining the spectral distribution over more than 10 kHz. The spectrum in (b) was

obtained using the modified form of CLSW-16 shown in Fig. 1.13(b), resulting in its 4.1 Hz FWHM Lorentzian line shape, which is at the state of the art in solid-state NMR.

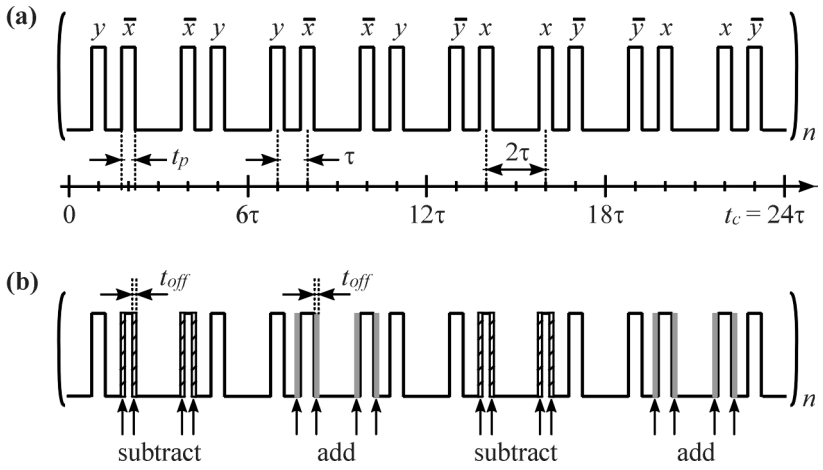

FIG. 1.13 **(a)** The CLSW-16 multiple-pulse line-narrowing sequence of duration t_c. Each solid bar indicates a $\pi/2$ rf pulse of duration t_p and labeled according to its phase in the rotating frame of the signal nucleus. Pulses are centered so that, in the δ-pulse approximation, intervening free-evolution windows alternate in duration τ and 2τ. **(b)** A modification of the sequence, where the duration of selected pulses is symmetrically reduced or increased to ($t_p \pm 2\, t_{off}$), as indicated. This results in a homogeneous contribution, $\bar{\mathcal{H}}_{off}^{(0)} = \omega_{off} I_z$, to the average Hamiltonian, which shifts NMR evolution in t_1 from zero frequency to ω_{off} in the rotating frame, and achieves second averaging to truncate residual error terms.

The purpose of the noted modification of CLSW-16 is twofold. First, the sequence in Fig. 1.13(b) homogeneously shifts the NMR signal from dc in the indirect time dimension of a pointwise-detected experiment. This reduces its susceptibility to shot-to-shot variation (i.e., t_1 noise) of the detector and/or spectrometer responsivity. The second advantage is that this frequency shift truncates residual errors due to contributions to the effective Hamiltonian of higher order than $\bar{\mathcal{H}}^{(0)}$. Such error terms can increase linewidth, and, when of sufficient magnitude, add unwanted structure to the NMR spectrum. This effect is shown in Fig. 1.14, where comparison of spectra collected using each form of CLSW-16 clearly demonstrates the advantage of the modified approach.

The removal of error terms by adding a homogeneous offset term $\bar{\mathcal{H}}^{(0)}_{off}$ to $\bar{\mathcal{H}}^{(0)}$ is known as "second averaging,"[52] and is analogous to the truncation of off-diagonal terms in $\tilde{\mathcal{H}}_{int}$ by the Zeeman interaction.

The modification of CLSW-16 shown in Fig. 1.13(b) is based on a similar variation that was developed for use in solid-state magnetic resonance imaging,[50,54] and is also conceptually equivalent to earlier approaches to second averaging.[52] An explicit calculation of the rf-induced offset provided by the redesigned sequence follows.

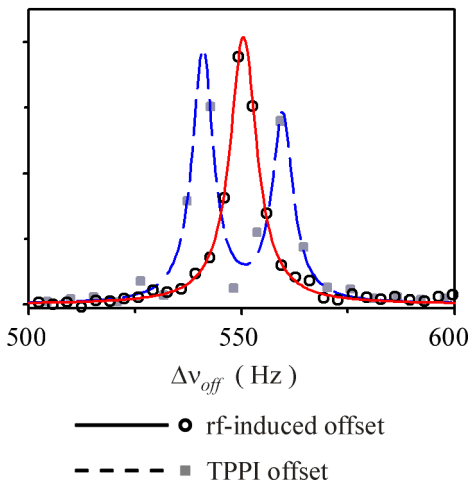

FIG. 1.14 ^{71}Ga NMR spectra (points) collected using CLSW-16 with pointwise time-domain evolution, and corresponding fits (lines). The modified version of CLSW-16 described in the text and Fig. 1.13(b) yielded the single-line (~ 7 Hz FWHM) spectrum, while the unmodified version yielded a 19 Hz doublet splitting due to residual error terms in the effective Hamiltonian. The apparent frequency offset in the doublet spectrum was provided by time-proportional phase incrementation[44,53] (TPPI) of the $\pi/2$ preparation pulse. Unlike the rf-induced offset, the shift provided by TPPI is not due to true spin evolution and does not result in second averaging.

In the modified sequence, the duration, ($t_p \pm 2\, t_{off}$), of x and $\bar{x}$ rf pulses is either increased or decreased relative to the $\pi/2$ pulse duration t_p. Each added or subtracted rf segment j of duration t_{off} is described by the rotating-frame Hamiltonian,

$$\tilde{\mathcal{H}}_{rf,j} = \zeta_j\, \omega_1 I_x , \tag{1.32}$$

describing rf irradiation along the x or $\bar{x}$ axes. The constant ζ_j is equal to +1 for added x or subtracted $\bar{x}$ irradiation, and to -1 for subtracted x or added $\bar{x}$ irradiation. Each toggling-frame contribution,

$$\mathcal{H}_{\mathrm{T}}^{rf,j} = U_{\mathrm{T},i}\,\tilde{\mathcal{H}}_{rf,j}\,U_{\mathrm{T},i}^{\dagger}, \tag{1.33}$$

to $\bar{\mathcal{H}}_{off}^{(0)}$ is scaled by the duty factor (t_{off}/τ_i) for its duration in the evolution window *i* on the side of the pulse it modifies. Thus, using Eq. (1.28), we obtain

$$\bar{\mathcal{H}}_{off}^{(0)} = (t_{off}/t_c)\sum_i\sum_j U_{\mathrm{T},i}\,\tilde{\mathcal{H}}_{rf,j}\,U_{\mathrm{T},i}^{\dagger} \tag{1.34}$$

Appendix I provides the unitary propagators $U_{\mathrm{T},i}$ corresponding to CLSW-16, as well as the toggling-frame transformations of several spin operators relevant to the nuclear spin system in GaAs. Inserting the toggling-frame transformations of I_x that correspond to windows with pulse modifications into Eq. (1.32), and inserting that result into Eqs. (1.33) and (1.34) yields

$$\bar{\mathcal{H}}_{off}^{(0)} = (16\,t_{off}/t_c)\,\omega_1\,I_z \tag{1.35}$$

for the modification of CLSW-16 shown in Fig. 1.13(b). All subsequent multiple-pulse line-narrowing experiments presented in this thesis utilize the modified form of CLSW-16 shown in Fig. 1.13(b), and hence incorporate the rf-induced offset represented by Eq. (1.35).

2. High-Resolution Observables: POWER NMR

The suspended-time condition discussed above, where $\bar{\mathcal{H}}^{(0)} = 0$, or more practically, $\bar{\mathcal{H}}_{off}^{(0)}$, is a starting point for a novel technique that selectively restores the bearing of weak interactions on NMR evolution. The method, which we refer to as POWER (perturbations observed with enhanced resolution) NMR,[24-26] measures the response of a spin Hamiltonian to a change in the state of a sample. This is a common strategy for determining underlying structure and dynamics by NMR, although the

relatively small induced change in the spectrum is frequently obscured by other interactions, such as inhomogeneity of $\mathbf{B}_0$ and the spin couplings discussed in the previous section.

If, however, a perturbation of the sample can be applied cyclically, then it is possible to obtain information on the difference between the perturbed and unperturbed spin Hamiltonians free of the line broadening associated with the invariant terms. POWER NMR accomplishes this by synchronizing the cyclic perturbation with a time-suspension multiple-pulse sequence, in such a way that a perturbative contribution $\bar{\mathcal{H}}_p^{(0)}$ survives the averaging process, yielding

$$\bar{\mathcal{H}}^{(0)} = \bar{\mathcal{H}}_{off}^{(0)} + \bar{\mathcal{H}}_p^{(0)}. \tag{1.36}$$

Either secular (i.e., diagonal) or nonsecular terms induced by the cyclic perturbation can be incorporated into a secular high-resolution effective Hamiltonian. Evolution governed by this Hamiltonian results in a spectrum about the offset frequency with structure dominated by the (possibly varied) response of nuclei to the perturbation. The linewidth of individual contributions to the spectrum is roughly determined by the quality of the line narrowing, which is measured in a complimentary experiment that does not include the perturbation,[1(c)] and results in a spectrum like those shown in Figs. 1.12(b) and 1.14.

[1(c)] In some cases, the perturbation-free spectrum is only an approximate reference for the line width underlying the corresponding POWER NMR spectrum. This is due to the possible introduction of homonuclear *J* couplings along with the intended perturbation interaction. If that perturbation results in an inequivalence of neighboring spins, *J* structure, which derives from a rotationally invariant Hamiltonian that is immune to the action of the multiple-pulse sequence, arises in the spectrum. Since the magnitude of the *J* interaction is likely smaller than that introduced by the intentional perturbation, the corresponding structure may be treated as an additional contribution to the line width that is not apparent in the perturbation-free reference. This issue is considered in more detail in Chapter 5, wherein a procedure to account for its effects in simulation of POWER NMR spectra is presented.

Pulse-sequence designs for POWER NMR are conceptually similar to those used in solid-state NMR imaging,[50,51,54] where the perturbation is a magnetic field gradient. Specific examples and corresponding experimental results appear in Chapters 4 and 5 of this thesis. To highlight the significant capabilities of these experiments, some results are previewed in the following.

The prototypical POWER NMR experiment synchronizes optical excitation with the CLSW-16 sequence.[24,26] Using this scheme, we have characterized the distribution of optically induced Knight shifts about shallow point defects where electrons or excitons localize,[26] as presented in Chapter 4. The resulting spectrum is analyzed in terms of single-nucleus spin physics, summed over thousands of sites, and incorporating (1) ONP, (2) the variation in the probability density of the optical excitation with distance from the point defect, and (3) hyperfine relaxation. This treatment suffices for fitting results at short ONP times, though the experiment also provides a basis for including spin-diffusion effects at longer ONP times. The 2D analysis of such an experiment has uncovered the effects of spin diffusion on line shape and on the hyperfine relaxation. An analogous experiment with optically induced electric fields is also presented in Chapter 4, and shows greater sensitivity to the fate of the optically induced hole via a linear Stark effect of the nuclear quadrupole Hamiltonian, promising a more complete picture of the defect sites. Example Knight shift and electric-field spectra are shown in Fig. 1.15(a) and (b), respectively.

Finally, a novel technique within the general class of POWER NMR enables measurement of a third electronic property: the polarization response of *n*-type carriers to an rf electric field. This work is presented in Chapter 5, where along with a detailed

presentation of the methodology and underlying physics, simulation of the isotopically diluted ^{69}Ga spectrum of an *n*-type GaAs QW indicates the possibility for atomic-layer-resolution of the polarization response. In the proposed experiment, nonsecular terms in the nuclear quadrupole Hamiltonian are converted into an effective secular observable: the first-order splittings shown in Fig. 1.15(c). Both the transformation of a nonsecular perturbation into a high-resolution secular observable and the proposed localized measurement of dielectric response are novel aspects of this work.

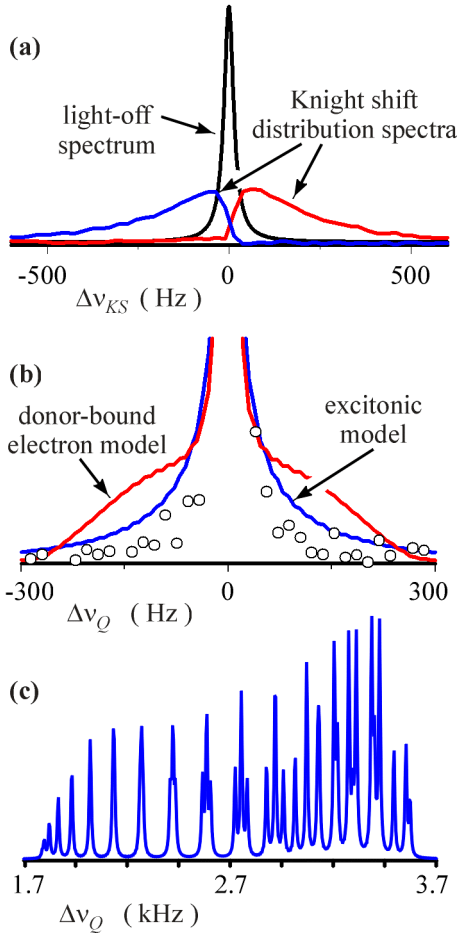

FIG. 1.15 Example POWER NMR spectra and simulations to be discussed in detail in coming chapters. **(a)** ^{71}Ga Knight shift ($\Delta\nu_{KS}$) and **(b)** Stark-induced quadrupole splitting ($\Delta\nu_Q$) spectra obtained by synchronizing cw optical pulses with CLSW-16 during NMR evolution. The direction of the Knight shift relative to the light-off spectrum depends on the electron spin orientation relative to $\mathbf{B}_0$ and placement of optical pulses. In (b) the observed distribution of splittings is compared with adjustable-parameter-*free* simulations corresponding to the indicated competing models for the electronic state. **(c)** Simulated ^{69}Ga NMR spectrum of a 10 nm quantum well, exhibiting atomic-layer-resolved quadrupole satellites due to the Stark response of quantum-confined electrons to an rf electrical perturbation synchronized with CLSW-16.

II. Instrumentation and Procedures for Optical NMR

In this chapter, I detail the apparatus required for ONMR experiments with Larmor beat detection (LBD), and discuss experimental procedures developed for their most effective execution. The instrumentation includes that needed for any modern NMR experiment, such as static and rf magnetic field sources and a spectrometer for amplification and detection of an rf signal in a narrow bandwidth. In addition to these components, our ONMR experiments require a cryogenic system to provide a sample temperature of ~ 2 K, i.e., below the λ-point of *l*-He, and optical apparatus for both excitation at the GaAs bandgap and detection of the rf-modulation of photoluminescence polarization. Furthermore, POWER NMR experiments, which provide the highest resolution for probing sample electronic properties, require synchronizing, to several nanoseconds, the timelines for TTL (transistor-transistor logic) controlled optical excitation and digitally synthesized rf irradiation of the sample. Automated control of the magnetic field orientation and strength, and of laser power and/or polarization is also important, but requires less precise timing.

Much of the instrumentation presented in this chapter was designed, and often home-built, before my arrival in the Weitekamp group at Caltech. For this I owe special credit and gratitude to David Shykind, Steve Buratto, Jack Hwang, John Marohn, Paul Carson and Michael Miller. I must note, however, that any errors in the presentation here are my own. Prior descriptions of the ONMR apparatus are also informative;[39,41-43] however, additions and modifications since the most recent of those writings, and the intended stand-alone quality of this thesis, require a new presentation.

A. The Cryogenic System, Sample Probe and Field Source

As noted in the first chapter, optical nuclear polarization (ONP) requires cryogenic sample temperatures in order to ensure that the dominant factor in nuclear spin relaxation is the fluctuation of contact hyperfine interactions between lattice nuclei and photoexcited electrons. The reduced number of thermal phonons also emphasizes the role of radiative recombination in the relaxation of photoexcited electronic states, thus enabling optical detection of NMR. A *l*-He immersion cryostat is an appropriate vessel for ONMR experiments. Relative to a vapor-cooled system, immersion may provide greater tolerance to high rf power input to excitation coils, as required for multiple-pulse line-narrowing experiments, and reduce rf heating of the sample. However, boiling of the cryogenic fluid can lead to optical scattering that particularly hampers the efficiency of luminescence detection. This problem is avoided by operation below the λ-point of *l*-He, which is reached by reducing the vapor pressure over the immersion bath.[55] The high thermal conductivity of the supercritical helium prevents the spontaneous bubbling present in the 4.2 K liquid. This effect, rather than any advantage provided by further reduction of the sample temperature, motivates operation below the λ-point.

1. Cryogenic Systems

The cryostat shown in Fig. 2.1 was used for experiments presented in this thesis. Internal glass walls separate vacuum and *l*-N_2 insulation jackets from the 10 L capacity main chamber, where the sample is immersed in a *l*-He bath. An oil diffusion pump (Consolidated Electrodynamics, model MCF-60, 2" diameter) with mechanical backing brings the vacuum jacket to a nominal pressure of 10^{-5} torr via stopcock access (not

shown). The 3.0" diameter opening in a copper flange at top accommodates the sample probe and magnet assembly (see Fig. 2.2), while a 2.0" diameter sidearm port provides access for a mechanical pump (Duo Seal, model 1397) via an adjoined 30' length of 1.5" diameter copper pipe. This pump reduces vapor pressure over the *l*-He bath, where a pump rate of ~ 180 L/min succeeds in adiabatically cooling to the λ-point in 40 min with ~ 40 % loss. The *l*-He hold time at the λ-point ranges from 5 to 7.5 hours, depending largely on the rf power demands and corresponding heat input of the particular experiment.

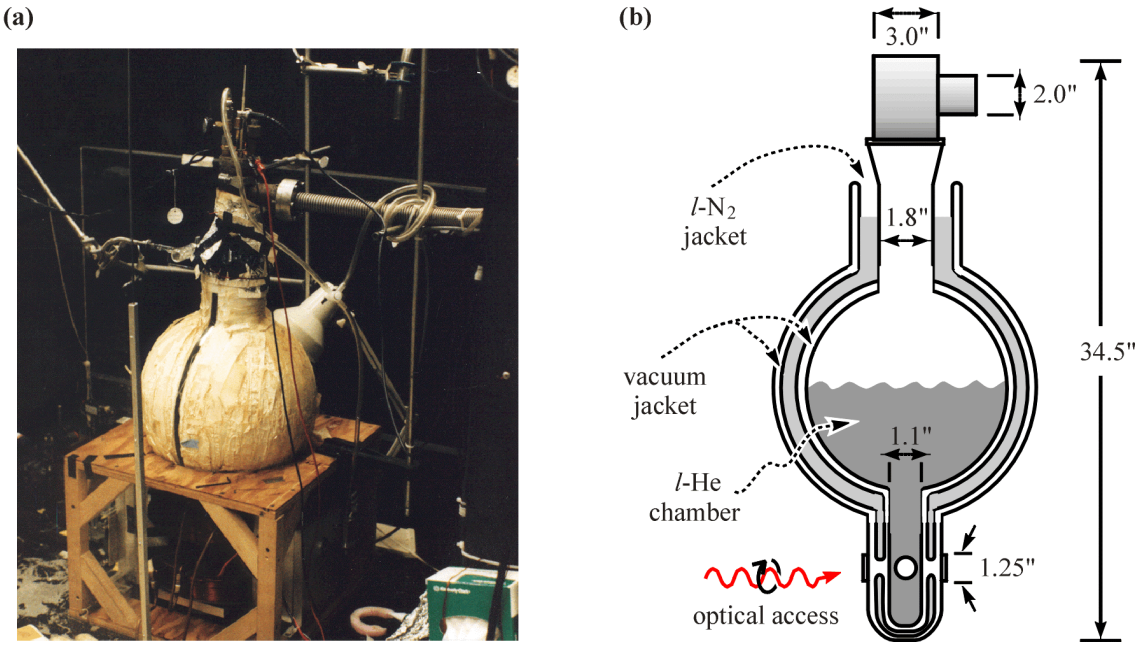

FIG. 2.1 **(a)** The *l*-He optical cryostat used for ONMR and custom made by Pope Scientific from 0.23 cm thick borosilicate glass. **(b)** A cross-sectional schematic of the cryostat.

Optical access to the sample is via 1.25" diameter external quartz windows, followed by 1.5" of vacuum space, a second quartz window of 0.75" diameter and, finally, ~ 0.5" of *l*-He to the sample. The external windows are attached to the cryostat

using wax-like Dekhotinsky cement (Pope Scientific), while occasional resealing is performed with uniform gentle heating of the seal under slight hand pressure. Three directions of optical access are available, though, in practice, we optically excite and detect through the same window.

2. Sample Probe, Magnet Assembly and rf Excitation Source

Fig. 2.2 is a schematic drawing of the probe that accompanies the cryostat. It consists of a 7.2 cm diameter, 3.4 cm thick brass cap, which mates with the vertical copper flange on the cryostat via an O-ring sealed compression fitting. An O-ring sealed fitting followed by an aluminum pipe accommodates a vacuum-insulated *l*-He transfer line for delivery to the main chamber during filling. Temperature is monitored with a carbon glass resistor (Lakeshore Cryogenics). Excluding additional fittings on the head for electrical access, the remainder of the probe is constructed from G-10, including circular baffles which block heat

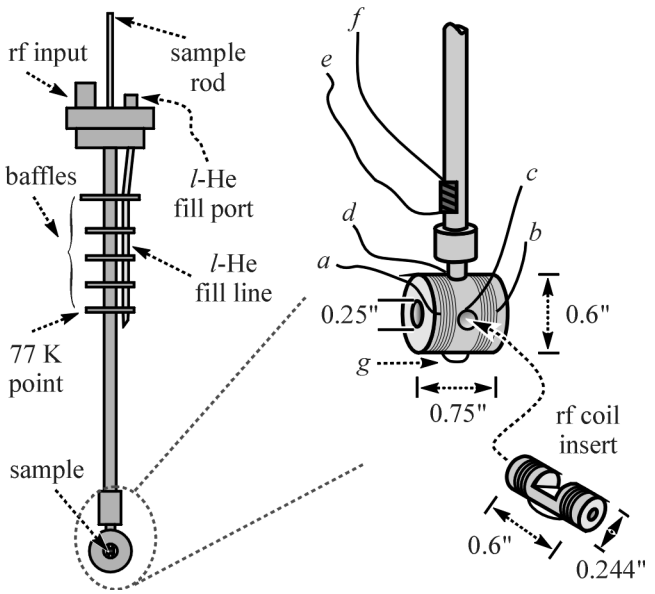

FIG. 2.2 The cryogenic probe for ONMR experiments. The inset depicts the magnet assembly, including an rf coil insert. Electrical leads to each coil contributing to the longitudinal-field are at *a* and *b*, while the pair is joined at *g*. An rf coil insert, with leads *c* and *d*, fits snugly inside the magnet assembly as indicated, and is shown with more detail in Fig. 2.3. Temperature is monitored with a carbon glass resistor (Lakeshore Cryogenics) contacted at *e* and *f*. Pressure release (5 psi) at the probe head is not shown.

transfer between the 77 K cryostat neck and the *l*-He belly. G-10 parts are cemented together using a thermal-expansion-matched epoxy that consists of equal parts resin (CIBA 6010), hardener (CIBA 825) and fine quartz chop. Curing in air for 8 hours was sufficient.

Superconducting magnets are a convenient, low-power-consumption source of magnetic field for cryogenic experiments. Additionally, the requirements for field homogeneity in an ONMR experiment are low relative to traditional NMR, since the sample volume is determined by the absorption depth and spot size, typically ~350 μm in our experiments, of incident laser irradiation. Our probe incorporates a home-wound superconducting Helmholtz pair as the source of the so-called longitudinal field $\mathbf{B}_0$, which is roughly parallel to the propagation axes of optical pumping and detection. The magnet is wound with 54-filament Niobium-Titanium alloy wire on a G-10 form, and has an inductance of 1.67 mH at 2 K, and field strength of about 20.5 mT/A. Typical operation is at ~ 250 mT, as calibrated by NMR. An rf coil is wound on G-10 plug that is inserted into a side access in the magnet assembly. The coil is a joined pair, in which each side consists of 36 AWG insulated wire closed packed in 3 levels of 3 windings each. A notch cut into the plug accommodates a sample fixed to a G-10 rod running down the center of the probe. A detailed picture of the plug/coil design, with corresponding electrical characteristics, is shown in Fig. 2.3(a).

An important aspect of the rf excitation circuit is that the coil is used stand-alone (i.e., untuned and unmatched) with an 500 watt 0.3-35 MHz rf power amplifier (ENI, model 500A). At the low static field values that we use, the resulting frequency response [see Fig. 2.3(b)] enables multinuclear excitation of all isotopes present in GaAs, and can

easily be made to cover the range of nuclei in other III-V's. Operation at an unnecessarily higher field requires a complicated multiply tuned excitation circuit for optically detected NMR with the inherently multinuclear LBD, while the most informative multiple-pulse experiments have the same requirement regardless of detection method.

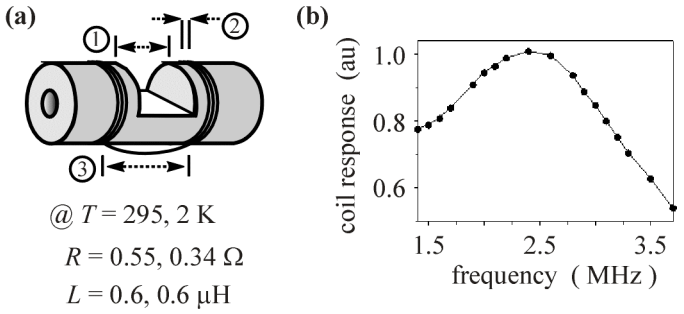

FIG. 2.3 **(a)** Schematic of the rf coil insert. The notch (1) for sample-rod access is 0.125" wide, while the inner edges (2) of the 0.020" deep by 0.021" wide grooves for the pair of coil windings are separated (3) by 0.175". A 0.185" diameter hole is drilled on the long axis providing a view of the sample. Room temperature and 2 K electrical characteristics are noted. **(b)** Coil response to direct input from an rf amplifier. A Rabi frequency of ~ 90 kHz at 3.2 MHz resonance frequency has been obtained for ^{71}Ga with this coil.

3. Strain-Free Sample Mounting

Frank Grunthaner of the NASA Jet Propulsion Laboratory provided MBE-grown GaAs-based samples in 2" diameter disks. Pieces approximately 3 mm × 3 mm are taken from this source by first scoring the GaAs substrate with a diamond-tipped pen, and then gently pressing on the substrate side with a straight edge under the score mark. Record is kept of the in-plane crystal axes, since certain NMR observables, most notably the quadrupole interaction, depend on their orientation with respect to the static magnetic field. The new sample piece is fixed to the G-10 rod at its flattened end with a thin layer of silicone high-vacuum grease (Dow Corning). After inserting the rod into the sample probe, and that assembly into the cryostat at room temperature, the main chamber is pumped and purged in a few cycles and left filled with *g*-He. The *l*-N_2 jacket is then

cooled for 20 minutes with the boiloff of an *l*-N_2 tank passing through a tygon tube, and subsequently filled with *l*-N_2 over another 20 minutes. Cooling of the main cryostat chamber occurs primarily at the neck of the cryostat, and the sample and silicone mounting grease annealed, reaching 77 K in no less than 2 hours. Reduction of the temperature to 4.2 K during the *l*-He fill occurs over ~ 40 minutes, while another 30 minutes achieves the λ-point.

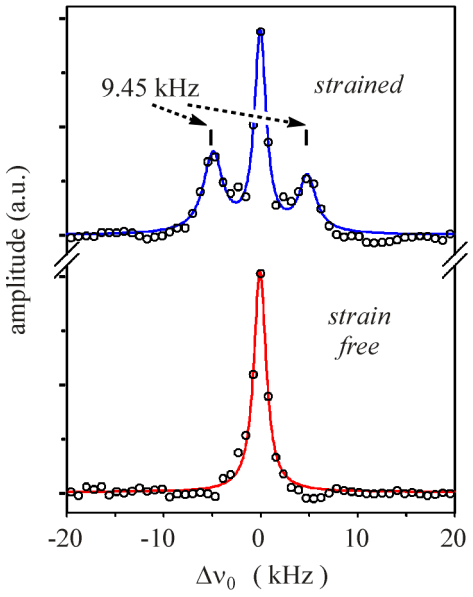

FIG. 2.4 Comparison of ^{71}Ga ONMR spectra of an AlGaAs/GaAs heterojunction sample with and without strain due to the annealing rate of the sample and mounting grease. Collected at 2 K using LBD and time-domain evolution in a static magnetic field along the [001] crystal axis.

The strain-free nature of this mounting/annealing procedure is evidenced by NMR experiments performed on samples with and without strain, which induces quadrupole splitting in GaAs and other III-V's by reducing the cubic symmetry of the lattice.[9] Figure 2.4 provides a comparison of ONMR spectra obtained from samples at 2 K with and without strain. The strained condition was obtained by lowering an identically mounted sample at room temperature into the in-place probe at 4.2 K over a 20-minute period.

B. Execution of the Experiment Timeline

Primary control of time-sequenced ONMR experiments with LBD rests with a DOS-based personal computer (PC) with a 486-generation processor. A C-language

program run on the PC defines three parallel instruction sets that determine the sequence of events during an experiment. As shown schematically in Fig. 2.5, one of these timelines is passed to an external digital word generator (Interface Technologies, model RS-670) via a general-purpose interface bus (National Instruments, model AT-GPIB) that is plugged in to an ISA expansion slot on the PC. The digital word generator provides up to 16 channels of TTL looped instructions with timing resolution of 25 ns. A second set of instructions is loaded to a two-channel, 12-bit arbitrary waveform generator (Signatec, model AWG502) ISA plug-in board. The AWG502 sets the timing for output of digitally synthesized rf waveforms to both the excitation coil and the spectrometer (see Section D). After instruction sets are loaded to the TTL word generator and the AWG502, each runs independent of the PC; however, a third coincident set of timing instructions is executed by the computer program itself, via GPIB communication to other peripheral instruments.

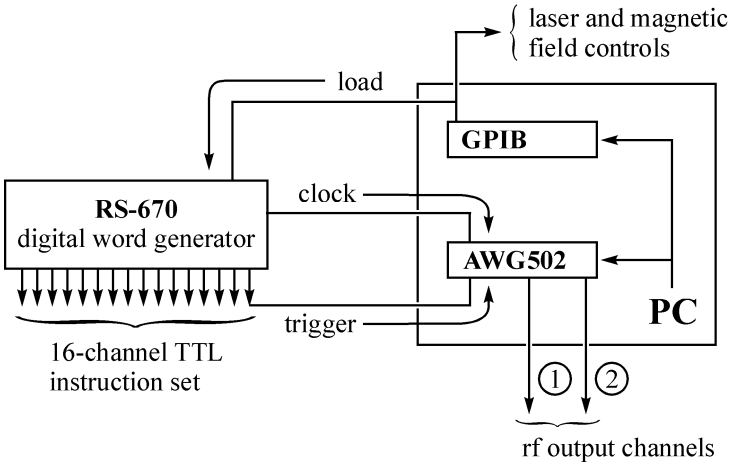

FIG. 2.5 Schematic of the automated control elements in the Larmor-beat-detected ONMR experiment. Four instruments determine event timing: a DOS-based personal computer (PC) with general-purpose interface bus (GPIB) and arbitrary rf waveform generator (AWG502) plug-in boards, and an external digital word generator (RS-670).

Execution of GPIB-controlled events, which are listed in Table 2.1, depends on a software poll to PC's system timer. This is achieved with an *ftime*() function call in

C/C++ that is updated at a rate of 18.2 Hz, resulting in a worst-case jitter of 60 ms in the timing of these events. Thus, when a GPIB-controlled event is to be roughly synchronized with the TTL and rf timelines, the latter two are set to include sufficient delay periods, during which the GPIB event may occur at any time without sensitivity to the noted jitter.

Table 2.1 Devices and corresponding functionality controlled via the general purpose interface bus (GPIB).

Device	GPIB-controlled functions
digital word generator	TTL program loading and sequence initiation
diode laser driver	various, including on/off and high/low TTL-switched power levels
lock-in amplifier	voltage output[(a)]

[(a)] Two-channel lock-in output controls the direction and magnitude of the static magnetic field, as discussed in Section C of this chapter. Traditional lock-in function is not utilized for ONMR.

The timing of TTL-controlled events, such as the on/off state of optical excitation, and of rf events, such as a sequence of $\pi/2$ pulses, must, however, be synchronized to within several nanoseconds for certain POWER NMR experiments presented in this thesis. For this reason, the AWG502 is configured to accept an external TTL trigger and then run on the 40 MHz clock of the TTL word generator. Empirically, the AWG502 timeline begins 700 ns after the rising edge of the TTL trigger; thus it is convenient that the trigger pulse be of the same duration, and followed by a period in which the two timelines are synchronized. Success in this endeavor is demonstrated in Fig. 2.6, which contains plots of the digitized (Tektronix, model DSA602A) channel 1 output of the AWG502 and of a photodiode monitor of TTL-controlled laser output (see Section C.1).

Optical excitation (7.6 μs pulses of cw irradiation) is arranged in windows of the CLSW-16 multiple-pulse line-narrowing sequence[50] of ~ 3.45 μs π/2 rf pulses. The optical pulses provide a Knight shift of the nuclear spins, and their placement during the pulse sequence determines the average Hamiltonian that governs nuclear spin evolution.[26]

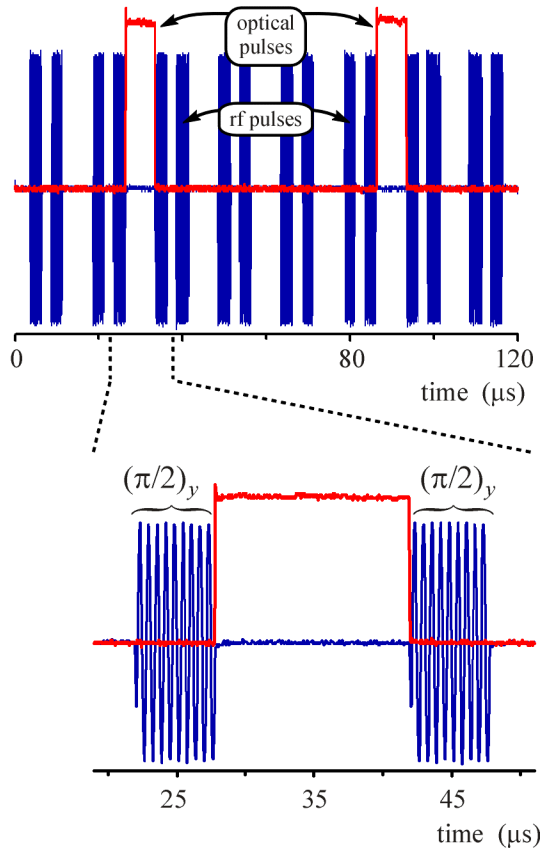

FIG. 2.6 Digitization of events on the timelines controlled by the AWG502 and the TTL word generator. In the plot at top, TTL-switched optical excitation of the sample in selected windows of the CLSW-16 multiple-pulse sequence demonstrates the synchronization of events. The digitized segment shown was preceded by 2.0 s of parallel AWG502 and RS-670 (TTL) operation, thus ensuring sensitivity to any accrued timing offset. The expanded view highlights the accuracy of synchronization, presenting the arrival of an optical pulse between two $(\pi/2)_y$ rf pulses.

C. Optical Systems

1. The Excitation Arm

The arrangement of the optical excitation pathway is depicted in Fig. 2.7(a). The collimated, linearly polarized output (32 mW maximum) of an 802.1 nm diode laser

(Melles Griot, model 06DLL707) passes through a focusing lens (focal length, $f = 40$ cm), followed by a λ/4 plate, which converts the light to right circular polarization (CP). After passage through the optical access windows of the cryostat, the excitation beam, which propagates ~ 15° off-axis of $\mathbf{B}_0$ and the surface normal, reaches the sample at a distance of ~ 45 cm from the focusing lens, yielding a measured spot diameter of ~350 ± 50 μm.

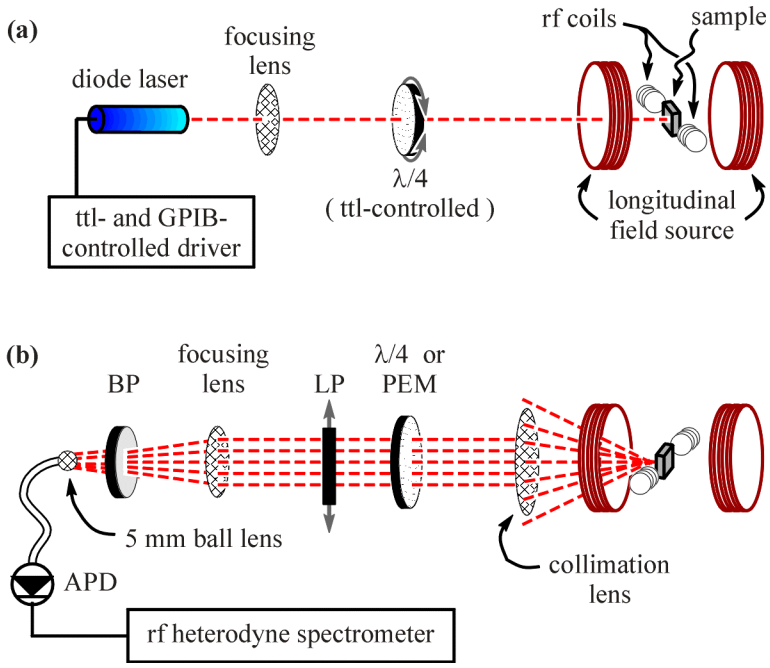

FIG. 2.7 Pathways of optical excitation **(a)**, and detection **(b)**. In the detection arm, BP indicates an optical bandpass filter, LP a linear polarizer and APD a fiber coupled avalanche photodiode. The second element used for polarization analysis used is either a photoelastic modulator (PEM), for use during the tune-up procedure, or a λ/4 plate for Larmor beat detection of NMR.

Automated control of the excitation beam is required for several experiments in which the nature of the excitation differs between the NMR evolution period and the ONP and/or detection periods. A diode laser driver (Melles Griot, model 06DLD103) enables TTL control of laser high and low power levels, including on/off, with the 25 ns RS-670-controlled response time discussed above in Section B. Additionally, a TTL-

controlled stepper motor (Superior Electronics, model MO 61-FD-6244) and driver (Forthright Electronics, model STPNA2) enable automated control of the λ/4 plate. For example, rotation by 90° can be used to switch between left and right CP excitation, and requires 50 steps and 300 ms for execution. The laser power and other miscellaneous controls are accessible via the GPIB interface to the driver.

2. The Detection Arm

Photoluminescence (PL) of the sample is detected along the axis that is mutually parallel with $\mathbf{B}_0$ and the surface normal of the sample. Two arrangements of the detection optics are used: one for pre-NMR tuning of the optics for collection of the PL signal, and a modification of that setup for use during LBD.

i. The Tune-up Configuration

The apparatus for tune-up of optical detection is shown in Fig. 2.7(b). Luminescence passes back out of the cryostat through the two consecutive optical windows and then to a lens (f = 10 cm), which nominally collimates sample PL and is held ~ 5 cm from the outer window.[2(a)] The PL light then passes in sequence through a photoelastic modulator (PEM, Hinds International, model 0101), driven at 50 kHz between the 830 nm ±λ/4 condition, and a linear polarizer. A focusing lens (f = 10 cm) held ~ 52 cm from the collimation lens is followed by an 832 ± 5 nm bandpass filter, and a 5 mm spherical ball lens, which is mounted ~ 8.5 cm from the focusing lens. The ball lens provides coupling of the polarization-analyzed light into the PC-polished free end of a fiber-coupled (200 μm core, 0.24 NA, multimode) avalanche photodiode (EG&G

Optoelectronics, model C30657-010QC-06), which is built into the circuit depicted in Fig. 2.8. The optical bandpass filter limits detection to the emission of a particular feature in the PL spectrum of an $Al_{0.36}Ga_{0.64}As/GaAs$ single heterojunction sample; thus, the ONMR spectrum selectively reports on sites in the vicinity of corresponding electronic states, while the filter also reduces the contribution to photon shot noise from other luminescent features.

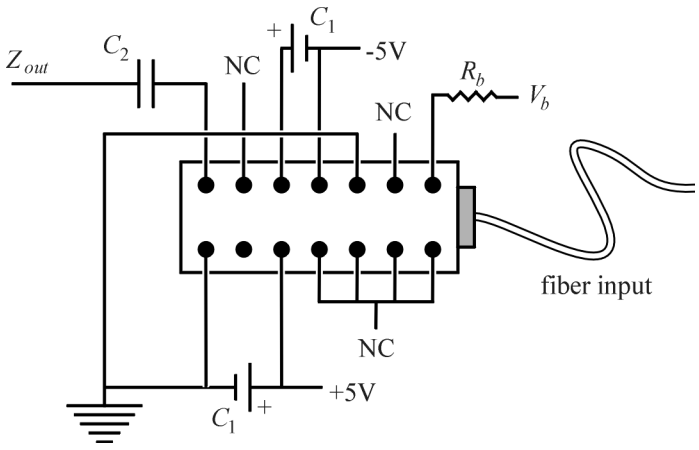

FIG. 2.8 Schematic of the avalanche photodiode (APD) and peripheral circuitry. The prepackaged unit includes the APD hardwired to a transimpedance preamplifier, while peripheral connections include capacitors $C_1 = 10$ μF (polarized) and $C_2 = 0.1$ μF, a resistor, $R_b = 10$ kΩ, to bias voltage $V_b = -217$ V, and unused pinouts (NC). The output impedance is $Z_{out} = 500$ Ω. Quoted specifications for the APD include a responsivity of 21.4 MV/W, bandwidth of 8.4 MHz, and dark noise equivalent power of 0.011 pW / $Hz^{1/2}$.

Polarization analysis is provided in the above scheme as follows. During the first half cycle of PEM modulation, right and left CP light are transformed into orthogonal linearly polarized waves, e.g., *x* and *y*, respectively. The subsequent linear polarizer passes one of these two components. In the second half cycle of the PEM, the conversion of right and left CP light is reversed to *y* and *x*. Thus, the PEM/linear polarizer combination alternately transmits right and left CP components of PL at the 50 kHz oscillation of the PEM.

[2(a)] In order to allow clear passage of the excitation beam, an approximately 3×3 mm notch is cut into the outer edge of this lens.

Properly phased lock-in detection (Stanford Research Systems, model SR510) of the component of avalanche photodiode output at the PEM frequency yields the difference between right and left handed PL signals. Simultaneous chopping of the laser excitation at ~ 1.5 kHz provides the "total" PL signal for lock-in detection at the same frequency. During initial tuning of the optics to locate the signal, for example, by adjustment of relative lens positions, the total PL is monitored, although fine tuning proceeds by maximization of the difference signal. We rely on the Hanle effect,[37] described in Section B.2 of Chapter 1, to validate that the observed signal arises from sample PL. Application of a sufficiently large (~ 50 mT) transverse magnetic field, supplied by electromagnets described in Section E, reduces PL polarization, and hence the difference signal, to zero. Finally, the optimal orientation of the longitudinal field is antiparallel to the orientation of optically pumped electron spins. This yields a difference signal that is larger than in the parallel case (the so-called banana effect),[41,56-58] and, thus, we choose the direction of current through longitudinal magnets on this basis.

ii. The Configuration for Larmor Beat Detection

The NMR signal is observed as an rf modulation of one CP component of PL at the avalanche photodiode. The resulting rf component of the electrical signal is transmitted to a heterodyne spectrometer, as described in Section D. The arrangement of detection optics differs from that used during tune-up in two ways: (1) the PEM is removed from the path and replaced with a time-independent $\lambda/4$ plate with fast and slow axes oriented relative to the linear polarization axis of the following element so as to transmit left CP light only, and, (2) the chopper is removed from the excitation pathway. Observation of Larmor beats in the difference signal may be executed with a detection

path that includes the PEM. However, such an arrangement provides no special advantage over single-component observation, while adding complexity to the signal analysis, as described elsewhere.[42]

iii. Collection of the PL Spectrum

Measurement of the sample PL spectrum and its polarization characteristics compliments study of the luminescent electronic states by ONMR. Spectral analysis of the PL is accomplished by replacing the avalanche photodiode with a fiber-coupled (200 μm core, multimode) optical spectrometer (Ocean Optics, model PC2000) at the fiber optic connection in the assembly shown in Fig. 2.7(b). The total PL spectrum, or its right or left CP components, are collected by excluding or including λ/4 plate in the detection pathway.

D. The rf Heterodyne Spectrometer

Detection of the LBD signal in a 20 Hz bandwidth is accomplished using the scheme shown in Fig. 2.9. The chip carrying the avalanche photodiode (APD) has an internal transimpedance amplifier, which converts the photocurrent to a voltage with primary components at the beat frequency ν_{LBD} and at dc, due to incomplete modulation of PL by the nuclear signal magnetization. As shown in the first segment of Fig. 2.9, the APD output passes through a combination 10:1 impedance transformer and 80 kHz high pass filter (TTE, custom order, serial H579-80K-6220) to match the 50 Ω impedance of the spectrometer and remove the dc contribution to the signal. A 1.5 MHz low pass filter (home built) is used to prevent high-frequency spurious output of the APD from saturating the preamp.

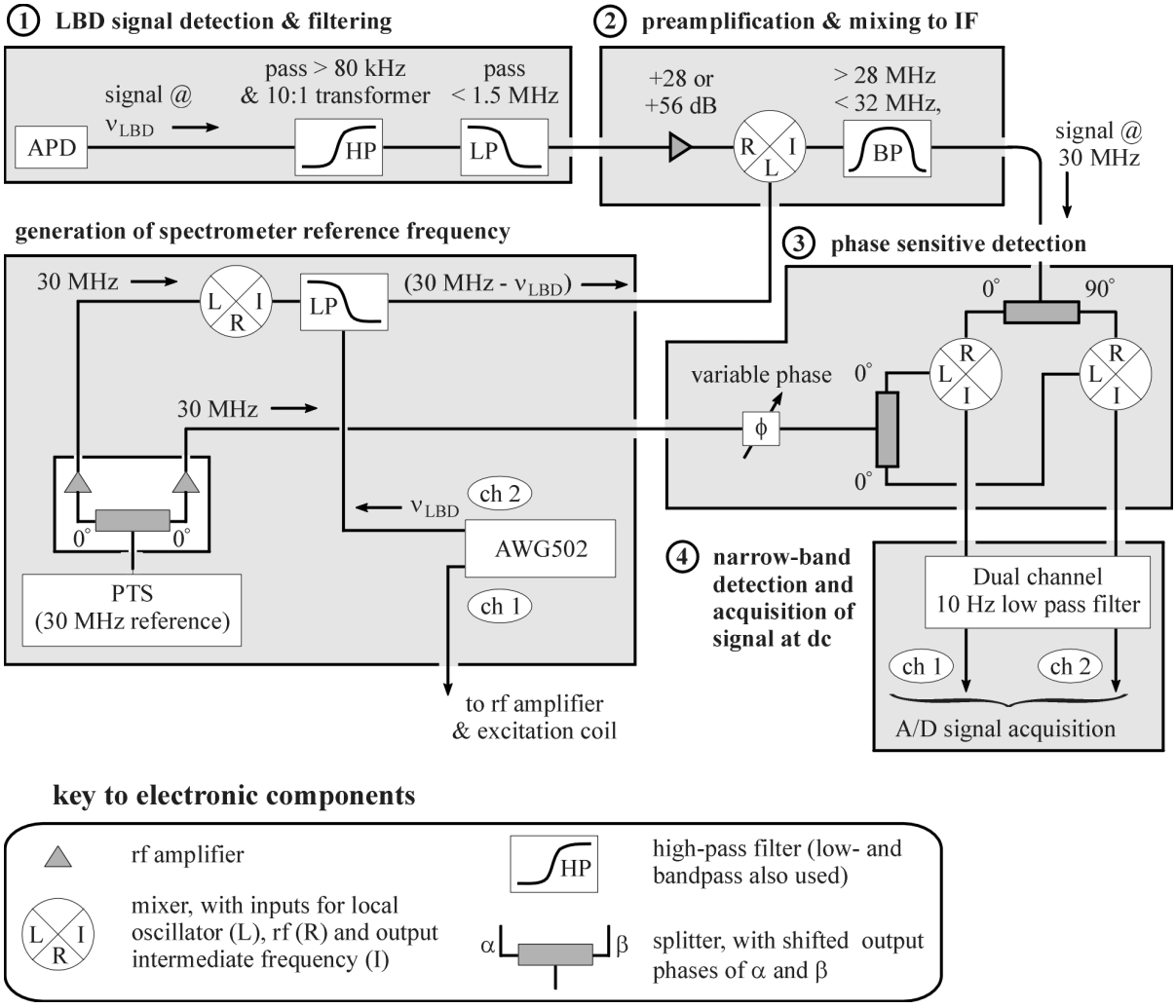

FIG. 2.9 Schematic of the ONMR spectrometer. Some amplification steps have been omitted for the sake of clarity. The net gain is 73 dB or 45 dB depending on whether the preamp is set at high or low.

Two low-noise rf amplifiers (Mini-Circuits, ZFL-500LN) are used in series for initial conditioning of the signal in the second segment of Fig. 2.9; however, a low gain setting is available, in which the second amplifier is bypassed to avoid its saturation in the case where the filtered APD output is sufficiently large. The signal is then mixed (Mini-Circuits, model ZAD-1H) with a reference at

$$\nu_{ref} = (30\ \text{MHz} - \nu_{LBD}), \tag{2.1}$$

and filtered to yield an intermediate signal carrier at 30 MHz. This reference is a filtered sideband from the mixture of the second-channel AWG output and the conditioned 30 MHz output of a precision source (Programmed Test Sources, model PTS500). The appearance of ν_{LBD} in Eq. (2.1) is exact, since both the signal frequency (i.e., the APD output), which is fixed by rf spin locking[44,59] of the LBD signal and reference nuclei, and this reference output are determined by rf generated from the same coherent source: the AWG.

Phase sensitive detection occurs in the third segment shown in Fig. 2.9, in which the 30 MHz signal carrier is split into two components 90° out of phase. Each of these is mixed with the 30 MHz conditioned PTS output. Since this places the signal at dc, adjustment of the phase of the latter is used to zero the signal in one channel while maximize it in the other, thus ensuring observation of the entire signal. Finally, both channels are fed through a 10 Hz low pass filter (Stanford Research Systems, model SR640) and acquired at the 20 Hz digitization rate of a 16-bit A/D converter (Computer Boards, model CIO-DAS 1402), which is triggered by a 1 μs TTL pulse from the RS-670. A C-language program has been written to provide graphical output of the sequence of digitized signal transients collected during an ONMR experiment.

E. Magnetic-Field Cycling

During the periods of ONP and Larmor beat optical detection of NMR, the static magnetic field must be parallel, or nearly so, with the propagation axes for optical pumping and detection. However, the time-sequenced approach[8,9] to ONMR allows for a different field orientation during the NMR evolution period, enabling study of the

angular dependence of nuclear spin interactions. Of particular relevance to this thesis are electric-field-induced quadrupole interactions, which arise due to a reduction in the symmetry of the crystal lattice brought on by the perturbation of a dc[60-62] or rf[25,63,64] electric field. The dc-field-induced effect, as exploited in this thesis to characterize the radial field distribution of single photocarriers, vanishes when the static magnetic field is along the [001] growth axis of GaAs, as is the case for ONP and LBD. Thus, its investigation requires adiabatic cycling of the magnetic field after ONP, yielding a new orientation for NMR evolution, which is followed by a second cycling event to restore the original orientation for optical detection.

For this purpose, our apparatus includes an electromagnet that is external to the cryostat and provides a transverse magnetic field that is orthogonal to both the rf excitation coils and the longitudinal field discussed above in Section A.2. The transverse magnet is an approximate Helmholtz pair, where each coil consists of 31×31 windings of square (1.7 mm on a side) copper wire supported on a copper yoke with 31 cm and 19 cm outer and inner diameters, respectively, and a width of 5.7 cm. The two yokes are held at a separation of 12 cm in an aluminum stand, which additionally enables rotation of the entire assembly by ±12° for further investigation of the angular dependence of spin interactions. The room-temperature electrical characteristics of this water-cooled pair are $R = 11.0\ \Omega$, $L = 99.1$ mH, and $C = 197$ nF, while the field is 5.65 mT/A at the sample. Typical operation is at 57.8 mT, for a ^{71}Ga resonance frequency of 750 kHz.

Cycling the field between the longitudinal and transverse sources is accomplished via GPIB control of the two-channel analog voltage output of a lock-in amplifier (Stanford Research Systems, model SR510). The first channel serves as the modulation

input to a home-built current limiter, which gates output of an external power supply (Hewlett Packard, model 6264B) to the longitudinal field coils discussed in Section A.2. The other voltage output channel is fed to the control input of a second power supply (Hewlett Packard, model 6675A) that is directly connected to the transverse field coils. In practice, the control voltages range from 0 to 10 V with 2.5 mV resolution, while the current-control circuitry for the longitudinal and transverse fields provides 2.24 and 2.87 A per volt of modulation input, respectively. This translates to 0.12 mT (1.5 kHz) longitudinal and 0.05 mT (0.65 kHz) transverse field resolutions, where the parenthetical values provide the field resolution in units of ^{71}Ga resonance frequency.

The timing of field-cycling events for ONMR experiments with pointwise time-domain evolution in t_1 and LBD in t_2 is shown in Fig. 2.10, where part (a) depicts the timeline (not to scale) of rf excitation of the signal nucleus. Delays following ONP and evolution accommodate *adiabatic* field cycling, during which magnetization along the initial direction of the static field follows to the new orientation. Fig. 2.10(b) contains plots of recorded field-cycling events in which the

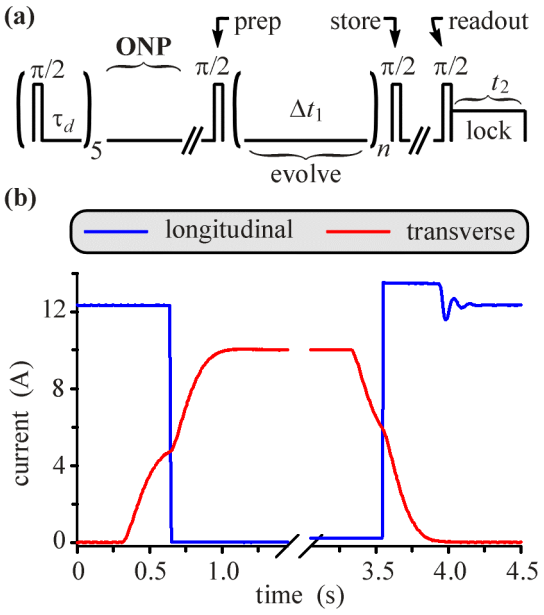

FIG. 2.10 **(a)** Sequence of rf excitation of the signal nucleus for a pointwise time-domain evolution in t_1 with LBD in t_2. **(b)** The magnet current level in the longitudinal and transverse field coils plotted on a timeline that represents the sequence of a Larmor-beat-detected ONMR experiment that requires a transverse field during the NMR evolution period.

longitudinal field is set high for the opening segment, which coincides with ONP. Following that period, the transverse field is cycled to half its final value in about 300 ms, at which time the longitudinal field is dropped to zero and the cycle to the ultimate transverse field value is initiated. The total time required for a cycle from a longitudinal field of 246.5 mT to a steady-state transverse field of 57.8 mT is 2.1 s. Use of the two-step sequence prevents level crossing of the nuclear Zeeman energy levels, thus avoiding corresponding fast relaxation of the spin order obtained during ONP. The second cycling event begins at the end of the NMR evolution period, and is sandwiched between a pair of $\pi/2$ pulses. The first of these pulses stores the spin magnetization that survives NMR evolution along the static field, which is then adiabatically cycled. The second $\pi/2$ pulse turns spin magnetization into the transverse plane for readout during the detection period. The second field-cycling event is an approximate reversal of the first two-step process, and requires 700 ms.

The adiabatic condition[65] for these field-cycling events, which ensures that nuclear spin magnetization follows the field during its reorientation, requires that

$$\left(\nu_c / \gamma_n B_{tot}\right) \ll 1 , \tag{2.2}$$

where ν_c is the instantaneous rate of field reorientation, γ_n is the gyromagnetic ratio of an isotope in the spin system, and B_{tot} is the instantaneous magnitude of the total field. In GaAs, ^{75}As is the species with the smallest γ_n, and, therefore, places the most restrictive limitation on the cycling rate. The unitless reduced rate that is the left-hand side of Eq. (2.2) is plotted in Fig. 2.11 for the cycling event immediately following ONP. This

result, and a similar one that corresponds to the second cycling event, demonstrates our fulfillment of the adiabatic requirement.

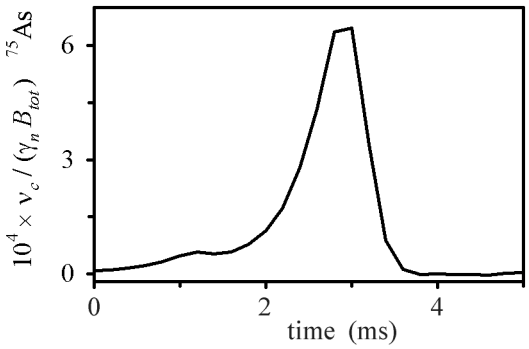

FIG. 2.11 The ^{75}As reduced cycling rate for the cycling of the total field in the first step of the two-step cycling sequence shown on the timeline of Fig. 2.10. The reduced rate easily satisfies the adiabatic requirement of Eq. (2.2).

III. Characteristics of a Single AlGaAs/GaAs Heterojunction: the *H*-band Luminescence

In this and the following chapter, I present experiments on a modulation-doped *p*-channel $Al_xGa_{(1-x)}As/GaAs$ ($x = 0.36$) single heterojunction grown by molecular beam epitaxy (MBE). The detailed layer profile and energy band diagram of this sample are shown in Fig. 3.1, where discrete hole states on the GaAs side of the interface comprise the *p*-channel along the sample plane. Heterojunction samples of this type have generated interest due to the so-called *H*-band[27] features in the photoluminescence (PL) spectrum, which are red shifted by 6 - 12 meV (5 - 10 nm) from the bulk-excitonic features and present only at low temperatures (< 10 K) in samples that contain an abrupt interface.

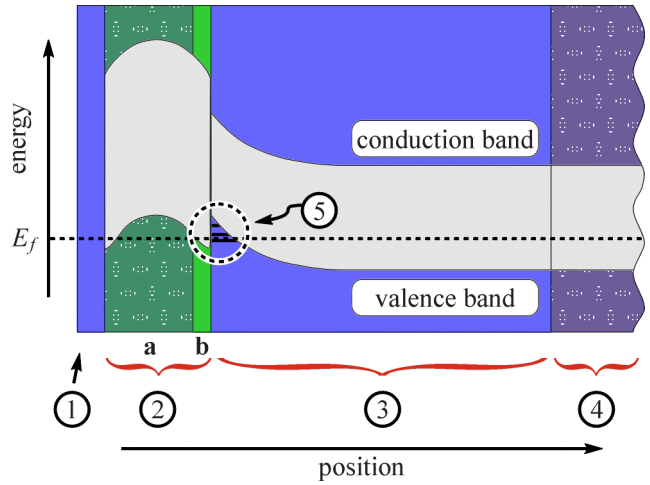

FIG. 3.1 Schematic of the layer structure and energy bands of our MBE-grown $Al_xGa_{(1-x)}As/GaAs$ ($x = 0.36$) modulation-doped *p*-channel heterojunction sample. Layer (1) is a 21 nm GaAs surface cap that provides chemical stability in air. Layer (2) is modulation-doped *p*-type $Al_xGa_{(1-x)}As$, in which the topmost 30 nm (a) is beryllium doped at 6×10^{17} cm^{-3} and followed by a 6.5 nm undoped spacer layer (b). Layers (1) and (2) are transparent to the 802.1 nm excitation used in our experiments, since the energy gap of the cap layer is perturbed by surface and quantum confinement effects, while the AlGaAs gap is well above the excitation energy. Layer (3) is the "active" layer of the sample and consists of 2500 nm of undoped GaAs grown in the [001] direction on a GaAs substrate (4). The Fermi energy E_F is in the GaAs gap near the valence band edge, while band bending yields hole-occupied discrete states in the interface notch (5).

The nature of the electronic states that give rise to the *H*-band PL has been a matter of some debate.[27-29,66,67] In their early work, Yuan, *et al*.[66] proposed an excitonic model, while others[28] suggested that the recombination of free and donor-bound electrons with 2D holes at the interface yields the so-called *e* and *d* lines, respectively, of the *H*-band. More recent work seems to confirm the excitonic model, in which the PL energy shift relative to bulk exciton features is attributed to the spatially indirect character of excitons in a region where the bands slope due to the tail of the interfacial electric field.[67] Within this model, the possibility remains that the *e* and *d* lines of the *H*-band distinguish free and bound excitons perturbed by the interface.

These models for the *H*-band photoelectronic system are rich with features that are uniquely quantifiable by ONMR, and which, upon their characterization, can aid in settling the debate over the origin of the *H*-band. Relevant observables include the interfacial electric field and the single-carrier distributions of electric field and spin density. These properties of the electronic system are held in common with other systems that are accessible by ONMR, such as quantum dots and wells. Thus, studies of this *p*-channel heterojunction represent progress toward characterization of a broad and important class of structured semiconductor materials.

In this chapter, I provide a brief discourse on previous optical spectroscopic studies of the *H*-band, and include characterization of our own sample with measurement of the circular polarization (CP) of each individual component of the PL spectrum. According to Eq. (1.10), the latter experiments measure the spin orientation of the electrons that recombine with thermalized holes to yield luminescence. This independent measure of the spin order related to each feature in the PL spectrum identifies those

luminescent features that are potential carriers of an optically detected NMR signal. Having thus established the relation between the *H*-band and our optically detected NMR signal, we exploit the response of nuclear spins to an electric field in order to probe the interfacial field at the sites of the recombinations that yield the *H*-band PL. This measurement distinguishes between the magnitudes of the interfacial field expected at recombination sites that correspond to the two proposed electronic models. Finally, the results presented in this chapter set the stage for the far more detailed electronic-state characterization provided by the POWER NMR experiments presented in Chapter 4. There the *spatial distributions* of single-photocarrier spin and charge are respectively measured via Knight shift and electric-field-induced quadrupole interactions of lattice nuclei.

A. The Photoluminescence Spectrum

1. Characteristics of the *H*-band

The PL spectrum of our heterojunction sample is shown in Fig. 3.2 and was collected at 4 - 5 K with Ar^+ laser excitation at 514.5 nm (Spectra Physics, model 2020) and a 1 m monochrometer (SPEX, model 1704) that provided 0.2 nm resolution. The spectrum exhibits bulk excitonic features in the range 818 - 819 nm, as well as the *e* and *d* lines of the *H*-band near 823 and 825 nm, respectively, and a band-to-acceptor carbon (BA_C) transition near 832 nm. The PL spectrum of the same sample, but collected under the conditions used in a typical ONMR experiment, is shown in Fig. 3.3. The result qualitatively matches that of the first spectrum, as described in the figure caption. Our primary interest is in the *H*-band features of the PL. Yuan, *et al*.[27,66] proved the

existence of a relationship between the heterojunction interface and the *H*-band by collecting the PL spectra corresponding to a series of such heterojunction samples. The AlGaAs layer was etched progressively across the series and the *H*-band features vanished in those samples where the interface was removed completely.

Further studies probed the nature of the *H*-band-to-interface relationship, revealing that its red shift relative to the free exciton depends both on experimental conditions and the details of the sample structure. The work of Yuan, *et al*.[27,66] and investigations by Ossau and coworkers[28] showed that the red shift decreases with the optical excitation power. Meanwhile, experiments at a power low enough (1 - 10 W/cm^2) that the red shift is maximized showed its increase with *p*-doping level and %Al in the AlGaAs layer, as well as with decreasing thickness of the undoped AlGaAs spacer.[27,28] The dependence on dopant and Al concentrations and on the spacer thickness may be attributable to corresponding changes in the energy band profile that manifest in a larger interfacial electric field. Similarly, reduced excitation power may diminish screening of that field by photocarriers at the interface. The net implication is that the *H*-band red shift increases with the interfacial field, due to some influence of that field on the electronic states whose recombinations give rise to the *H*-band.

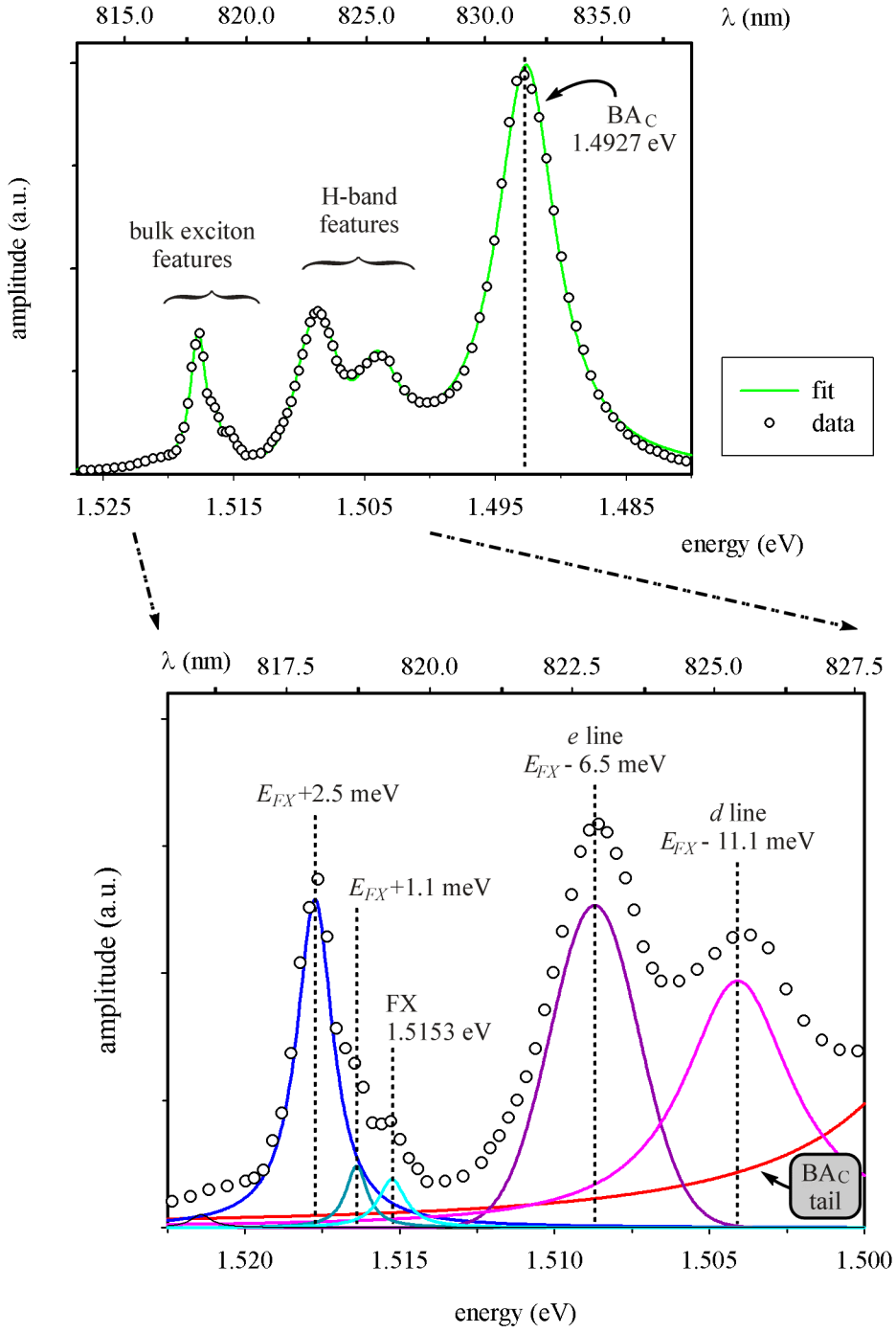

FIG. 3.2 The PL spectrum (points) and fit (line) of the $Al_{0.36}Ga_{0.64}As/GaAs$ heterojunction sample. The fit to the entire spectrum is composed of individual Lorentzian components, which are plotted and labeled according to their apparent energies relative to the ground-state free exciton energy, $E_{FX} = 1.513$ eV. The *e* line, however, differs from the other features in that the best fits to the entire spectrum, including that shown above, required a Gaussian at the corresponding energy. The free exciton and band-to-carbon-acceptor (BA_C) peak assignments are based on literature values.[68,69]

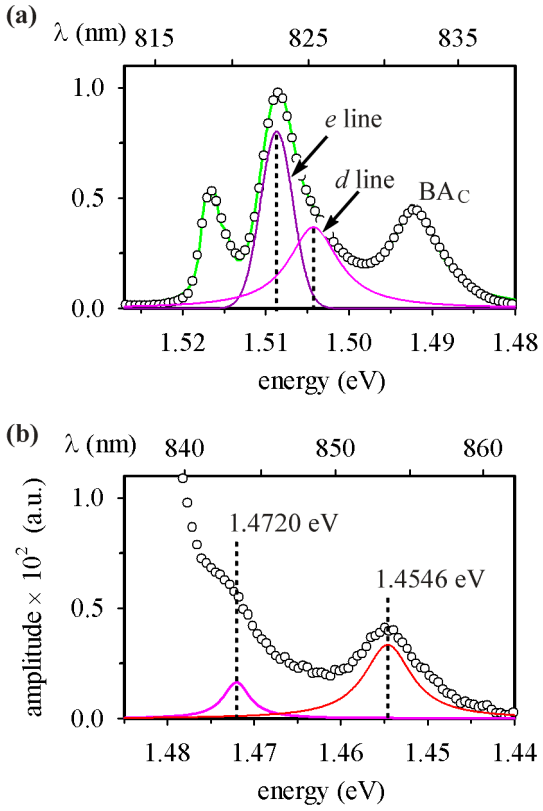

FIG. 3.3

(a) The PL spectrum (points) and fit (line) of the same sample, in this case collected in the ONMR apparatus. The sample was at 2 K in a 246.5 mT field that was mutually parallel to the sample growth direction and the propagation axis of the right circularly polarized excitation at 802.1 nm and 2.0 ± 0.5 W/cm^2. The Ocean Optics spectrometer (model PC 2000) discussed in Chapter 2 provided 1 nm resolution. The fit to the entire spectrum consists of the same components used for the spectrum in Fig. 3.2 and yielded qualitatively similar results. Here, the *e* and *d* lines are 6.5 and 11.0 meV below E_{FX}, and the intensity of the H-band is increased relative to that of both the bulk exciton features and the BA_C transition.

(b) Two PL features at energies higher than the collected range of the spectrum in Fig 3.2 are revealed here and shown for completeness. The arbitrary amplitude units are directly comparable those in (a). No assignment for the peak at 1.4546 eV has been found, although the higher energy peak is close to the 1.4722 eV expected for a donor-to-Ge-acceptor transition.[69]

2. Electronic Models for the *H*-band Luminescent States

Two electronic models for the *H*-band states have been proposed, each of which is consistent with the noted dependence on the interfacial field. Yuan, *et al*.[27] suggested the first, which has since been investigated by others.[28,70] Therein, free or donor-bound electrons in the conduction band tunnel to the interface region and recombine with 2D holes in an interface subband. In this case, an increase in interfacial field, or, equivalently, in the slope of the energy bands at the interface, would correspondingly increase the *H*-band red shift as the valence-band-hole potential well at the interface deepens. The second model for the *H*-band electronic states was put forth in a subsequent paper by Yuan and coworkers,[66] and later explored by Shen, *et al*.[29,67,71]

Therein, the *H*-band is presumed to be due to excitonic recombination at a distance from the interface where the attractive polarizing force of the interfacial field on the exciton balances with the Coulombic attraction of the electron-hole pair. This model is schematized in Fig. 3.4. The binding energy E_b of the polarized exciton is reduced due to the quadratic Stark interaction, which provides a small *blue shift*,

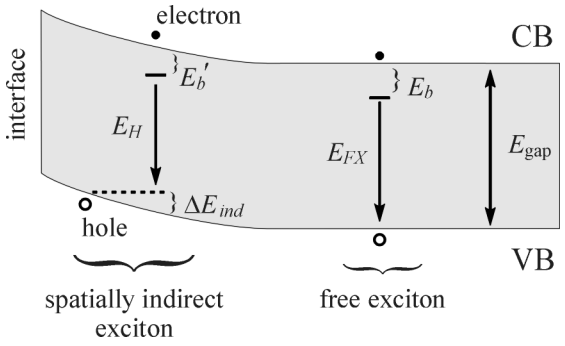

FIG. 3.4 Comparison of the energies of a free exciton (FX) and one perturbed by an electric field such as that due to the interface in an AlGaAs/GaAs heterojunction. The slope in the valence (VB) and conduction (CB) energy bands gives the value of the field. The binding energy E_b' of the perturbed excitons is less than that of the FX, resulting in a small blue shift of the transition. However, the net shift that appears in the PL spectrum is red due to the shift ΔE_{ind} that results from the spatially indirect nature of the recombination.

$$\Delta E_b = E_b - E_b', \tag{3.1}$$

relative to the free-exciton recombination energy. However, the band slope also renders the excitonic recombination spatially indirect, yielding a red shift ΔE_{ind} that outweighs ΔE_b in determining the net shift relative to the bulk excitonic feature.

Previous attempts to distinguish between these two models provide conflicting evidence. Ossau, *et al*.[28] observed a linear shift of the *H*-band PL to higher energies with a magnetic field applied parallel to the interface. The observed shift matches that which is expected for free-electron Landau levels. Meanwhile, these authors also found that the *H*-band split into four CP components with a magnetic field applied along the surface normal, and that these components each exhibited an apparently linear shift with the magnitude of that field. From this it was inferred that one set of carriers involved in

the *H*-band transition, presumably the holes, is confined at the interface. Such 2D carriers are relatively insensitive to a magnetic field parallel to the interface, as that field can induce a cyclotron motion that is restricted by the confining potential. The analogous in-plane motion incurred by a field along the surface normal is much higher in energy. Combining these arguments, Ossau, *et al*. concluded that the *H*-band is due to recombination of a free (or donor-bound) electron with a 2D interfacial hole.

In direct contrast to the above results, the experiments of Shen and coworkers[67] support an excitonic model. This group observed a nonlinear diamagnetic shift of the *H*-band to higher energy with a magnetic field oriented either perpendicular or parallel to the interface plane. This implies that the *H*-band is of excitonic origin, since an initial state that includes one or more free carriers would exhibit *linear*, *paramagnetic* energy dependence that is larger than the observed nonlinear shift. Furthermore, these authors pointed out that, according to the so-called phase-filling effect,[72] excitonic transitions cannot involve 2D carriers.

Based on these observations, Shen, *et al*. proposed[29,67,71] a dynamic model for the formation of excitons that are polarized by the interfacial field to yield the red-shifted *H*-band luminescence. The mechanism is depicted in Fig. 3.5, and begins with photoexcitation of an electron-hole pair, followed by relaxation of each carrier to its band edge and spatial transport under the influence of the interfacial field. Finally, the electron and a second hole, which was photoexcited nearer to the flatband region, trap each other to form a polarized exciton whose recombination yields the *H*-band luminescence.

Time-resolved PL experiments on analogous *n*-type samples, in which the carrier transport is reversed in direction relative to Fig. 3.5, provide evidence to support this

dynamic model.[29,67] In those studies, Shen, *et al*. observed that the free-exciton PL had a decay rate typical of that in bulk samples, but also exhibited a unique two-component rise time. A fast, tens-of-picoseconds rise in the PL signal is attributed to direct exciton formation in the flatband region, while a subsequent 1 - 2 ns rise is linked to exciton formation like that shown in Fig. 3.5, but where the electron and hole joined and recombined in the flatband region. It is reasonable to expect that similar exciton formation occurs nearer to the interface, yielding polarized excitons that energetically match the *H*-band.

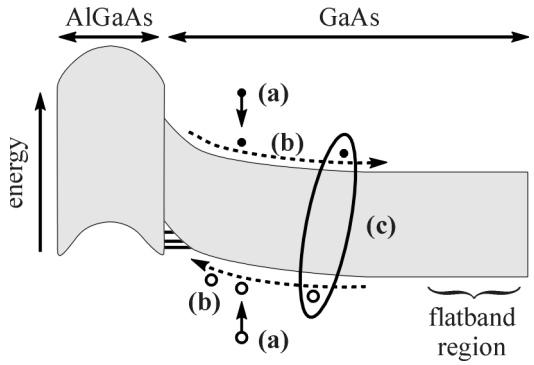

FIG. 3.5 Dynamic model for formation of *H*-band electronic states proposed by Shen, *et al*.[67,71] **(a)** Photoexcitation of an electron-hole pair. **(b)** Carrier drift in the interfacial field. **(c)** Polarized exciton formation.

The final piece of evidence with which Shen, *et al*. connected the *H*-band to excitons results from their PL experiments with concurrent microwave irradiation of a cyclotron resonance of the 2D holes in *p*-type samples.[67] The microwave irradiation served to heat the interface region and, by association, nearby photoexcited electrons. The increased energy of these electrons presumably carried their trajectory to a greater distance from the interface prior to exciton formation of the sort in part (c) of Fig. 3.5. As evidence of this process, the authors observed a reduction in the *H*-band PL with a corresponding increase in free exciton emission and zero net change in PL intensity.

B. Characterization of the Interfacial Electric Field

As recounted above, previous authors have established the existence of a relationship between the *H*-band electronic states and the heterojunction interfacial field. However, contrasting models for these electronic states have been proposed. The most recent and compelling results suggest an excitonic model, but that evidence is indirect and has not discounted the possibility of recombination involving 2D interfacial holes. An as-yet-uncharacterized feature that can distinguish between these two models is the magnitude of the interfacial field at the recombination sites. In this section, I present a calculation of the interfacial-field profile and estimate its magnitude at distances from the interface that could reasonably correspond to the two models for the *H*-band electronic states. Finally, I present the results of optically detected NMR experiments in which the *H*-band PL serves as the NMR signal carrier, as established by analysis of the CP of features contributing to the entire PL signal. The ONMR experiment measures the value of the interfacial field at the sites responsible for NMR, which in turn are the sites of *H*-band recombination. The result clearly distinguishes between the values of the interfacial field expected for the two contending models for the *H*-band electronic states.

1. The Exciton Dissociation Limit

The interfacial field at the possible sites of excitonic recombination in the model of Shen, *et al*. is limited by field-induced dissociation of the electronic state. In quantum wells, the quantum-confined Stark effect[73,74] can yield an energy shift of the excitonic luminescence corresponding to up to 50 times the classical ionization field $\varepsilon_i = (E_b / 8\, e\, a_x)$, where a_x is the exciton Bohr radius. However, in bulk samples, the shift

is limited by dissociation to ~ 10% E_b.[74,75] The same is true in a single heterojunction, where one-sided confinement allows escape of the carrier that is repelled by the interfacial field. An estimate of the corresponding dissociation-limited electric field is made using perturbation theory to calculate corrections to E_b, which in turn are held to 10% of the unperturbed energy.

An exciton is described by the spatial hydrogenic wave function

$$\begin{aligned} \Psi_{nlm}(\mathbf{r}) &= Y_{lm}(\theta,\phi)R_{nl}(r) \\ &= \langle \mathbf{r} | n\, l\, m \rangle, \end{aligned} \tag{3.2}$$

where $\mathbf{r} = (r, \theta, \phi)$ is the relative electron-hole coordinate, n, l and m are usual quantum numbers labeling the spherical harmonic $Y_{lm}(\theta, \phi)$ and radial $R_{nl}(r)$ factors, and the second line expresses the function in Dirac notation. The associated exciton Bohr radius is

$$a_x = a_B(\kappa/\mu_x), \tag{3.3}$$

where $\kappa = 13.1$ is the GaAs dielectric constant, a_B is the Bohr radius of the hydrogen atom and μ_x is the reduced mass of the exciton composed of electron and hole with effective masses m_e and m_h, respectively. The perturbation Hamiltonian for an interfacial electric field ε_{int} along the z-axis is

$$\mathcal{H}_\varepsilon = (-e\,\varepsilon_{int}\,z) = (-e\,\varepsilon_{int}\,r\cos\theta). \tag{3.4}$$

The corresponding first-order perturbation theory correction to the ground-state energy is

$$E_1^{(1)} = -e\varepsilon_{int}\,\langle 100 | z | 100 \rangle, \tag{3.5}$$

which vanishes by symmetry. The second-order correction is

$$E_1^{(2)} = \left(e\varepsilon_{int}\right)^2 \sum_{n\neq 1,\, l,\, m} \frac{\left|\langle 100 | \, r\cos\theta \, | n\, l\, m\rangle\right|^2}{E_1^{(0)} - E_n^{(0)}}. \tag{3.6}$$

This is simplified using the relationships[76]

$$E_n^{(0)} = n^{-2} E_1^{(0)} \tag{3.7}$$

and

$$\cos\theta \; Y_{lm}(\theta,\phi) = A\, Y_{l+1,\,m}(\theta,\phi) + A'\, Y_{l-1,\,m}(\theta,\phi), \tag{3.8}$$

where

$$A = \sqrt{\frac{(l+m+1)(l-m+1)}{(2l+1)(2l+3)}} \qquad \text{and} \qquad A' = \sqrt{\frac{(l+m)(l-m)}{(2l+1)(2l-1)}}. \tag{3.9}$$

Substituting Eqs. (3.7) - (3.9) into Eq. (3.6) and using the orthonormality of the $Y_{lm}(\theta, \phi)$, we obtain

$$E_1^{(2)} = \frac{\left(e\varepsilon_{int}\right)^2}{3E_1^{(0)}} \sum_{n\neq 1} (1-n^{-2})^{-1} \left| \int_0^\infty r \; R_{1,0}(r) \; R_{n,1}(r) \; dr \right|^2. \tag{3.10}$$

To estimate this correction in GaAs, we insert $m_e = 0.067\, m_0$, and the heavy-hole mass, $m_{hh} = 0.465\, m_0$, where m_0 is the free electron rest mass, into Eq. (3.3) for a_x, which appears in the factors $R_{1,0}(r)$ and $R_{n,1}(r)$ (see, for example, Dykstra[77]). Substituting the resulting radial functions and $E_b = 4.2$ meV[78] into Eq. (3.10), and truncating the sum at $n = 5$ yields

$$E_1^{(2)}(\text{GaAs}) = 0.29_2 \text{ meV/(kV/cm)}^2. \tag{3.11}$$

Satisfaction of the requirement that $E_1^{(2)} \leq 0.1\, E_b$ determines the dissociation-limited electric field of 1.2 kV/cm. For the light-hole mass, $m_{lh} = 0.082\, m_0$, and the calculated corresponding binding energy $E_b = 2.9$ meV, the dissociation limit is instead 0.52 kV/cm.

2. Self-Consistent Calculation of the Interfacial Field

The band structure of the AlGaAs/GaAs heterojunction sample with the layer and doping profile shown in Fig. 3.1 was calculated numerically using a self-consistent Schrödinger-Poisson solver. Relevant parameters of the calculation include: a dielectric constant of 13.0[3(a)] in both materials, background *p*-type doping of 3×10^{14} cm^{-3}, a valence-band offset at the AlGaAs/GaAs interfaces of 35% of the total gap difference, and energy pinning at the surface (i.e., of the GaAs cap) and substrate of 0.7 eV, which corresponds to the mid-gap of GaAs. The program accounts for only one type of hole; however, since the heavy-light hole degeneracy is removed at the interface, previous authors have neglected the lower energy light-hole levels in calculating the interfacial subband states.[28] Therefore, I have assumed the GaAs heavy-hole mass, $m_{hh} = 0.465\ m_0$.

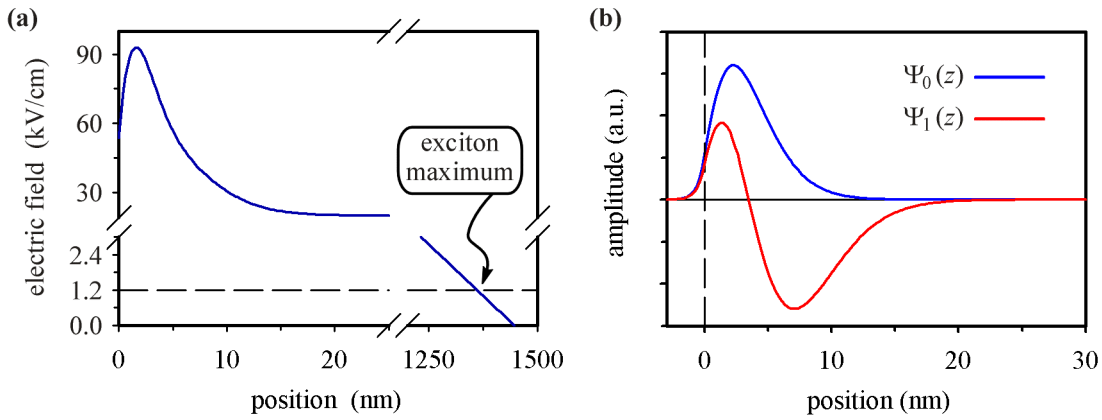

FIG. 3.6 **(a)** Calculated 1D profile of the interfacial electric field. The position axis is labeled relative to distance from the interface on the GaAs side of the (non-cap) heterojunction. Note the changes in scale at each break. **(b)** The normalized envelope wave functions of corresponding occupied hole states.

[3(a)] The Schrödinger-Poisson solver used here accepts a dielectric constant no greater than 13.0, while the accepted value in GaAs is 13.1.[79] Since the source code is not immediately available for incorporation of changes allowing the larger value, I have proceeded using the maximum and note that resulting differences in output are inconsequential to the qualitative assessment of the interfacial field and states sought here.

The calculation was executed on a 1D grid with 2 Å spacing from the surface to a distance of 60 nm beyond the (non-cap) heterojunction interface, while a 60 Å increment was used from that point out to the substrate.

The resulting profiles of the interfacial electric field and the envelope wave functions of the occupied discrete hole states are plotted in Fig. 3.6. If the *H*-band luminescence is due to the recombination of free electrons with the interfacial holes represented by the envelope functions in Fig. 3.6(b), then the electric field at the recombination sites should be $\gtrsim 25$ kV/cm according to the result plotted in Fig 3.6(a). This is in stark contrast to the ~1.2 kV/cm dissociation-limited field for excitonic recombination, which, as indicated in the figure, corresponds to a distance from the interface in excess of 1 μm.

3. NMR Measurement of the Interfacial Field

In noncentrosymmetric crystals such as GaAs, there exists a linear quadrupole Stark effect (LQSE) whereby the nuclear resonance of spins $I \geq 1$ is split in proportion to an electric field.[25,60-62,80,81] Here, we exploit this interaction to measure the interfacial field at the sites responsible for the signal in an optically detected NMR experiment. We establish that the *H*-band PL serves as the NMR signal carrier with further optical experiments, and thus that the environment reported on by the NMR signal is that where the corresponding electronic states recombine.

i. The Linear Quadrupole Stark Effect

A detailed description of the LQSE is presented in Appendix B. In brief, an electric field at a noncentrosymmetric site perturbs the valence electronic states in the

lattice such that a field gradient arises at the nuclear sites. The magnitude of the induced gradient, and in turn the nuclear quadrupole interaction, is linear in the electric field. The observable quantity is a quadrupole splitting of the nuclear resonance, where, in the example of a spin $\frac{3}{2}$ such as any of the primary isotopes in GaAs, the degeneracy of $(+\frac{1}{2} \leftrightarrow -\frac{1}{2})$ and $(\pm\frac{3}{2} \leftrightarrow \pm\frac{1}{2})$ transitions is lifted, resulting in a symmetric 3:4:3 triplet.

The relevant form of the rotating-frame LQSE nuclear spin Hamiltonian is the time-independent part of Eq. (B.18) of Appendix B:

$$\tilde{\mathcal{H}}_Q(\alpha,\beta,\gamma) = \frac{eQ}{2I(2I-1)\hbar}\, T_{2,0}\, V'_{2,0}(\alpha,\beta,\gamma), \tag{3.12}$$

where e is the unit electric charge, Q is the nuclear quadrupole moment, $T_{2,0}$ is the spherical tensor operator given by Eq. (B.7) and the expression is in units of (radÿs^{-1}). The dependence of $\tilde{\mathcal{H}}_Q$ on the orientation of $\mathbf{B}_0$ with respect to the crystal axes is given by the Euler angles α, β and γ as discussed in the appendix, where Eq. (B.19) gives the explicit form of the component $V'_{2,0}(\alpha,\beta,\gamma)$ of the LQSE-induced electric-field-gradient tensor. Inserting that expression and Eq. (B.7) for $T_{2,0}$ into Eq. (3.12) and dropping the ineffectual term proportional to the identity operator, yields

$$\tilde{\mathcal{H}}_Q(\alpha,\beta,\gamma) = \tfrac{1}{2}\,\omega_Q(\alpha,\beta,\gamma)\, I_z{}^2, \tag{3.13}$$

where we have defined

$$\begin{aligned}\omega_Q(\alpha,\beta,\gamma) = {} & \frac{3eQC_{14}}{2I(2I-1)\hbar} \\ & \times \left[\sin 2\beta\ (E_{100}\sin\alpha + E_{010}\cos\alpha) + E_{001}\sin^2\beta\ \sin 2\alpha\right].\end{aligned} \tag{3.14}$$

E_{100}, E_{010} and E_{001} are the components of the electric field along the crystal axes indicated in the subscript and C_{14} is a constant describing the coupling between the electric field and the induced-gradient tensor, as discussed in Appendix B.

NMR evolution governed by the Hamiltonian of Eq. (3.13) is evaluated using the standard density matrix formalism to yield the rotating-frame time-domain NMR signal,

$$S(t) \;=\; Tr\Big[\, I_{+}\, \exp\!\left(-i\, \tilde{\mathcal{H}}_{Q} t\right)\; \rho(0)\; \exp\!\left(+i\, \tilde{\mathcal{H}}_{Q} t\right)\Big], \tag{3.15}$$

where $\rho(0)$ is the initial density matrix and it is understood that real and imaginary parts of the signal represent its two orthogonal components in the transverse plane. The initial condition is established by a $(\pi/2)_x$ preparation pulse on the optically pumped nuclear magnetization that yields $\rho(0) = A_0 I_y$ in the high-temperature approximation, where A_0 is a numerical constant that is derived in Section C.1 of Chapter 4. Substituting this and Eq. (3.13) into Eq. (3.15) yields

$$S(t) \;=\; A_0 \left(3e^{+i\,\omega_Q t} \;+\; 4 \;+\; 3e^{-i\,\omega_Q t}\right) \tag{3.16}$$

for a spin $\frac{3}{2}$. Fourier transformation of $S(t)$ reveals the triplet pattern noted above in which a central transition at dc in the rotating frame is sandwiched by two satellite peaks at frequencies $\pm\omega_Q/2\pi$.

Our apparatus can provide a static magnetic field in either of two orthogonal directions. With the sample orientation we have chosen, these place $\mathbf{B}_0$ along either of the [001] or [110] crystal axes, corresponding to $(\alpha, \beta, \gamma) = (0, 0, 0)$ or $(\frac{\pi}{4}, \frac{\pi}{2}, 0)$, respectively. Substituting these angles into Eq. (3.14), we obtain

$$\omega_Q(0, 0, 0) \;=\; 0\,, \tag{3.17}$$

and $$\omega_Q(\tfrac{\pi}{4}, \tfrac{\pi}{2}, 0) = \frac{3eQC_{14}E_{001}}{2I(2I-1)\hbar}. \qquad (3.18)$$

In the former case, NMR evolution is independent of the LQSE. Thus an experiment executed with $\mathbf{B}_0$ along [001] during the NMR evolution period serves as a control that is to be contrasted with the results of an experiment with $\mathbf{B}_0$ along [110]. According to Eqs. (3.16) and (3.18), the latter experiment allows for direct measure of the interfacial field via a quadrupole splitting that is linear in $E_{001} = \varepsilon_{int}$. For quantification of this result, the values of Q and C_{14} that correspond to the primary isotopes in GaAs are presented in Table 3.1. The last column presents the predicted splitting per unit electric field in the case that corresponds to Eq. (3.18), where $\mathbf{B}_0$ is along [110].

Table 3.1 The values of the LQSE coupling constant C_{14} and the nuclear quadrupole moment Q are listed for each isotope in GaAs, as are the corresponding quadrupole splittings per unit electric field along the [001] crystal axis in the case where $\mathbf{B}_0$ is along [110]. As suggested by Dumas *et al*.,[62] we use the largest reported C_{14} values, as all systematic errors in their determination tend to decrease their apparent size. Furthermore, only the product $C_{14}Q$ corresponding to each nuclear species is measurable by LQSE NMR (as reflected in the last column), thus the Q values assumed by Dumas *et al*. should not be replaced by more modern values without correspondingly scaling the C_{14} values.

Isotope	$C_{14}\times10^{-12}$ [m^{-1}]	$Q\times10^{29}$ [m^2]	$(\omega_Q/2\pi) / E_{001}$ [kHz / (kV/cm)]
^{69}Ga	2.85	1.9	0.65
^{71}Ga	2.85	1.2	0.41
^{75}As	3.16	2.9	1.11

ii. ONMR with the H-band

Before moving on to NMR characterization of the interfacial field, it is important to establish the relationship between the NMR signal and the *H*-band PL, i.e., we must show that among all PL features the *H*-band alone serves as the signal carrier in an optically detected NMR experiment. Recall from the introductory chapter that the only

lattice nuclei that contribute to the signal are those located in regions that appreciably overlap with the wave function of the luminescent electron. Therefore, the optically detected NMR signal reports on the environment at the sites of localization of electronic states that go on to produce optical recombination. When the PL is well resolved, optical filtering trivially establishes knowledge of the NMR signal carrier. However, in the present case, which is represented by the spectrum in Fig. 3.3, such optical resolution is not present and we must rely on further PL characterization to demonstrate that the *H*-band component of PL is the ONMR signal carrier.

Using the Larmor beat detection (LBD) method[9] described in Section B.4 of Chapter 1, we rely on the Hanle effect depolarization of PL to optically encode NMR evolution. Thus the optical signal carrier must exhibit some degree of luminescence polarization ρ and, furthermore, this quantity must be responsive to a transverse magnetic field, such as that provided by the lattice nuclei during LBD. The underlying physical processes that determine this response were discussed in Section B.2 of Chapter 1; however, the objective here is simply to measure the PL polarization of individual features in order to determine which region or regions of the PL spectrum are viable as an NMR signal carrier.

The polarization of the PL spectrum of our AlGaAs/GaAs heterojunction is shown in Fig. 3.7, and is similar to that observed from a sample of the same type by Krapf, *et al*.[15] Our result is the difference between two spectra in which either the right (σ_+) or the left (σ_-) CP component of PL was collected under the conditions used for ONMR, as detailed in the figure caption. Selection of a given polarization for detection was achieved by adjustment of the $\lambda/4$ optical element in the detection path, as described in Section C.2 of Chapter 2. The spectrum exhibits the largest degree of CP in the range corresponding to the *H*-band features. The bulk excitonic and BA_C features also reveal nonvanishing polarization. The reversal of the sign of ρ in the BA_C case indicates that the corresponding electron spin is antiparallel to that of the electrons yielding other PL features.

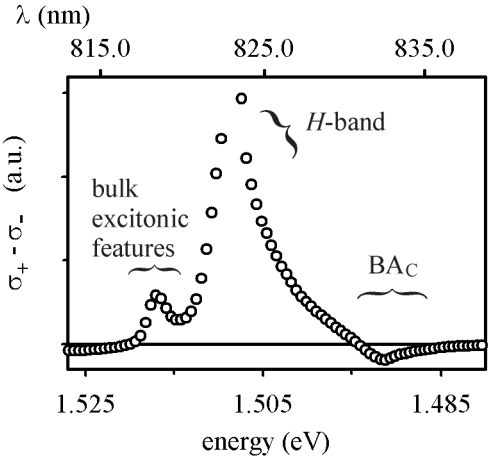

FIG. 3.7 Difference between the right and left CP components of sample PL. The spectra were collected in the ONMR apparatus at 2 K in a 246.5 mT field along the [001] growth direction and the propagation axis of the right CP excitation.

In order to quantify the polarization of contributing features, the spectra whose difference is shown in Fig. 3.7 were each fit with the set of line shapes used in characterization of the PL spectra of Figs. 3.2 and 3.3. We define the CP of the i^{th} individual feature as

$$\rho_i = \frac{A_i^+ - A_i^-}{A_i^+ + A_i^-}, \tag{3.19}$$

where $A_i^{\pm}$ is the area of the corresponding component of the fit to the spectrum in which $\sigma_{\pm}$ light was detected. The results of this analysis are presented in Table 3.2. The finite polarization of each PL feature indicates that all are apparently viable as optically detected NMR signal carriers. However, an additional clue as to the carrier identity in our experiments is revealed by inference of the average spin $\langle S \rangle$ of the recombining electrons from Eq. (1.10). In that expression, we take $\xi = \frac{1}{2}$ and the direction of spin polarization to be parallel to the unit vector $\hat{n}_d$ along the detection axis, thus yielding $\langle S \rangle = \rho$. In Chapter 4, I present experiments in which this quantity is independently measured via the distribution of NMR Knight shifts due to the same photoexcited states that are responsible for optical nuclear polarization (ONP) and optical detection. These indicate that $\langle S \rangle = 0.15_3$, which closely matches the PL results for the *e* and *d* lines, while excluding the BA_C feature as the NMR signal carrier since it is consistent with a Knight shift opposite in sign to that observed. Finally, exclusion of the bulk excitonic features in ONMR experiments is provided by the 832 ± 5 nm optical bandpass filter in the detection pathway as described in Section C.2 of Chapter 2. Convolution of the transmittance of this filter with the fit to the total PL spectrum collected under the conditions of ONMR yields the integrated relative contribution of each PL feature to the total optical signal collected during an ONMR experiment. As shown in Table 3.2, the filter effectively blocks the bulk excitonic features and the *e* line. Thus we conclude that the *d*-line of the *H*-band is the ONMR signal carrier.

Table 3.2 Circular polarization ρ of individual components of the heterojunction PL spectrum, along with their relative contributions to the collected optical signal during NMR experiments. As discussed in the text, the electron spin polarization $\langle S \rangle$ in the corresponding electronic state is equivalent to ρ.

PL feature	ρ, $\langle S \rangle$	filtered signal contribution
bulk exciton features[(a)]	0.06	0.02
e line	0.17	0.05
d line	0.16	1
BA_C	-0.04	3.3

[(a)] Fits to the PL spectra include three bulk excitonic features, as shown in Fig. 3.2; however, these were treated as a collective feature in calculating the corresponding ρ value.

iii. Measurement of the Interfacial field

The timeline of the NMR experiment is depicted in Fig. 3.8(a) and follows the general sequence (see Section B.4 of Chapter 1 and Section E of Chapter 2) for pointwise acquisition of the time-domain signal in t_1 with LBD in t_2. A spin-echo pulse sequence,[31] in which the evolution period is divided in equal halves by a π pulse on the signal nucleus, was used to remove broadening of the frequency domain spectrum by field inhomogeneity and reduce that due to heteronuclear dipolar coupling. During both ONP and optical detection, $\mathbf{B}_0$ was at 246.5 mT and along the [001] growth direction, as is standard in our experiments. However, during evolution, the field was oriented along either [001] (longitudinal), providing the control experiment discussed above, or [110] (transverse), where the sensitivity to the interfacial field is given by Eqs. (3.16) and (3.18). In either case, the field is cycled adiabatically at the breaks in the timeline to provide 57.8 mT during the NMR evolution period, which is approximately the maximum available from our transverse field coils without causing internal arcing.

The NMR signal nucleus was ^{71}Ga, which has a 750 kHz resonance frequency in the noted evolution field. The $\pi/2$ pulse duration on that isotope was 5.35 μs and the evolution increment Δt_1 was 3.3 μs, yielding a spectral width of 303.0 kHz. Time-proportional phase incrementation[53] (TPPI) of both the $\pi/2$ preparation pulse and the π pulse of the echo sequence with phases

$$\phi_1 = 2\pi \times (30\ \text{kHz}) \times t_1 \qquad \text{and} \qquad \phi_2 = 2\pi \times (-10\ \text{kHz}) \times t_1, \tag{3.20}$$

respectively, resulted in a net shift of the signal in the indirect dimension to

$$\nu_{\text{TPPI}} = \frac{\phi_1 - 2\phi_2}{2\pi t_1}, \tag{3.21}$$

or, in this case, 50 kHz. The ^{71}Ga spin lock during optical detection was at an rf field amplitude of $B_1^{sig} = 0.86$ mT (11 kHz Rabi frequency), while concurrent irradiation of the ^{75}As LBD reference nucleus was at $B_1^{ref} = 1.48$ mT (10.8 kHz Rabi frequency) and ~ 25 kHz above its resonance frequency in the 246.5 mT detection field.

The results of the longitudinal (i.e., the control) and transverse field experiments are shown in Fig. 3.8(b). Evolution in the longitudinal field yielded a 1.28 kHz FWHM Lorentzian centered at the TPPI frequency, where the line width reflects the distribution of homonuclear dipolar couplings among signal nuclei. The transverse-field experiment yielded a broader line shape with approximately the same area as in the control. This change is attributed to the introduction of quadrupole splitting by ε_{int} as discussed above.

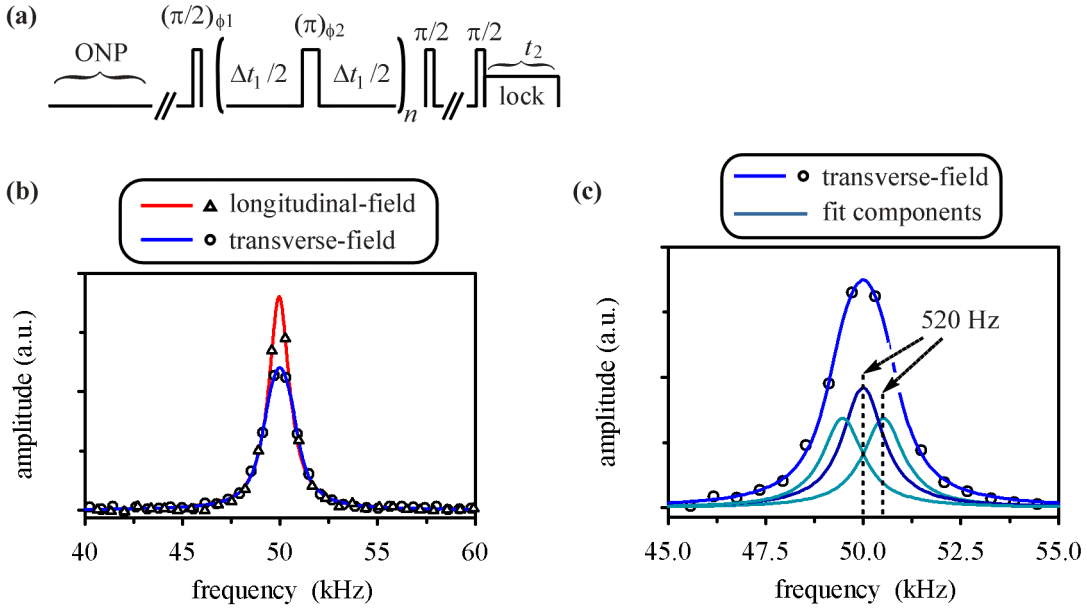

FIG. 3.8 **(a)** Spin-echo pulse sequence with field cycling delays. (See Chapter 2, Section E.) **(b)** Optically detected ^{71}Ga spin-echo spectra with evolution in longitudinal or transverse static field. Points and lines represent the data and corresponding fits, respectively. **(c)** Expanded view of the transverse-field spectrum with separate plots showing the three components of the 3:4:3 triplet fit function, which exhibits the indicated symmetric splitting.

Thus, the transverse-field spectrum was fit to a 3:4:3 triplet of Lorentzians, where the FWHM of each was fixed at that of the single peak obtained in the control experiment. The result of this fit is plotted with the data in Fig. 3.8(c) and places the two satellite peaks at approximately ± 520 Hz about the central transition. This corresponds to $\varepsilon_{int} = 1.2_6$ kV/cm, which is an upper bound on the interfacial field at the sites of the electronic recombinations that yield the *d* line of the *H*-band. Smaller field values may be at play if ε_{int} is inhomogeneous over the ensemble of electron-hole pairs that yield the *d* line, thus providing a distribution of LQSE-induced splittings. In that case, the satellite peaks would exhibit a breadth greater than the FWHM of the control and yield a more closely spaced triplet in the fit to the transverse-field data.

C. Conclusions

The NMR measurement of the interfacial field at the sites of *H*-band (*d* line) recombination is in remarkably good agreement with the expected value in the model of Shen, *et al*., where excitonic recombination should occur in a field near the 1.2 kV/cm dissociation limit. In contrast, the 25 kV/cm field expected at sites corresponding to recombination involving 2D interfacial holes would yield a ^{71}Ga quadrupole splitting of 10.3 kHz, which would be easily resolved in the experiment above. Therefore, the latter model is clearly excluded, and we conclude that the optically detected NMR signal is due to nuclei at a distance on the order of 1 μm from the *p*-channel heterojunction interface. There, the recombination of a polarized radial states, such as localized or free excitons, yields the *H*-band PL. To this point, another possibility remains open: that the ONMR signal is encoded in the spin of a donor-bound electron that delocalizes and forms a polarized exciton before recombination to yield the *H*-band PL. In Chapter 4, high-resolution POWER NMR experiments characterize distributions of Knight shifts and LQSE-induced splittings of nuclei in spatial overlap with the relevant electronic states, thereby distinguishing among these remaining candidates.

Acknowledgments

I would like to thank Dr. Frank J. Grunthaner and Dr. John Liu of the NASA Jet Propulsion Laboratory (JPL) for performing the MBE sample growth, and Dr. Alex Ksendov, also of JPL, who collected the PL spectrum shown in Fig. 3.2. Additionally, Dr. Doran Smith of the University of Maryland provided the code for calculation of the

interfacial electric field. I am grateful for this access as well as useful discussions with Dr. Smith regarding operation of the program.

IV. Imaging Single-Carrier Wave Functions with Optically Detected NMR

Our main goal in implementing ONMR for the study of III-V materials is the characterization of local electronic properties in structured samples. To that end, the technique provides two levels of resolution at which the spatial variation of these properties can be imaged. The first selects a local ensemble of nuclei from the bulk sample as the dominant source of the NMR signal. This guarantees that the NMR spectrum is, for example, due to the nuclei near a heterojunction interface, or to those in a quantum well or dot. At this level, one probes *average* properties of the local environment, such as the interfacial field measured in the previous chapter. A more finely divided view is available when one can resolve the spectral contributions of *individual nuclei* or subsets thereof in the local ensemble.[24-26,82] This second level of imaging, which is the focus of the current chapter, has been obscured in all previous ONMR experiments by the low spectral resolution typical of solid-state NMR in general and notoriously associated with optical detection in particular.

As discussed in the introductory chapter, the POWER NMR approach[24-26] provides orders-of-magnitude resolution enhancement over the few kHz dipolar limit in experiments where the imaged quantity can be cycled in synchrony with an NMR multiple-pulse sequence. This novel method provides, for the first time, access to the noted "second level" of imaging with ONMR. In this chapter, the prototypical POWER NMR experiments are presented in which the cyclic perturbation is provided by laser irradiation. Throughout this work, the sample is that discussed in Chapter 3: the *p*-channel $Al_xGa_{(1-x)}As/GaAs$ ($x = 0.36$) single heterojunction of Fig. 3.1. The *d*-line of

the *H*-band is the ONMR signal carrier, and, also as discussed in Chapter 3, is due to the radiative decay of a *bound* electronic state that is described qualitatively by a radial hydrogenic envelope function, such as that shown in Fig. 4.1.

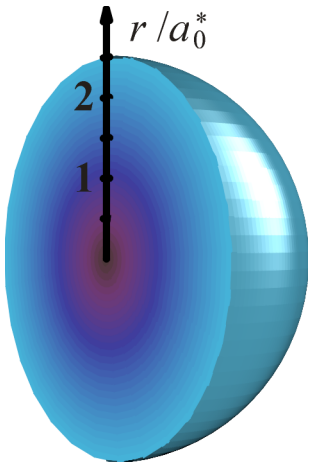

FIG. 4.1 Cross-sectional schematic representation of a hydrogenic radial envelope of a localized electronic state in GaAs. With a Bohr radius $a_0^* \sim 10$ nm, the electron has effective overlap with on the order of 10^6 nuclei.

In GaAs, such a state is characterized by an effective Bohr radius $a_0^* \sim 10$ nm and overlaps with on the order of 10^6 nuclear spins in a volume bounded at $r = 2a_0^*$ about the corresponding center of localization. These spins provide the optically detected NMR signal. With the POWER NMR approach, we can image the photoexcited wave function via the varied spectral response of these nuclei to optically switched Knight shift and linear quadrupole Stark effect (LQSE) interactions. The former yields a shift of nuclear resonance in proportion to the polarized electronic spin density at a given nuclear site, while the distribution of LQSE-induced quadrupole splittings in response to the optically switched electric field are sensitive to the distributions of *both* photoexcited electrons and holes. Radial resolution of these observables distinguishes between similar states that are consistent with the hydrogenic model, such as donor-bound electrons and excitons.

In this chapter, I present the most detailed NMR electronic-state characterization obtained to date. Experimental results probing optically induced (hyperfine) nuclear spin relaxation, Knight shifts and LQSE interactions are successfully modeled in terms of

single-nucleus spin physics summed over sites about a point defect in the GaAs lattice. This approach suffices for fitting results at short ONP times, though the experiment also provides a basis for including spin-diffusion effects at longer ONP times. The 2D analysis of such an experiment has uncovered the effects of spin diffusion on the NMR line shape, which deviate from one's expectations for isolated nuclei with a range of hyperfine interactions. An analogous experiment with optically induced electric fields is additionally sensitive to the fate of the optically induced hole via a linear Stark effect of the nuclear quadrupole Hamiltonian, yielding a more complete picture of the defect sites.

Finally, it is important to note that the experiments and analysis presented here represent significant progress in both optical NMR methodology and solid-state imaging techniques. Furthermore, while these advances are used to detail the particular *H*-band electronic system, they are applicable to a wide variety of structured semiconductor materials. Important examples include: (1) Single quantum dots, which are of interest for their optical properties and as test systems for quantum computing,[10-12,83-87] and (2) quantum wells and heterostructures, where recent experiments have uncovered surprising spin-dependent electronic transport,[13,88-93] and in which studies of exotic collective electronic states probe fundamental questions about the behavior of a confined Fermi sea.[19,20,22,23,94,95] In each of these examples, electron-nuclear interactions play an important role in the material properties, and ONMR in conjunction with the POWER methodology can provide unprecedented detail on the relevant underlying physics.

A. Optically Switched Nuclear Spin Interactions

1. The Magnetic Hyperfine Interactions

The interaction of a conduction-band electron with the nuclear spins in its vicinity is described in part by the magnetic hyperfine Hamiltonian. This operator includes terms describing the contact and dipolar interactions between the electronic and nuclear spins, and that between the nuclear spin and the orbital angular momentum of the electron. (See, for example, Cohen-Tannoudji.[96]) The Hamiltonians that govern these interactions are

$$\mathcal{H}_{hf}^{C,\,i} \;=\; -\tfrac{2}{3}\,\Gamma\,\mu_0\,g_0\,\mu_B\,\gamma_n^i\,\left|\Psi(\mathbf{r}_i)\right|^2\,\mathbf{I}^i\cdot\mathbf{S}\,, \tag{4.1}$$

$$\mathcal{H}_{hf}^{D,\,i} \;=\; -\tfrac{1}{4\pi}\,\Gamma\,\mu_0\,g_0\,\mu_B\,\gamma_n^i\,R_i^{-3}\left(3\left(\mathbf{I}^i\cdot\hat{n}_i\right)\left(\mathbf{S}\cdot\hat{n}_i\right)-\mathbf{I}^i\cdot\mathbf{S}\right), \tag{4.2}$$

and

$$\mathcal{H}_{hf}^{L,\,i} \;=\; -\tfrac{1}{4\pi}\,\Gamma\left(e\,\mu_0\,\gamma_n^i/m_e\right)R_i^{-3}\left(\mathbf{L}\cdot\mathbf{I}^i\right), \tag{4.3}$$

respectively, where each expression is in units of Hz, R_i is the instantaneous distance between the electron and the i^{th} nuclear center connected along a line with unit vector $\hat{n}_i$, and $\mathbf{L}$ is the electron orbital angular momentum operator. As noted in Section B.1 of Chapter 1, Γ is the occupancy of the electronic state, g_0 is the free-electron g-factor, and $\Psi(\mathbf{r}_i)$ is the value of the electronic wave function at the i^{th} nuclear center in the lattice.

The contact interaction provides the well-known Knight shift of nuclear resonance. The other interactions are less frequently noted and usually assumed negligible. In this section, I analyze whether this assumption is legitimately applicable to the optical NMR experiments presented in this thesis. Thus, I determine the relative magnitudes of these interactions as they exist in radial electronic states, such as those

describing electrons or excitons bound at point defects in the lattice. In GaAs, such states have vanishing electronic orbital angular momentum, and thus, $\mathcal{H}_{hf}^{L,i} = 0$. For $\mathcal{H}_{hf}^{C,i}$ and $\mathcal{H}_{hf}^{D,i}$, the spatial dependence of the interactions must be considered, and to that end analysis of a donor-bound electron, where

$$\left|\Psi(\mathbf{r}_i)\right|^2 = \left|\Psi_d(\mathbf{r}_i)\right|^2 = d_i\,\Omega\,\left|\psi_d(r_i)\right|^2, \tag{4.4}$$

provides a sufficient sense of their relative importance. In this expression, d_i is the element-dependent electron probability density within the unit cell at the nuclear center (see Table 4.1), and

$$\Omega = \tfrac{1}{4}a^3 \tag{4.5}$$

is the volume of a GaAs unit cell, where a is the GaAs lattice constant. The radial dependence is given by the hydrogenic envelope function

$$\psi_d(r_i) = \left(\pi\, a_d^{\,3}\right)^{-1/2} \exp(-r_i / a_d) \tag{4.6}$$

with effective Bohr radius

$$a_d = a_B(\kappa / m_e). \tag{4.7}$$

Inserting Eqs. (4.4) - (4.7) into Eq. (4.1) and taking $\mathbf{S}$ to be along $\mathbf{B}_0 // \hat{z}$ we obtain

$$\mathcal{H}_{hf}^{C,i} = -\gamma_n^i\,\mathbf{B}_e^{C,i}\cdot\mathbf{I}^i, \tag{4.8}$$

where I have defined the contact hyperfine field

$$\mathbf{B}_e^{C,i} = \left(\tfrac{2}{3}\,\Gamma\,\mu_0\,g_0\,\mu_B\,\langle S\rangle\,d_i\,\Omega\left(\pi\,a_d^{\,3}\right)^{-1}\exp(-2\,r_i / a_d)\right)\hat{z}. \tag{4.9}$$

The dipolar interaction between the nucleus at r_i and a donor-bound electron is equivalent to that of the nucleus with a point dipole at $r = 0$ and with effective spin

$$\mathbf{S}_{eff} = \langle S \rangle \left(4\pi \int_0^{r_i} \psi_d(r)\, r^2 dr \right) \hat{z}. \tag{4.10}$$

Substituting this result for **S,** r_i for R_i and $\hat{n}_i \cdot \hat{z} = \cos\theta_i$ in Eq. (4.2), yields

$$H_{hf}^{D,i} = -\gamma_n^i \mathbf{B}_e^{D,i} \cdot \mathbf{I}^i \tag{4.11}$$

where I have defined the dipolar hyperfine field

$$\begin{aligned} \mathbf{B}_e^{D,i} &= \tfrac{1}{4\pi} \Gamma \mu_0 g_0 \mu_B \langle S \rangle \left(3\cos\theta\, \hat{n}_i - \hat{z} \right) \\ &\quad \times r_i^{-3} \left(1 - \left(1 + 2(r_i/a_d) + 2(r_i/a_d)^2 \right) \exp(-2r_i/a_d) \right). \end{aligned} \tag{4.12}$$

For comparison with $H_{hf}^{C,i}$, we are interested in the maximum of $H_{hf}^{D,i}$, which is found along $\theta_i = 0$, where $\hat{n} = \hat{z}$. Furthermore, since our interest is in relative magnitudes only, choices for the occupancy, average electron spin and effective Bohr radius are arbitrary here, and I choose the maximum values $\Gamma = 1$ and $\langle S \rangle = \frac{1}{2}$, while taking $a_d = 10.37$ nm.

Table 4.1 The square of the conduction electron Bloch function at the centers of the primary isotopes in GaAs.[6]

isotope	$d_i \times 10^{-31}$ (m^{-3})
^{69}Ga, ^{71}Ga	5.8
^{75}As	9.8

The latter is determined by Eq. (4.7) using $\kappa = 13.1$ and $m_e = 0.067\, m_0$, as appropriate in GaAs; however, note that $\mathbf{B}_e^{C,i}$ and $\mathbf{B}_e^{D,i}$, expressed as functions of the dimensionless quantity (r_i/a_d), go with a_d^{-3}, and so this choice of Bohr radius does not bear upon the relative magnitudes of these fields. The contact hyperfine field is unique for each of Ga and As, according to the constants d_i in Table 4.1. The resulting radial profiles of the relative strengths of $\mathbf{B}_e^{C,i}(r_i)$ and $\mathbf{B}_e^{D,i}(r_i, \theta_i = 0)$ for both elements are plotted in Fig. 4.2 and clearly demonstrate that, for all primary isotopes in GaAs, the contact interaction is dominant among the magnetic hyperfine interactions for the radial states treated here.

Thus, I exclude the dipolar and orbital angular momentum terms in further treatment of optically switched spin interactions.

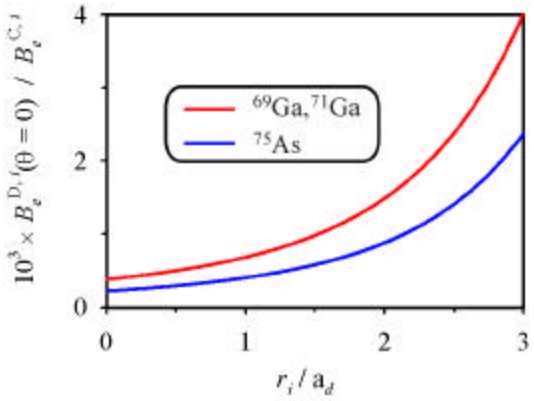

FIG. 4.2

Ratios of the radial profiles of the dipolar and contact hyperfine interactions for the primary isotopes in GaAs about a donor-bound electron. Contributions to the ONMR signal from beyond $(r / a_d) = 3$ prove negligible (*vida supra*).

2. The LQSE Revisited

In Chapter 3, the influence of the LQSE on nuclear spin evolution was introduced for the case in which a quadrupole splitting appears that is linear in the interfacial electric field ε_{int} of a single heterojunction. Such a field is directed along the [001] crystal axis and nearly uniform across the ensemble of nuclear spins contributing to the optically detected NMR signal. In the present section, we are interested in the sudden change in the local electric field brought on by optical excitation is of interest. In general, this field is neither uniaxial nor uniform at the atomic scale, and the corresponding quadrupole splitting is obtained by replacing E_{100}, E_{010} and E_{001} in Eq. (3.14) with their position dependent counterparts in the optically switched field, yielding

$$\omega_{Q,i}(\alpha,\beta,\gamma) = \frac{3eQC_{14}}{2I(2I-1)\hbar} \times \left[\sin 2\beta\,(E_{100}(\mathbf{r}_i)\sin\alpha + E_{010}(\mathbf{r}_i)\cos\alpha) + E_{001}(\mathbf{r}_i)\sin^2\beta\,\sin 2\alpha\right]. \tag{4.13}$$

Evaluating this expression requires modeling the fates of the electron *and* the hole provided by photoexcitation. Thus measurement of the photoexcited LQSE is complementary to that of the contact hyperfine interaction, which depends only on electronic spin density, since hole-nuclear spin interactions are relatively weak.[4]

B. Radial Resolution of the Optical Knight Shift

In this section, several POWER NMR experiments for high-resolution characterization of optically induced Knight shifts are presented. The shifts are due to the interaction of lattice nuclei with the same electronic state that provides the optical NMR signal carrier. Experimental conditions and parameters that, unless otherwise noted, apply to each of the experiments in this section are as follows. Filtering of the photoluminescence was employed as described in Section B.3.*ii* of Chapter 3, and thus the *d* line of the *H*-band is the NMR signal carrier. Whether implemented for ONP, optical detection or during NMR evolution, optical excitation was at 802.1 nm, right circularly polarized and propagating parallel to $\mathbf{B}_0$, thus providing electron spins that are antiparallel to $\mathbf{B}_0$ // [001] (see Section B.1 of Chapter 1). Experimental timelines follow the usual order for collection of a pointwise time-domain NMR spectrum in t_1 with Larmor beat detection (LBD) in t_2 (Fig. 1.11), while durations of ONP and the spin-locked optical detection period were $t_{\mathrm{ONP}} = 4.992$ s and $t_{lock} = 2.256$ s.[4(a)] The signal nucleus was ^{71}Ga at a resonance frequency of 3.2 MHz in the 246.5 mT static field, and off-resonance irradiation of the LBD reference nucleus (^{75}As) was employed as described

[4(a)] An artifact our programming code for the AWG502 rf synthesizer requires that each segment of the experiment timeline be an integer multiple of 200 times the CLSW-16 cycle time. Thus, for example, we use $t_{ONP} = 4.992$ s, rather than 5 s.

Section B.3.*iii* of Chapter 3. The CLSW-16 multiple-pulse sequence was used during the evolution period of all POWER NMR experiments with a standard cycle duration of $t_c = 120$ μs. Radiofrequency homogeneous offsetting was implemented as in Fig. 1.13(b) to provide a frequency shift [determined by Eq. (1.35)] in ω_1, the Fourier-transformed t_1 dimension. Typical $\pi/2$ pulse times and offset duration ranged from $t_p = 2.90 - 3.45$ μs and $t_{off} = 100 - 200$ ns, resulting in an offset frequency in ω_1 of about half Nyquist's frequency of $(2\, t_c)^{-1}$. This homogeneous offset is labeled as the origin of the frequency axis in the figures of this chapter.

1. A Qualitative View of the Electronic Wave Function

The pulse sequences used for POWER NMR characterization of optically induced Knight shifts are shown in Fig. 4.3(a) – (c). The sequence in (a), which is free of optical perturbations, provides the so-called "light-off" control spectrum, while the "light-on" sequences in parts (b) and (c) are designed to measure Knight shifts described by $\mathcal{H}_{hf}^{C,\,i}$ of Eq. (4.1). Spectra collected using each of the three sequences are shown in part (d) of the figure. In the following, I develop a formal expression for the resulting average Hamiltonian describing the optically induced Knight shifts, and then continue with a qualitative analysis of the relation between the spectra in Fig. 4.3(d) and the radial electronic state shown in the figure inset.

The rf excitation in each of the sequences (b) and (c) is identical to that of (a). However, shaded windows in the light-on sequences indicate the placement of optical pulses that introduce the Knight-shift interaction to the average Hamiltonian $\overline{\mathcal{H}}^{(0)}$, which

governs net NMR evolution over integer multiples of t_c. Optically induced contributions to $\bar{\mathcal{H}}^{(0)}$ derive from the secular part of the rotating-frame representation of $\mathcal{H}_{hf}^{C,\,i}$:

$$\tilde{\mathcal{H}}_{KS}^{\,i} \;=\; \left(-\tfrac{2}{3}\,\Gamma\,\mu_0\,g_0\,\mu_B\,\gamma_n^i\,\langle \mathrm{S}\rangle\,\left|\Psi(\mathbf{r}_i)\right|^2\right) I_{z,\,i}\,, \tag{4.14}$$

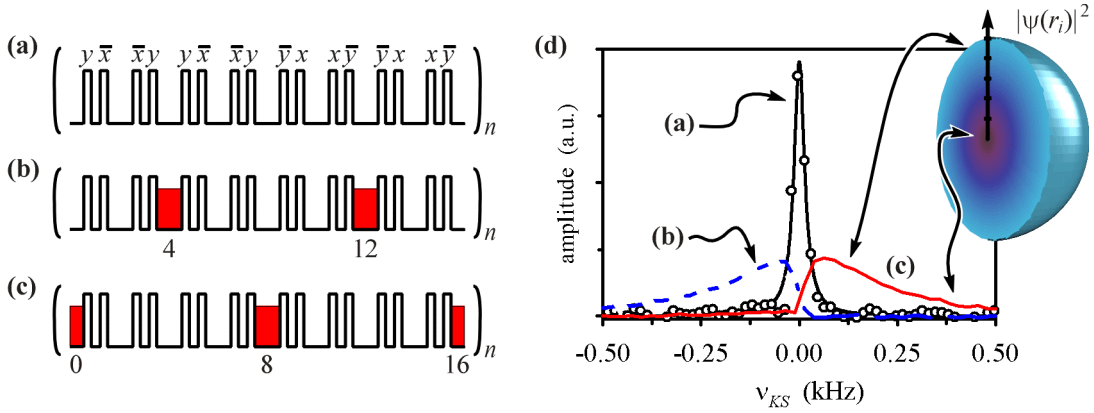

FIG. 4.3

(a) The CLSW-16 sequence of π/2 rf pulses applied to the signal nucleus during the NMR evolution period of the "light-off" experiment. The corresponding ^{71}Ga spectrum indicated in (d) was obtained using $t_p = 2.90$ μs and $t_{off} = 100$ ns, resulting in a frequency offset of 1186.6 Hz and yielding a Lorentzian line shape with a FWHM of 32.3 Hz.

(b) A "light-on" sequence, in which optical pulses (shaded) arrive in windows 4 and 12 of CLSW-16 to induce a Knight-shift interaction with photoexcited electrons.

(c) An alternative arrangement of optical pulses that reverses the shift relative to that obtained from (b).

(d) ^{71}Ga spectra corresponding to the sequences (a) – (c). The inset correlates the distribution of Knight shifts ν_{KS} in the spectrum corresponding to (c) with the positions of nuclear spins in the vicinity of a center of electronic localization. Large (small) shifts correspond to sites near to (distant from) $r = 0$, where electronic spin density given by $|\psi(r_i)|^2$ is at its maximum. Similar correlation can be made with the spectrum resulting from the sequence in (b). The convention in labeling the horizontal axis defines positive (negative) shifts as towards (away from) the Nyquist frequency in ω_1.

where the change in labeling from "*C*" for contact hyperfine to "*KS*" for Knight shift is in keeping with more standard usage in the solid-state NMR literature. To obtain the average Hamiltonian that corresponds to Eq. (4.14) and the sequences in Fig. 4.3(b) and (c), we apply the process described in Section C.1 of Chapter 1. Therein we substitute

$\tilde{\mathcal{H}}_{KS}^{i}$ for $\tilde{O}$ in Eq. (1.27) and evaluate the resulting expression using the toggling-frame transformations of $\tilde{\mathcal{H}}_{KS}^{i}$, which follow the trajectory of I_z that is given in Table A.1 of Appendix A. Inserting these transformations into Eq. (1.28), we obtain

$$\bar{\mathcal{H}}_{KS,i}^{(0)} = \pm \nu_{KS}(r_i)\, I_{z,i}, \tag{4.15}$$

where the sign is determined by the placement of optical pulses in the light-on sequence with ± corresponding to the light-on sequences of Figs. 4.3(b) and (c), respectively. The Knight shift,

$$\nu_{KS}(r_i) = -\tfrac{2}{3}\, b\, \Gamma\, \mu_0\, g_0\, \mu_B\, \gamma_n^i\, \langle \mathrm{S} \rangle\, \left|\Psi(\mathbf{r}_i)\right|^2, \tag{4.16}$$

is referenced to the center frequency of the light-off line shape. The averaging process scales ν_{KS} by the light-on duty factor

$$b = t_c^{-1} \sum\nolimits_j \left(\tau_j - t_p\right), \tag{4.17}$$

where the summation is over windows j of duration τ_j that include the optical perturbation. The appearance of the $\pi/2$ pulse duration in Eq. (4.17) accounts for the facts that rf pulses cover a finite duration of each window and that rf and optical excitation do not overlap, as shown in Fig. 2.6. For the pulse and cycle times noted above, and the τ_j's given in Table A.1 of Appendix A, Eq. (4.17) yields $b = 0.118\overline{3}$ for each of the noted light-on sequences.

The most important conclusion to be made based on the above experiments is that the Knight shift is due to the interaction of the lattice nuclei with a *localized* electronic state. This is demonstrated by the light-on spectra of Fig. 4.3(d), in each of which a *distribution* of Knight shifts is apparent that corresponds to a bound radial state. As

indicated in the figure inset, nuclei situated near to (far from) the center of localization exhibit the largest (smallest) shifts according to variations in electronic spin density at those sites [see Eq. (4.16)]. If the electronic state were instead delocalized (even if still radial), then lattice nuclei would experience a uniform time-averaged hyperfine interaction resulting in narrow-line, light-on spectra that are shifted from, but maintain the line shape of the light-off spectrum. The observed result confirms the expectation that the *d* line of the photoluminescence spectrum is due to recombination of trapped photocarriers.

Finally, we have shown that inhomogeneities in the beam or absorption profiles do not lead to spatial variation in photocarrier density, which would provide a corresponding *macroscopic* contribution to the spectral distribution. One might expect such a contribution to vary in shape with excitation power, while we have observed (see Section B.3) that only the amplitude, but not the shape, of the distribution scales over the range 1 - 20 W/cm^2. Furthermore, our observations of the short-timescale influence of spin diffusion (see Section C.1) on the spectral distribution and on signal relaxation times strongly evidence the *nanoscale* origin of the signal.[4(b)]

[4(b)] In Section C.1, we see that spin diffusion influences the ^{71}Ga NMR line shape in Knight-shift-imaging experiments at times on the order of $t = 2$ s, corresponding to a distance scale[97] of $(4Dt/\pi)^{1/2} \sim 10$ nm, i.e., the GaAs Bohr radius. This is calculated using an estimate of the ^{71}Ga spin-diffusion constant, $D(^{71}\mathrm{Ga}) = D(^{75}\mathrm{As}) \times \left(\gamma(^{71}\mathrm{Ga})/\gamma(^{75}\mathrm{As})\right)^4 \times \left(\chi(^{71}\mathrm{Ga})/\chi(^{75}\mathrm{As})\right) \sim 4\times10^{-13}$ cm^2/s, that is based on Paget's[7] measure of $D(^{75}\mathrm{As}) \sim 10^{-13}$ cm^2/s. The quartic dependence on gyromagnetic ratios γ derives from the quadratic dependence (see Abragam,[65] pp. 136-139) of the spin-diffusion rate on the homonuclear dipolar Hamiltonian $\left|\mathcal{H}_{II}^{D}\right|^2 \propto (\gamma_I)^4$, while the linear dependence on isotopic abundancies χ is justified by the fact (see Abragam,[65] p125) that the second moment of the NMR line shape, which is likewise quadratic in $\mathcal{H}_{II}^{D}$, scales with the occupancy of sites. As of this writing, there is no existing theory for explicit calculation of D for a spin-3/2 isotope.

The Knight-shift distribution in Fig. 4.3(d) reflects several factors. The first is qualitatively understood in terms of the number of contributing nuclei with a given shift. The relatively few nuclei near the center of localization provide the relatively low-amplitude, large-Knight-shift component of the signal. Quantitative assessment requires that one additionally accounts for the efficacy of both ONP and optical detection at each nuclear site. Also, the possibility that nuclear spin diffusion spreads order amongst distinct nuclei that overlap with the radial wave function must be evaluated. In Section C of the current chapter, I return to these quantitative issues with a detailed model for the light-on line shape.

A remaining point is a technical note on which of the two light-on sequences shown in Fig. 4.3(b) and (c) is preferred for measurement of the Knight-shift distribution. Each provides a Knight shift that is relative to the rf-induced homogeneous offset frequency. The arrangement of optical pulses in CLSW-16 that yields a shift towards the Nyquist frequency is favored over that which provides an oppositely directed shift towards zero frequency in the ω_1 dimension. This preference is intended to maintain the advantages of the second-averaging process (see Section C.1 of Chapter 1), which are diminished near $\omega_1 = 0$. A choice made between sequences (b) and (c) will depend on whether right (σ_+) or left (σ_-) circularly polarized optical excitation is used and on whether $\mathbf{B}_0$ is parallel or antiparallel to the optical propagation axis. These factors, as discussed in the next section, establish the sign of $\langle S \rangle$ in Eq. (4.16), and thus, together with the placement of optical pulses, determine the direction of the optical Knight shift.

2. Optical Reversal of the Knight Shift

The σ_+ optical excitation with propagation axis $\hat{n}_e$ parallel to $\mathbf{B}_0$ in the previous experiments yielded photoexcited electron spins with an average orientation antiparallel to $\mathbf{B}_0$. This fact is deduced from the selection rules governing circularly polarized excitation in GaAs (see Section B.1 of Chapter 1) and evidenced by the so-called banana effect, which was introduced in Section C.2.*i* of Chapter 2 and is described in detail elsewhere.[41,56-58] The noted selection rules dictate that the average spin orientation is reversed with σ_- excitation. The following experiments are designed to confirm that the observed optically induced shift is paramagnetic due to interaction with electron spins, as befits a shift attributed to the contact hyperfine interaction of Eqs. (4.1), (4.14) and (4.15) , and that the spin alignment is due to the initial photoexcitation. Diamagnetic changes in chemical shielding upon optical excitation are another conceivable mechanism to be evaluated.

The experiment timeline is shown in Fig. 4.4(a) and is similar to that used in field-cycling experiments (see Section E of Chapter 2) in that delays are incorporated after the ONP and NMR evolution periods. The latter break is sandwiched by $\pi/2$ store and read pulses. In sequence, these ~ 350 ms delays accommodate plus and then minus 90° rotation of the $\lambda/4$ plate that sits in the optical excitation pathway. Such rotation chooses between an excitation beam with σ_+ or σ_- polarization. In all cases, σ_+ excitation was used for ONP and optical detection, but, when implemented, the noted manipulations of the $\lambda/4$ plate selected σ_- polarization for the excitation during windows of the

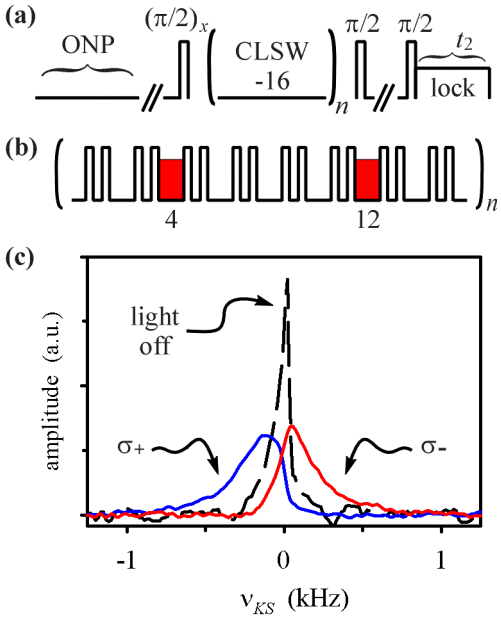

FIG. 4.4 **(a)** Timeline of the experiment designed to measure the dependence of the optically induced Knight shift ν_{KS} on circular polarization of the excitation beam. **(b)** The particular arrangement of optical pulses during CLSW-16 for light-on experiments. **(c)** Resulting spectra, where the CP that corresponds to each light-on result is indicated. The labeling convention on the horizontal axis matches that of Fig. 4.3(d).

CLSW-16 sequence that governed NMR evolution. At all times, $\mathbf{B}_0$ and $\hat{n}_e$ were roughly parallel.

Three experiments were performed using the timeline in (a), each with $t_p = 2.90$ s and $t_{off} = 150$ ns. The first incorporated the light-off CLSW-16 sequence to yield the indicated spectrum in Fig. 4.4(c), which references $\nu_{KS} = 0$ to 1.670 kHz in ω_1 and exhibits a 97 Hz Lorentzian FWHM. The accompanying experiments employed the light-on CLSW-16 sequence with optical excitation arranged as shown in part (b) of the figure. This placement corresponds to the negative coefficient of $\bar{\mathcal{H}}^{(0)}_{KS,i}$ in Eq. (4.15). As noted above, σ_+ excitation along $\mathbf{B}_0$ provides electron spins antiparallel to $\mathbf{B}_0$, and thus $\langle S \rangle < 0$. This yields $\nu_{KS} > 0$ in Eq. (4.16) since all other factors in that equation are positive. Inserting this positive ν_{KS} into the negative $\bar{\mathcal{H}}^{(0)}_{KS,i}$ provided by the light-on sequence yields a negative shift. This expectation matches the corresponding σ_+ spectrum indicated in Fig. 4.4(c). In contrast, σ_- excitation with the light-on sequence of (b) yields $\langle S \rangle > 0$ and a positive shift, matching the σ_- spectrum indicated in the figure.

Based on these results, we conclude that the observed shift behaves as expected for contact-hyperfine-mediated interaction between the photoexcited spins and lattice nuclei. The symmetry of the shifts with reversal of circular polarization rules out significant light-induced changes in chemical shielding. Furthermore, the shift direction is consistent with the observed photoluminescence polarization of only the *H*-band and bulk excitonic features, as alluded to in Section B.3.*ii* of Chapter 3. Therein, this point was used to argue that the band-to-acceptor carbon transition is excluded as a candidate ONMR signal carrier in our experiments, settling the notion that the *d* line is the relevant photoluminescent feature.

Finally, recall the point made in Section B.1 that positive Knight shifts are preferred. Since, as noted in Section C.2.*i* of Chapter 2, antiparallel electron-spin orientation is optimal for ONP and optical detection, all POWER NMR experiments for characterization of optical Knight shifts presented ahead were executed with σ_+ excitation along $\mathbf{B}_0$ to yield this condition. However, in each Knight-shift imaging experiment, the arrangement of optical pulses during CLSW-16 that is shown in Fig. 4.3(c) is used in order that signal intensity occur in the spectral range [say $(4\,t_c)^{-1} < \omega_1 > (2\,t_c)^{-1}$] where the line narrowing is most effective.

3. Optical Power Dependence of the Knight Shift

The dependence of the Knight shift on the time-averaged occupancy of the electronic localization site is expressed by the factor Γ in Eqs. (4.14) and (4.16). With goal of quantitative spectral modeling in mind, it is desirable to analyze Knight shift distribution data for which this Γ is a known parameter and, furthermore, equal to its

maximum, thus providing the highest possible resolution of spectrally distinct contributions to POWER NMR spectra. In the experiments of the present section, the measurement of the optical power dependence of the observed Knight shift distribution is presented. The resulting spectra determine the approximate power at which the interaction saturates, thus locating the desired maximum occupancy, $\Gamma = 1$.

A series of experiments was performed on a timeline identical to that used in the previous section and shown in Fig. 4.4(a). In the present case, delays of ~ 400 ms accommodated GPIB switching of the optical power output of the laser diode. The CLSW-16 sequence was implemented with $t_p = 2.90$ s and $t_{off} = 150$ ns, yielding a light-off spectrum that references $\nu_{KS} = 0$ to 1727.3 Hz in ω_1 and exhibits a 41.2 Hz Lorentzian FWHM. For all experiments here, the σ_+ excitation was at ~10.3 W/cm^2 during ONP and optical detection; however, the range 0.55 – 21 W/cm^2 was used for excitation during light-on POWER NMR experiments with the optical pulse arrangement of Fig. 4.3(b). The quoted optical power densities were calculated from the measured laser power output scaled by $(0.96)^6$ to account for reflections from the three quartz windows (six surfaces) of the optical cryostat, and using the measured 350 ± 50 μm diameter incident spot size. This dimension introduces a systematic uncertainty of ± 25 % in the power densities.

The results of the light-on experiments are shown in Fig. 4.5, where the enlarged view at right highlights the clear trend of increasing Knight shift with excitation power across the observed spectral distribution. The apparent saturation level is 10.3 W/cm^2, at which a slightly reduced shift is observed on the low-frequency (more positive) side relative to the next-highest power level at 21 W/cm^2, but where the observed distribution slightly exceeds that spectrum on the high-frequency (more negative) side, indicating that

the differences observed between these two results are near the limits of noise contributions. Thus it is reasonable to take $\Gamma = 1$ at 10.3 W/cm^2 for our sample.

In addition to these experiments, we have measured the optical power dependence of ONP and optical detection to reveal that the NMR signal strength also saturates near 10.3 W/cm^2 under the same experimental conditions. Thus, there is no advantage to operation at a higher power density, as such would only increase the optical shot noise in the experiment. Thus 10.3 W/cm^2 fluence was used during ONP, evolution and detection periods in all experiments presented subsequently for quantitative analysis.

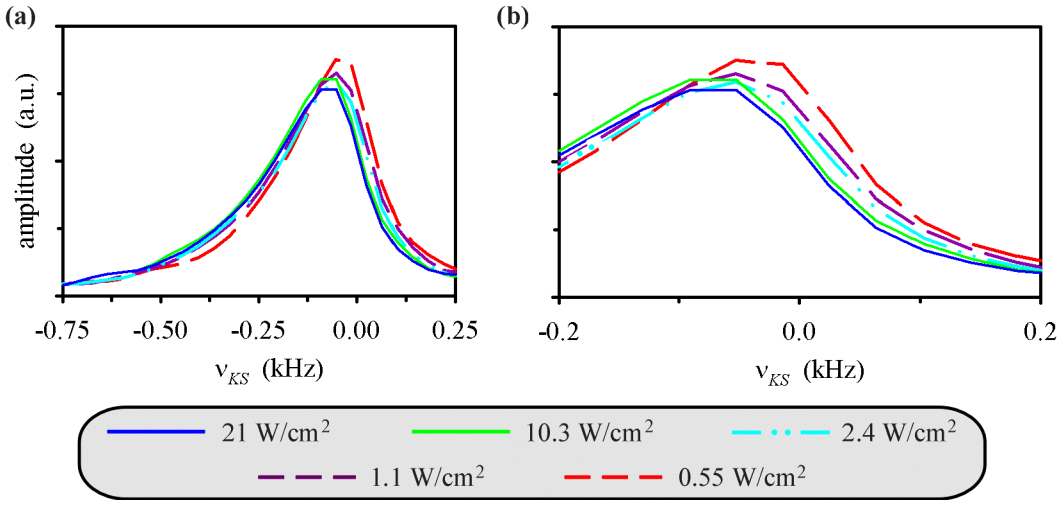

FIG. 4.5 **(a)** Dependence of the Knight shift ν_{KS} on incident optical power density. **(b)** Expanded view of the same spectra, highlighting the overall increase in the distribution of Knight shifts with laser power. The legend indicates the incident optical power density for excitation in selected windows of the CLWS-16 sequence.

C. Quantitative Spectral Modeling

Interpretation of the above Knight-shift distribution spectra as images of the electronic wave function requires that we consider the modes of nuclear spin relaxation during each of the three segments of the experiment timeline. This enables prediction of

the signal amplitudes that, together with the spectral distribution introduced by $|\Psi(\mathbf{r})|^2$ in Eqs. (4.15) and (4.16), provides an analytical expression for the NMR signal. During both ONP and optical detection, we must account for no fewer than three physical processes: quadrupolar relaxation, optically induced hyperfine relaxation and spin diffusion. An unanticipated process, rf-induced relaxation due to fluctuations in the phase of the spin-locking field during detection, is also considered. In contrast to the ONP and detection periods, an NMR evolution period t_1 that is governed by CLSW-16 includes a spin diffusion process that is attenuated to a negligible level, while quadrupolar and hyperfine relaxation are unimportant on the timescale of t_1. Thus, all relaxation during t_1 in a Knight-shift imaging experiment is accounted for empirically through observation of the linewidth of the accompanying light-off spectrum, a quantity that is taken to be independent of nuclear site.

Finally, as noted in the previous section, the optically detected NMR signal is due to nuclear spin interactions with a localized electronic state. Thus the starting point for spectral modeling in the present section incorporates the electronic state $\Psi_d(\mathbf{r})$ of Eqs. (4.4) - (4.7). This choice determines the spatial dependence of both ν_{KS} of Eq. (4.16) and the relaxation processes that govern ONP and optical detection.

The remainder of this section is organized as follows. In Section C.1, the influence of spin diffusion during the optical detection period is uncovered in an analysis of the full two-dimensional (ω_1 and t_2) data set obtained in Knight-shift imaging experiments of the type described above. This analysis determines the approximate time scale at which the role of spin diffusion becomes significant, while additionally extracting the time constant for non-optically induced signal relaxation during t_2. In

Section C.2, an analytical expression for Knight-shift distribution spectra is developed in terms of the single-spin (i.e., diffusion-free) relaxation problem. Measurements of the relevant time constants are presented for both ^{69}Ga and ^{71}Ga. Summation of the diffusion-free model over nuclear sites suffices for fitting spectra collected at short ONP times. Section C.3 presents the results of such experiments with t_{ONP} as short as 144 ms, while the simulations presented there complete characterization of the radial electronic state via the Knight-shift imaging experiment. Finally, in Section C.4, the one-to-one relationship between the Knight shift and the position of a nuclear site that is established in the shortest-ONP-time experiment provides a basis for following the effects of spin diffusion. A mathematical model is developed for conversion of the frequency domain spectrum into an empirical weighting function that, when longer ONP times are used, replaces the analytical expression developed in Section C.2.

1. Spatially Resolved Relaxation: the Effects of Spin Diffusion

The spin-diffusion process presents perhaps the greatest theoretical challenge towards gaining a sufficient understanding of the evolution of nuclear spin order during ONP and optical detection. Its effects are clearly evidenced with an alternative analysis of the data collected in a Knight-shift imaging experiment of the type described in Section B above. In the usual data work-up procedure, the signal transients in t_2 (the optical-detection period) are each integrated to yield a corresponding point in t_1. As a set, the t_1 points constitute the time-domain NMR signal. However, the integration over t_2 buries the effects of signal relaxation during that period; thus it is informative to bypass the integration and instead analyze the full 2D data set.

The first step in this alternative approach is Fourier transformation of the t_1 dimension, which yields a frequency-domain spectrum at *each* value of t_2. A plot of the resulting 2D data from a Knight-shift-imaging experiment is shown in Fig. 4.6. The second step is to characterize the frequency dependence of signal relaxation in t_2 by fitting slices cut through the data at constant Knight shift $\nu_{KS,\,i}$ to the form

$$S_2(t_2, \nu_{KS,\,i}) \;=\; A_2(\nu_{KS,\,i})\,\exp(-t_2 / T_{1\rho,\,i})\,, \tag{4.18}$$

where $A_2(\nu_{KS,\,i})$ is an arbitrary scale factor and $T_{1\rho,\,i}$ is the overall relaxation time constant for the spin-locked optically detected NMR signal corresponding to the i^{th} slice.

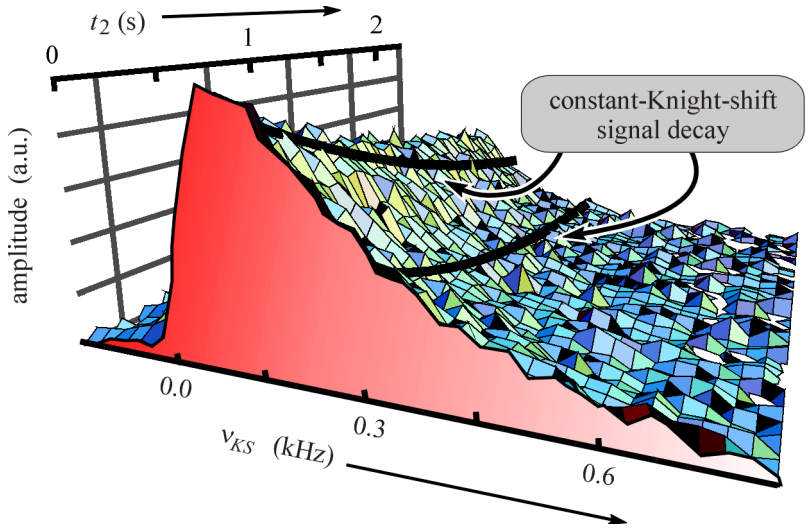

FIG. 4.6 ^{71}Ga Knight-shift distribution spectrum with additional dimension (t_2) of optical detection. The spectrum was collected using a timeline similar to that of Fig. 4.4(a), but without the delay periods and accompanying store and read $\pi/2$ pulses, while the relevant arrangement of σ_+ optical pulses during CLSW-16 is given in Fig. 4.6(c). The corresponding light-off spectrum with Lorentzian FWHM of 39.9 Hz references $\nu_{KS} = 0$ to 2124.3 Hz in ω_1. For both light-on and off experiments, $t_{\text{ONP}} = 4.992$ s, $t_p = 3.45$ μs and $t_{off} = 200$ ns.

Of interest now is the dependence of $T_{1\rho}$ on the observed Knight shift, which is uncovered by dissection of nuclear spin relaxation during optical detection. The first of two contributing processes, with time constant $T_{1\rho}^{B}$, accounts for spatially uniform, or background, nuclear spin relaxation, the dominant mechanism of which is phonon-driven quadrupolar relaxation. The second process is optically induced (hyperfine) relaxation, which, according to relaxation theory,[98,99] (see also Abragam,[65] pp309-11, 328-31) is characterized by the inverse time constant

$$\begin{aligned} \left(T_1^{opt}\right)^{-1} &= 2\,J^{(1)}(\omega_I - \omega_S) \\ &= \tfrac{2}{3}\,S(S+1)\,\frac{\tau_c}{1+(\omega_I-\omega_S)^2\tau_c^{\,2}}\left|2\pi\mathcal{H}_{hf}^{C}/\Gamma\right|^2, \end{aligned} \tag{4.19}$$

where $J^{(1)}(\omega_I - \omega_S)$ is the normalized spectral density of fluctuations with correlation time τ_c and at the difference between the electron and nuclear (angular) Larmor frequencies, ω_S and ω_I, occurring in the $(I_+S_- + I_-S_+)$ part of $\mathcal{H}_{hf}^{C}$.[4(c)] This factor is common to all nuclear sites and contains both repopulation dynamics of the optically relevant state and electron spin relaxation. According to Eqs. (4.1) and (4.16), the proportionality of $\left(T_1^{opt}\right)^{-1}$ to the square of $\left|\mathcal{H}_{hf}^{C}\right|$ may be rewritten in terms of

$$\left|\frac{\nu_{KS}}{b\langle S\rangle}\right| = \left|\mathcal{H}_{hf}^{C}\right|, \tag{4.20}$$

[4(c)] Abragam's[65] equation relating a relaxation time constant T_1 to a spectral density $J(\omega)$, expressed here in Eq. (4.19), pertains to a two-state fluctuation of the corresponding Hamiltonian. By factoring out Γ in our expression, we remain within the two-state context: that of a nuclear hyperfine interaction with an electron that is either spin up or down, but always present. This is appropriate to our experiments since $\Gamma = 1$. Paget[7] scaled his expression relating T_1^{opt} to $J^{(1)}(\omega)$ by Γ, which is an incorrect consideration of possible three-state dynamics for cases where $\Gamma \neq 1$.

where we recall that b is the light-on duty factor of the POWER NMR experiment. Inserting Eq. (4.20) and $S = \frac{1}{2}$ into Eq. (4.19) yields

$$\left(T_1^{opt}(\nu_{KS})\right)^{-1} = \left(\frac{2\pi^2}{b^2\langle S\rangle^2}\,\frac{\tau_c}{1+(\omega_I-\omega_S)^2\tau_c^{\,2}}\right)\nu_{KS}^{\,2}. \tag{4.21}$$

Finally, the inverse of the measured time constant, *without accounting for the influence of spin diffusion*, is

$$\left(T_{1\rho}(\nu_{KS})\right)^{-1} = \left(T_1^{opt}(\nu_{KS})\right)^{-1} + \left(T_{1\rho}^{B}\right)^{-1}, \tag{4.22}$$

and exhibits quadratic dependence on ν_{KS} given by Eq. (4.21).

Consider, however, the opposite extreme, where spin diffusion is fast compared to the noted relaxation processes and thus cannot be ignored. Here, the signal with a given Knight shift due to its association with nuclear spin evolution at a single lattice site during t_1 freely diffuses during t_2.[4(d)] Thus, the spin order associated with a single site is detected as that order migrates across the set of lattice sites corresponding to the full distribution of Knight shifts and relaxation times $T_{1\rho}(\nu_{KS})$. In this case, all signal contributions reflect a *spatially averaged* hyperfine relaxation process during t_2 that is characterized by a *uniform* time constant, i.e., one that is independent of ν_{KS}.

In Fig. 4.7(a), the $(T_{1\rho})^{-1}$ values obtained from the ^{71}Ga data in Fig. 4.6 are plotted vs the square of corresponding Knight shifts. The fast-diffusion, uniform-relaxation limit and the negligible-diffusion extreme of Eqs. (4.21) and (4.22) are also depicted. The observed behavior is intermediate between these extremes. At the low-Knight-shift side

[4(d)] Recall that, as noted in the opening remarks of Section C, spin diffusion is ineffectual during a t_1 period governed by the CLSW-16 time-suspension pulse sequence.

of the plot, the measured $T_{1\rho,i}$ follow the diffusion-free limit, while fast diffusion is approached at higher Knight shifts. This apparent increase in the influence of spin diffusion with ν_{KS} is understood as follows. According to Eqs. (4.16), (4.21) and (4.22), ν_{KS} and $|\frac{\partial}{\partial r} T_{1\rho}^{-1}|$ have quadratic and quartic dependence, respectively, on the radial, exponentially decaying $|\psi(r_i)|$. Thus the maximum of each quantity occurs at $r = 0$, the center of electronic localization. When spin order diffuses over nuclear sites in a given distance range, the corresponding range of sampled time constants $T_{1\rho}(\nu_{KS})$ is much larger in the vicinity of these maxima than it is for spin order that diffuses on the same distance scale, but far from $r = 0$. Thus, at a given diffusion rate, the apparent effect, as witnessed by our measured $T_{1\rho}$ values, is greatest in the large-Knight-shift regime near the center of localization and vanishes at small Knight shifts.

We can conclude from this analysis that spin diffusion does make a significant contribution to the dynamics on time scales of order 2 s, which is the duration of t_2 corresponding to the data analyzed above. Furthermore, the linear fit to measured $T_{1\rho}$ values for small Knight shifts ($\Delta\nu_{KS} \lesssim 200$ Hz) in Fig. 4.7 intercepts the abscissa to yield $T_{1\rho}^{B}(^{71}\mathrm{Ga}) = 4.8 \pm 0.4$ s, while a similar experiment and analysis yielded $T_{1\rho}^{B}(^{69}\mathrm{Ga}) = 2.9 \pm 0.1$ s. We note, incidentally, that for background relaxation due solely to homogeneous fluctuations in the quadrupolar interaction, one expects that $T_{1\rho} \sim T_1$, while the above analysis shows that $T_{1\rho} << (T_1 \sim \text{hours})$. Furthermore, such relaxation would yield

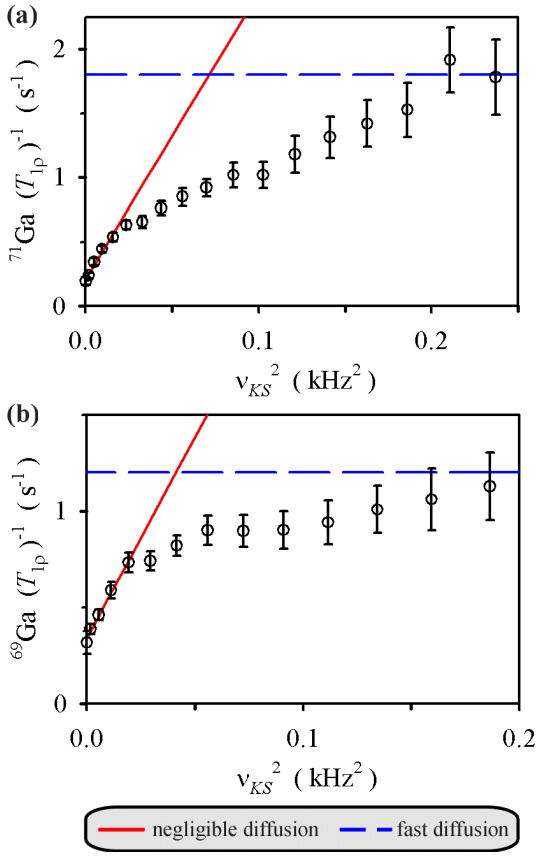

FIG. 4.7 Frequency dependence of NMR signal relaxation during t_2 for **(a)** ^{71}Ga and **(b)** ^{69}Ga. Data points with error bars at 95% confidence result from fits of constant-Knight-shift slices of the data in Fig. 4.6 to Eq. (4.18). Lines correspond to the hypothetical cases of negligible and fast nuclear spin diffusion. Qualitative comparison of (a) and (b) indicates that spin diffusion may be more efficient for ^{69}Ga, possibly due to its higher isotopic abundance (69.4%), although the dipolar interaction responsible for spin diffusion is stronger for ^{71}Ga.

$$\frac{\left(T_{1\rho}^{B}(^{71}\mathrm{Ga})\right)^{-1}}{\left(T_{1\rho}^{B}(^{69}\mathrm{Ga})\right)^{-1}} = \frac{\left(Q(^{71}\mathrm{Ga})\right)^{2}}{\left(Q(^{69}\mathrm{Ga})\right)^{2}} \sim 0.4\,, \tag{4.23}$$

whereas, insertion of the measured time constants into the left-hand side of Eq. (4.23), yields (0.61 ± 0.06). These observations suggest that rf-induced relaxation stemming from phase noise in the digitally synthesized rf is dominant during t_2 in our experiments. In fact, we have observed dramatic dependence of signal relaxation during t_2 on the clock source used in the digital rf synthesis.

Finally, we note that the starting point in the above analysis, Eq. (4.19), is rigorously valid only for the dynamics of a spin-$\frac{1}{2}$ nucleus. This ignores the possibility that distinct time constants may govern relaxation between the pairs of states of a spin-$\frac{3}{2}$ nucleus, $|m\rangle = |\pm\tfrac{3}{2}\rangle, |\pm\tfrac{1}{2}\rangle$ and $|m\rangle = |+\tfrac{1}{2}\rangle, |-\tfrac{1}{2}\rangle$, that are separated by $\Delta m = \pm 1$. Lambert and Weitekamp[100] have completed a preliminary investigation of this issue. However, above and in the following section, the assumption that the spin-$\frac{1}{2}$ expression is taken to be sufficient, as inclusion the noted spin-$\frac{3}{2}$ dynamics is beyond the scope of this thesis.

2. Characterization of the Diffusion-Free Signal Dynamics

On time scales much less than the two-second period analyzed above, it proves sufficient to model relaxation during ONP and optical detection in the *absence* of spin diffusion. To that end, I focus on short (fraction of a second) ONP time experiments in remaining Knight-shift imaging experiments for characterization of the localized electronic state. However, before presentation and analysis of such experiments, it is necessary to formalize the diffusion-free relaxation problem and to present measurements of the time constants T_1^{opt} and T_{1Q} that characterize optically induced and quadrupolar relaxation, respectively, during the ONP period.

i. The Diffusion-Free Optically Pumped and Detected NMR Signal

The relaxation process that yields the optically induced nuclear polarization $P(t_{ONP}, r)$ is described by the differential expression

$$\frac{d}{dt_{ONP}} P(t_{ONP}, r) = \frac{P_0^{opt} - P(t_{ONP}, r)}{T_1^{opt}(r)} + \frac{P_0^{T} - P(t_{ONP}, r)}{T_{1Q}} \tag{4.24}$$

where P_0^{opt} and P_0^{T} are the limits of optically induced and thermal nuclear spin relaxation. The radial dependence of Eq. (4.24) derives from hyperfine relaxation, which, according to Eqs. (4.4), (4.6), (4.16) and (4.21), is characterized by the time constant

$$\begin{aligned} T_1^{opt}(r) &= \left(\frac{2\pi^2}{b^2 \langle S \rangle^2} \frac{\tau_c}{1 + (\omega_I - \omega_S)^2 \tau_c^2} \right)^{-1} C^{-2} \left| \psi(r) \right|^{-4} \\ &= T_1^{opt}(0)\, e^{+4r/a_d}, \end{aligned} \tag{4.25}$$

where C is a constant of the hyperfine interaction, and where, in expressing the rightmost equivalence, the radial envelope of a donor-bound electron is assumed. Solving Eq. (4.24) for the initial condition $P(0, r) = 0$ and inserting Eq. (4.25) into the result finally yields

$$\begin{aligned} P(t_{ONP}, r) = {} & \frac{P_0^{opt}\, T_{1Q} - P_0^{T}\, T_1^{opt}(0)\, e^{+4r/a_d}}{T_{1Q} + T_1^{opt}(0)\, e^{+4r/a_d}} \\ & \times \left[1 - \exp\left(\frac{-t_{ONP} \left(T_{1Q} + T_1^{opt}(0)\, e^{+4r/a_d} \right)}{T_{1Q}\, T_1^{opt}(0)\, e^{+4r/a_d}} \right) \right]. \end{aligned} \tag{4.26}$$

The relevance of the chosen initial condition to experiment is guaranteed by the sequence of kill pulses leading the ONMR timeline.

The optically detected signal $S_2(t_2, r)$ is described by the differential equation

$$\frac{d}{dt_2} S_2(t_2, r) = \left(\left(T_1^{\,opt}(r) \right)^{-1} + \left(T_{1\rho}^{B} \right)^{-1} \right) S_2(t_2, r) . \tag{4.27}$$

Inserting Eq. (4.25) for $T_1^{\,opt}(r)$ into the solution to this expression yields

$$S_2(t_2, r) = S_2(0, r) \exp\left(\frac{-t_2 \left(T_{1\rho}^{B} + T_1^{opt}(0)\, e^{+4r/a_d} \right)}{T_{1\rho}^{B}\; T_1^{opt}(0)\, e^{+4r/a_d}} \right). \tag{4.28}$$

The relevant form of the initial condition $S_2(0, r)$ is determined by nuclear spin evolution during ONP and t_1, and by the position-dependent efficiency of Hanle-effect optical detection. The latter is set by the strength of the hyperfine interaction, which, according to Eqs. (4.1), (4.4), and (4.6), is radially dependent, as expressed in full by the exponential decay e^{-2r/a_d} of $|\psi(r)|^2$. Thus, we have

$$S_2(0, r) = A_0\, P(t_{ONP}, r) \left[e^{-\pi \Delta\nu(r)\, t_1} \cos\left(\omega(r)\, t_1 \right) \right] e^{-2r/a_d} , \tag{4.29}$$

where A_0 is an overall scale factor, and $\omega(r)$ and $\Delta\nu(r)$ are the experiment-dependent frequency and Lorentzian FWHM of the signal in ω_1.

ii. The Time-Constants for Optically Induced and Quadrupolar Relaxation

Evaluation of the contributions of $T_1^{\,opt}(0)$ and T_{1Q} to optical polarization in the diffusion-free formalism, requires measurement of the optically detected NMR signals of ^{71}Ga and ^{69}Ga vs t_{ONP} and t_2 at $t_1 = 0$. Constant 5.040 s reference (^{75}As) and miscellaneous (non-signal Ga isotope) nuclei ONP times were used in

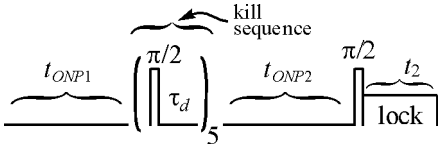

FIG. 4.8 Timeline of rf excitation of the signal-nucleus for characterization of its ONMR signal dynamics. Saturation of signal nucleus magnetization by the kill sequence restarts the clock on its polarization time, yielding $t_{ONP}^{sig} = t_{ONP2}$. The reference and miscellaneous nuclei, which are unaffected by the kill sequence, receive $t_{ONP}^{ref,misc} = (t_{ONP1} + t_{ONP2})$, while the dephasing time, $\tau_d = 1.5$ ms, is negligible in comparison to the ONP periods. A similar arrangement with kill pulses on the reference and miscellaneous nuclei is used to yield $t_{ONP}^{sig} > t_{ONP}^{ref,misc}$.

these experiments. Isotope-specific ONP times were set by inserting kill sequences at appropriate points along the ONP segment of the experiment timeline as shown in Fig. 4.8. The combination of Eqs. (4.26), (4.28) and (4.29) provides the expression for the resulting radially dependent signal:

$$S_2(t_{ONP}, t_2, r) = A_0\, e^{-2r/a_d}\, \frac{P_0^{opt}\, e^{-4r/a_d} - P_0^T \left(T_1^{opt}(0)/T_{1Q}\right)}{e^{-4r/a_d} + \left(T_1^{opt}(0)/T_{1Q}\right)} \times \left[1 - \exp\left(\frac{-t_{ONP}}{T_1^{opt}(0)}\left(e^{-4r/a_d} + \left(T_1^{opt}(0)/T_{1Q}\right)\right)\right)\right] \times \exp\left(\frac{-t_2}{T_1^{opt}(0)}\left(e^{-4r/a_d} + \left(T_1^{opt}(0)/T_{1\rho}^{B}\right)\right)\right). \tag{4.30}$$

It is furthermore reasonable to assume that

$$P_0^{opt}\, e^{-4r/a_d} \gg P_0^T \left(T_1^{opt}(0)/T_{1Q}\right) \tag{4.31}$$

over the range of r in which nuclei make a nonvanishing contribution to the signal. This is evident as P_0^{opt} is on the order of the average photoexcited electron spin polarization,

$$P_e = 2\langle S\rangle \sim 10^3 P_0^T, \tag{4.32}$$

in our experiments, and since we expect that $T_1^{opt}(0)$ is on the order of ms[7] while T_{1Q} is on the order of hours in GaAs at 2 K. Thus, Eq. (4.30) reduces to

$$S_2(t_{ONP}, t_2, r) \sim A_0\, e^{-2r/a_d}\, \frac{e^{-4r/a_d}}{e^{-4r/a_d} + \left(T_1^{opt}(0)/T_{1Q}\right)} \times \left[1 - \exp\left(\frac{-t_{ONP}}{T_1^{opt}(0)}\left(e^{-4r/a_d} + \left(T_1^{opt}(0)/T_{1Q}\right)\right)\right)\right] \times \exp\left(\frac{-t_2}{T_1^{opt}(0)}\left(e^{-4r/a_d} + \left(T_1^{opt}(0)/T_{1\rho}^{B}\right)\right)\right), \tag{4.33}$$

where P_0^{opt} has been absorbed into the overall scale factor A_0.

The 2D data was collected over the variable ranges $t_{ONP} = 0$ to 30 s and $t_2 = 0$ to 2.25 s under the standard conditions for ONMR: most notably, $B_0 \sim 226$ mT and along both [001] and $\hat{n}_e$, with σ_+ excitation thus yielding electron spins antiparallel to $\mathbf{B}_0$. The results were fit to the integral expression

$$S(t_{ONP}, t_2) = A_1 + A_0 \int_0^{r_{max}} r^2 \, S_2(t_{ONP}, t_2, r) \, dr \,, \tag{4.34}$$

where the overall offset parameter A_1 is necessitated by the dc character of the signal in the spectrometer's audio stage. In order to include all nuclear sites that make an appreciable contribution to the optically detected NMR signal, the cutoff $r_{max} = 70$ nm sufficed in the numerical evaluation of the integral. Implicit in Eq. (4.34) is the approximation that the lattice includes a continuous distribution of nuclei. This approximation was found to be satisfactory by comparison with direct summation in other calculations.

A standard nonlinear least-squares routine was used to execute a four-parameter (A_0 and A_1, $T_1^{opt}(0)$ and T_{1Q}) fit to each of the ^{71}Ga and the ^{69}Ga data sets using the measured values of $T_{1\rho}^B$ reported in Section C.1. Again, it is important to distill the data set in such a way that the time constants resulting from the fit to Eq. (4.34) are relatively free of the effects of spin diffusion. This was achieved by focusing the analysis on the data at short-timescales as follows. The data set corresponding to the full range of contributing t_{ONP} and t_2 values for a given isotope was fit to yield a set of best-fit parameters, which in turn were used as the starting point for fitting a truncated version of the same data set. For example, data up to only a reduced maximum value of t_{ONP} was included in optimizing the second fit. This regression process, and a complementary one

in t_2, was applied repetitively, each time using the results of the fit as starting parameters for the subsequent smaller (i.e., shorter-time) data set.

The results of this regression analysis are plotted in Fig. 4.9 for both ^{71}Ga and ^{69}Ga. For each isotope, the smallest truncated data sets yielded a rough plateau of $T_1^{opt}(0)$ in the plane of maximum t_{ONP} and t_2 values (t_{ONP}^{max} and t_2^{max}) included in the fits. Meanwhile, T_{1Q} diverged at all points on the grid corresponding to $t_2^{max} \lesssim 6$ s, indicating that the corresponding relaxation rate is negligible in comparison with that of the optically induced effect for the nuclei contributing to the signal at short ONP times. The time constants for optically induced relaxation are estimated from the average of the fit results at shorter times, i.e., those where $t_{ONP}^{max} = 0.696 - 1.896$ s and $t_2^{max} = 0.4 - 1.0$ s, respectively. This yields $T_1^{opt}(0) \sim 16$ ms and 90 ms for ^{71}Ga and ^{69}Ga, with standard deviations of 9% and 12%, respectively, in the sets contributing to these average values. These results correspond to $T_1^{opt}(a_d) = 0.87$ and 4.9 s, for ^{71}Ga and ^{69}Ga. In a more indirect estimate pertaining to a similar radial electronic system, Paget[7] reported $T_1^{opt}(0) \sim (80 \pm 50)$ ms for ^{75}As, which, appropriately scaled by the $(\gamma_{75As}\, d_{75As} / \gamma_\alpha\, d_\alpha)^2$, yields similar values to those reported above: $T_1^{opt}(0) \sim (72 \pm 45)$ and (120 ± 72) ms for $\alpha =$ ^{71}Ga and ^{69}Ga. Others have reported much longer time constants;[13,101] however, their measurements likely reflect either optical pumping of bulk nuclei via delocalized states or spin diffusion into the bulk from spins near confined electronic states.

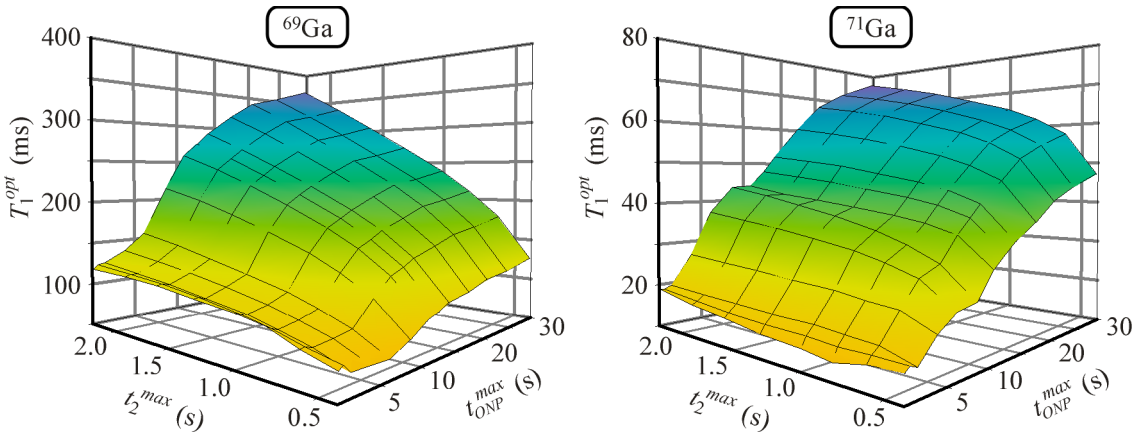

FIG. 4.9 Plots of T_1^{opt}, the time constant for optically induced relaxation, as extracted from fits of Eq. (4.34) to ^{69}Ga and ^{71}Ga optically detected NMR signals as functions of t_{ONP} and t_2. Each data point in the above surfaces results from a particular fit in which the data set was truncated at t_{ONP}^{max} and t_2^{max} in the two time dimensions. The grid is composed of the cross between the sets $t_{ONP}^{max} = \{0.4, 0.6, 0.8, 1.0, 1.3, 1.6, 1.9, 2.25\}$ and $t_2^{max} = \{0.696, 1.176, 1.896, 3.960, 6.120, 8.640, 10.872, 12.600, 14.112, 17.352, 20.592, 24.480, 29.664\}$, where all values are given in seconds.

3. Quantitative Knight-Shift Imaging

With the time constants governing nuclear spin relaxation during ONP and optical detection in hand, I now present the results of Knight-shift-imaging experiments performed as a function of ONP time on the NMR signal nucleus. The shortest-ONP-time results are quantitatively fit according to the diffusion-free signal dynamics governed by the measured time constants $T_1^{opt}(0)$ and $T_{1\rho}^{B}$, and the observation that the relaxation rate corresponding to T_{1Q} is vanishing on the time scale of these processes. The relevant expression for the single-nucleus, optically pumped and detected NMR signal is obtained by inserting Eqs. (4.26) and (4.29) into Eq. (4.28), accounting for the inequality of Eq. (4.31), and setting $\left(T_1^{opt}(0)/T_{1Q}\right) = 0$, to finally yield

$$S_2(t_{ONP}, t_1, t_2, r_i) = A_0 \left[e^{-\pi \Delta\nu(r_i)\, t_1} \cos\left(\omega(r_i)\, t_1\right)\right] \times \left[1 - \exp\left(\frac{-t_{ONP}}{T_1^{opt}(0)\, e^{+4r_i/a_d}}\right)\right] e^{-t_2/T_{1\rho}(r_i)}\, e^{-2r/a_d}, \tag{4.35}$$

which incorporates the expression

$$T_{1\rho}(r_i) = \left(\left(T_{1\rho}^{B}\right)^{-1} + \left(T_1^{opt}(0)\, e^{+4r/a_d}\right)^{-1}\right)^{-1}. \tag{4.36}$$

In Knight-shift-imaging experiments, the evolution frequency,

$$\omega(r_i) = 2\pi\, (\, \nu_{KS}(r_i) + \nu_{off}\,), \tag{4.37}$$

at the i^{th} nuclear site is determined by Eq. (4.16) for $\nu_{KS}(r_i)$ and ν_{off}, the rf-induced homogeneous offset frequency corresponding to Eq. (1.35). Furthermore, the FWHM $\Delta\nu(r_i)$ of single-site contributions is taken to be spatially uniform and equal to that of the Lorentzian fit to the spectrum obtained in an accompanying light-off experiment.

i. Short-ONP-Time Knight-Shift Images

The results were obtained using the standard timeline for pointwise time-domain evolution in t_1 with LBD in t_2. Light-on experiments incorporated the POWER NMR sequence of Fig. 4.3(c) with σ_+ excitation at ~10 W/cm^2, and $\hat{n}_e$ parallel to $\mathbf{B}_0$, thus providing electron spins antiparallel to $\mathbf{B}_0$ // [001]. Using t_c = 120 μs, t_p = 3.45 μs and t_{off} = 200 ns, provided, according to Eq. (4.17), the light-on duty factor $b = 0.1091\overline{6}$.

A series of ^{71}Ga spectra with varying ONP times were collected back-to-back during a continuous experimental run of 180 minutes plus tune-up time. For the signal nucleus, t_{ONP} = 0.144, 0.240, 0.720 and 3.000 s in this series of light-on experiments, while t_{ONP} = 3.000 s was incorporated in the lone light-off experiment. Each of these incorporated miscellaneous (^{69}Ga) and reference (^{75}As) nucleus ONP times of 4.992 s,

with isotope-specific ONP times set as described in Section C.2. Time-domain spectra in t_1 were obtained by integrating the signal transients in t_2 from $t_2^{min} = 0.100$ s to the end of the optical detection period at $t_2^{max} = 2.280$ s. These limits reflect the exclusion of data from $t_2 < t_2^{min}$, a period that is skewed by ringing of the spectrometer filters, and a detection period that is halted before the signal decay is complete. The latter limit is intended to reduce the contribution of resistive heating in the rf coils to the *l*-He boil-off rate during spin-locked detection. Furthermore, keeping this limit short is additionally important since problematic spin diffusion gains prominence at larger values of t_2^{max}.

The resulting spectra are shown in Fig. 4.10. The best fit to the light-off spectrum is a 32.3 Hz FWHM Lorentzian that references ν_{KS} to 2119.5 Hz in ω_1. Each of the light-on spectra exhibits the qualitative features (see Section B.1) of a Knight-shift distribution due to interaction with a radial electronic state. Quantitative analysis of the frequency dependent increases in signal amplitude with t_{ONP} requires comparison with the analytical model for diffusion-free dynamics.

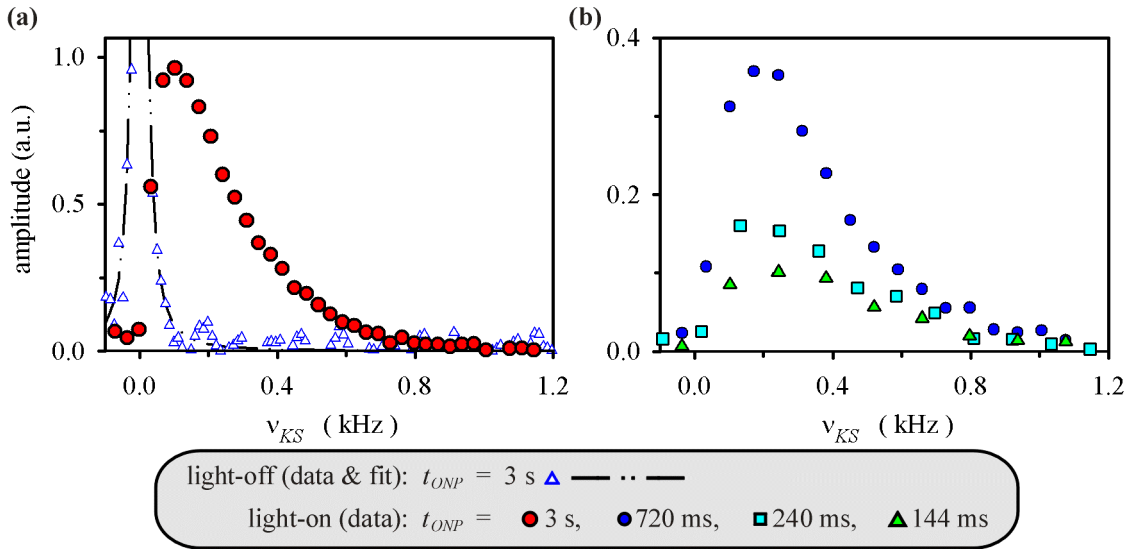

FIG. 4.10 ^{71}Ga Knight-shift-distribution spectra as a function of t_{ONP}. **(a)** Light-on and (truncated) light-off spectra collected at $t_{ONP} = 3.000$ s. **(b)** Light-on spectra collected at the indicated short ONP times where the influence of spin diffusion is diminished.

ii. Simulation and Fitting Procedure

The time-domain spectra that were Fourier transformed to yield the above Knight-shift distributions were simulated and fit using the analytical signal expression,

$$S(t_{ONP}, t_1) = \sum_i \left(\int_{t_{2min}}^{t_{2max}} S_2(t_{ONP}, t_1, t_2, r_i)\, dt_2 \right), \tag{4.38}$$

where the summation is over Ga sites in one radially bounded octant of the lattice about the center of electronic localization. Inserting Eq. (4.35) into this expression we obtain

$$S(t_{ONP}, t_1, r_i) = \sum_i A(t_{ONP}, r_i) \left[e^{-\pi \Delta\nu_i t_1} \cos\left(\omega(r_i) t_1\right) \right], \tag{4.39}$$

where the single-site amplitude is given by

$$\begin{aligned} A(t_{ONP}, r_i) = A_0 & \left[1 - \exp\left(\frac{-t_{ONP}}{T_1^{opt}(0)\, e^{+4r_i/a_d}} \right) \right] \\ & \times \left(e^{-t_2^{min}/T_{1\rho}(r_i)} - e^{-t_2^{max}/T_{1\rho}(r_i)} \right) T_{1\rho}(r_i)\, e^{-2r_i/a_d}. \end{aligned} \tag{4.40}$$

and Eq. (4.36) for $T_{1\rho}(r_i)$.

The octant of lattice sites over which Eq. (4.39) is summed was obtained as follows. Figure 4.11 depicts the zincblende crystal structure of the GaAs lattice, which is formed by the two interpenetrating fcc sublattices of Ga and As. Four of the Ga sites are highlighted in the figure along with their coordinates in units of $\frac{a}{2}$, where a is the GaAs lattice parameter.

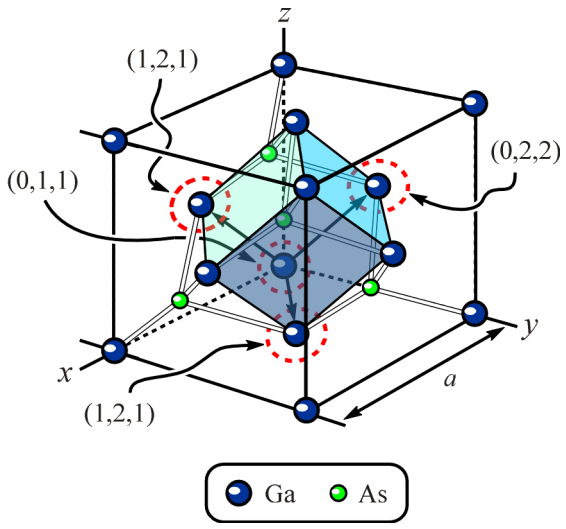

FIG. 4.11 The zincblende crystal structure of GaAs. The coordinates of the four Ga "seed" sites discussed in the text are indicated in units of ½ the lattice parameter a. The center of electronic localization defined to be at (0, 0, 0).

Incrementation of the x, y, or z index of one of these "seed" positions by +2 locates another Ga site. Repetition of such incrementation at each index of each seed generates the complete Ga sublattice in the octant of interest. For the purpose of the present calculation, it is sufficient to include only those sites within a 70 nm radial boundary, outside of which the contribution to the optically detected NMR signal is negligible.

In calculating the time-domain signal with Eq. (4.40), we incorporate the position-dependent frequency of Eqs. (4.16) and (4.37), using the donor-bound radial electronic state of Eqs. (4.4) – (4.7). Relevant experimental parameters and measured constants that were presented in previous sections are compiled in Table 4.2. Therein, the values corresponding to both ^{69}Ga and ^{71}Ga are listed; however, only the ^{71}Ga values are necessary for simulation of the spectra shown in Fig. 4.10.

Table 4.2 Constants and parameters relevant to simulation of Knight-shift distribution spectra.

Constant or Parameter	Units	^{71}Ga	^{69}Ga	Source
$T_1^{opt}(0)$	ms	16	90	Section C.2
$T_{1\rho}^{B}$	s	4.8	2.9	Section C.1
a_d	nm	10.37	same	Eq. (4.7)
a	nm	0.565	same	Kittel[79]
Ω	10^{-29} m^3	4.51	same	Eq. (4.5)
d_i	10^{31} m^{-3}	5.8	same	Paget, *et al.*[6]
γ_n	MHz / T	12.98	10.22	——
Γ	none	1	same	Section B.3
b	none	$0.1091\overline{6}$	same	[(a)]Section C.3.*i*
ν_{off}	kHz	2.119_5	——	[(b)]Section C.3.*i*
$\Delta\nu$	Hz	32.3	——	[(b)]Section C.3.*i*

[(a)] Parameters of the CLSW-16 sequence determine b.
[(b)] The Lorentzian fit to the light-off line shape determines ν_{off} and $\Delta\nu$.

Two free parameters remain: the overall scale factor A_0 and the average electronic spin $\langle S \rangle$. A grid search over these was executed for each of the ONP times used in obtaining the light-on spectra above. The optimum values were located according to a minimization of the χ^2 value obtained by comparison of the $t_{ONP} = 144$ ms time-domain data and simulation. Of the light-on spectra presented in Fig. 4.10, this is the least perturbed by spin diffusion, and thus offers the best comparison with the analytical model for the NMR signal. Contours of the grid search are shown in Fig. 4.12, while its detailed description is contained in the caption. The minimum of $\chi^2(t_{ONP} = 144 \text{ ms})$ is 1.0 and located at $\langle S \rangle = 0.15$ and $A_0 = 0.86$, where the latter quantity is the unitless ratio of the $t_1 = 0$ point of the simulation to that from the experimental data. Remarkably, this value of $\langle S \rangle$ is identical within experimental accuracy to those of the *e* and *d* lines of the

H-band, which were obtained in independent PL experiments and reported in Table 3.2. The minimum χ^2 values and corresponding parameters at each ONP time are given in Table 4.3. As noted therein, and as apparent from the contour plots of the grid search, the t_{ONP} = 144 ms minimum almost directly overlaps those of the t_{ONP} = 240 and 720 ms data. This indicates that the influence of spin diffusion remains small at these time scales. However, the minimum for the t_{ONP} = 3 s data is located more distantly in the parameter space and yields the worst χ^2 value in the group, which is presumably attributable to the failure of the diffusion-free modeling of signal amplitudes in Eq. (4.40).

Table 4.3 The χ^2 minima resulting from grid search over $\langle S \rangle$ and A_0. The values $\langle S \rangle_{min}$ and $(A_0)_{min}$ locate the minimum at each value of t_{ONP}. The last column provides the χ^2 value for simulations at each ONP time using the parameters in the shaded (t_{ONP} = 144 ms) row. The last decimal place in each fit result is shown as a subscript and, while not significant for measurement, give a sense of the variation from fit to fit.

t_{ONP} (ms)	best χ^2	$\langle S \rangle_{min}$	$(A_0)_{min}$	χ^2 at t_{ONP} = 144 ms minimum
144	1.0_0	0.15_3	0.78_0	1.0_0
240	1.2_6	0.15_0	0.77_6	1.2_6
720	1.5_9	0.14_8	0.83_0	1.8_2
3000[(a)]	4.3_1	0.12_2	0.86_0	12.4_9

[(a)] The χ^2 minimum for the t_{ONP} = 3 s data was located in the coarse grid search.

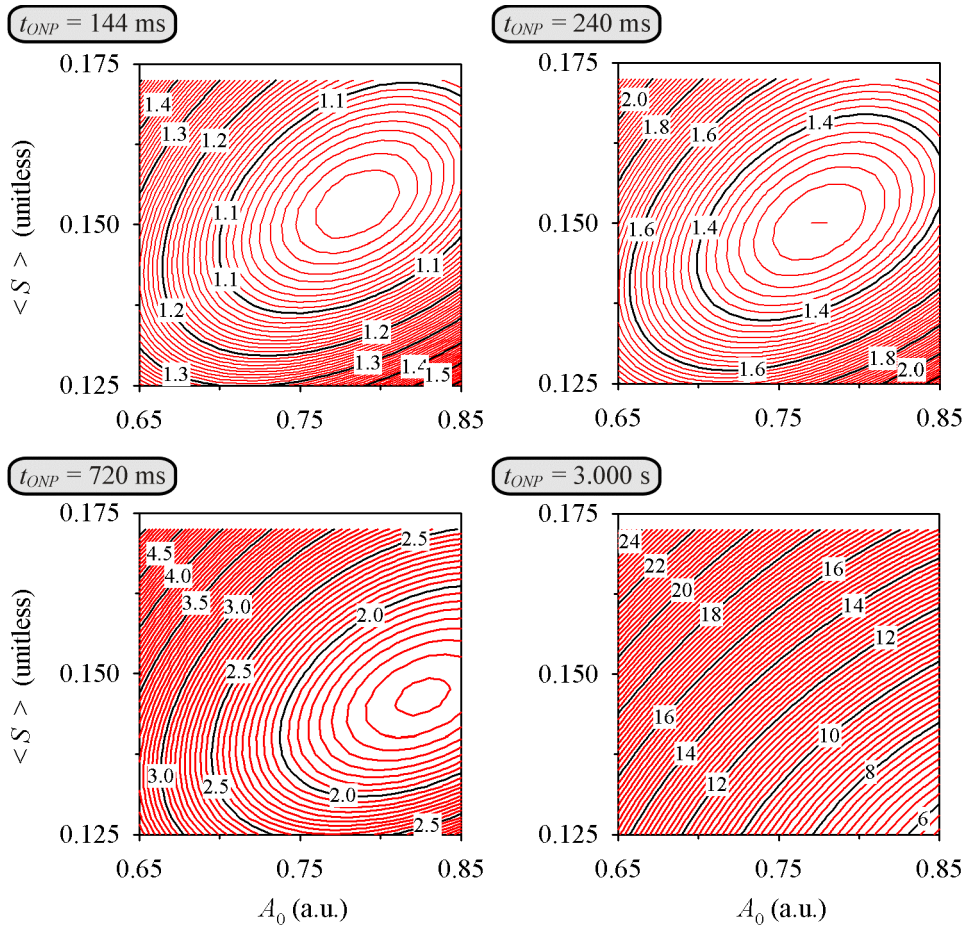

FIG. 4.12 Contour plots of the χ^2 values obtained by comparison of the time-domain spectra that correspond to the light-on results in Fig. 4.10 with simulated spectra obtained from the analytical model discussed in the text. Coarse and fine 2D grids were used in the search over the parameters $\langle S \rangle$ and A_0, covering the ranges: (1) coarse: $\langle S \rangle = \{0.05 - 0.395\}$ and $A_0 = \{0.2 - 1.25\}$ with increments of 0.01 and 0.05; and, (2) fine: $\langle S \rangle = \{0.125 - 0.174\}$ and $A_0 = \{0.65 - 0.85\}$ with increments of 0.0025 and 0.01.

Fourier transformations of these time-domain simulations at the $\chi^2(t_{ONP} = 144\text{ ms})$ minimum are plotted along with the frequency domain data in Fig. 4.13. Good agreement at the three shortest ONP times is immediately apparent, while the inset shows the experiment and simulation at $t_{ONP} = 3$ s, where, most notably, the analytical model undershoots the amplitude in the small-Knight-shift, large-radius regime. We attribute

this failure to the influence of spin diffusion, which carries optically pumped spin order from regions that are relatively near to $r = 0$ out to the extremities of the electronic state.

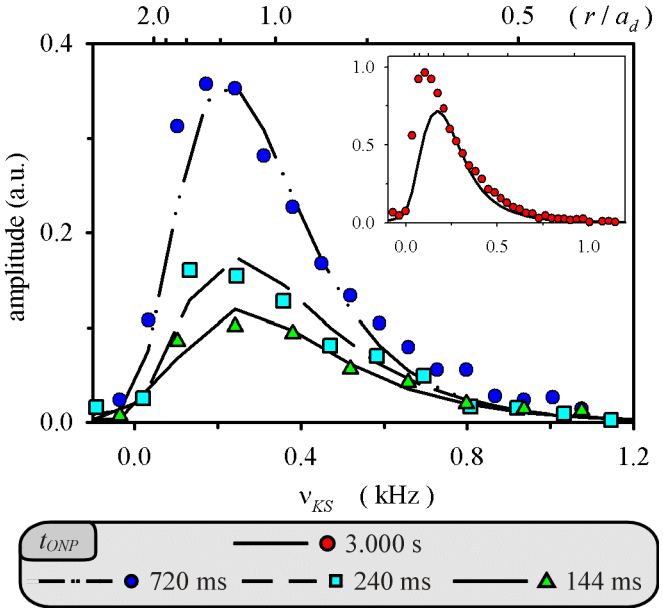

FIG. 4.13

^{71}Ga Knight-shift-distribution spectra (points) and corresponding simulations (lines). The parameter set used in each of the simulations is that which yields the minimum χ^2 in comparison of the time-domain simulation and spectrum at $t_{ONP} = 144$ ms. The inset highlights the failure of the analytical model at longer ONP times due to the influence of spin diffusion.

In addition to providing an image of the localized electronic wave function via the Knight shift's dependence on $|\Psi(\mathbf{r})|^2$, the fit result at $t_{ONP} = 144$ ms establishes an important one-to-one relationship between frequency (ν_{KS}) and radial position (r / a_d). This relationship is reflected in the labeling of the uppermost horizontal axis of Fig. 4.13 and is expressed by inserting Eqs. (4.4) – (4.7) for $|\Psi(\mathbf{r})|^2$ into Eq. (4.16) for $\nu_{KS}(r)$ and inverting the result to yield

$$\left(r / a_d\right) = \tfrac{1}{2}\left[\ln\left(\nu_{KS}(0)\right) - \ln\left(\nu_{KS}(r)\right)\right], \tag{4.41}$$

where

$$\nu_{KS}(0) = -\tfrac{2}{3}\, b\, \Gamma\, \mu_0\, g_0\, \mu_B\, \gamma_n^i\, \langle S \rangle\, d_i\, \Omega\, \left(\pi a_d^3\right)^{-1} \sim 2.5 \text{ kHz} \tag{4.42}$$

in these experiments. We have developed a novel scheme that takes advantage of this result in order to convert radially resolved Knight-shift-distribution spectra into an empirical radial-weighting function that replaces $A(t_{ONP}, r)$ of Eq. (4.40). In the next section, the empirical function is developed using the $t_{ONP} = 3$ s Knight-shift-distribution spectrum presented above. The result is of use in predicting the outcome of experiments in which spin diffusion may contribute and where the relation between position and frequency may be other than one-to-one. One such experiment is presented in Section D, where I detail the results of our characterization, via the LQSE, of the radial distribution of the electric field that is associated with the photoexcited electronic state.

Finally, in light of the above results, an additional comment on the optically induced relaxation dynamics discussed in Sections C.1 and C.2 is warranted here. The correlation time τ_c of fluctuations in the spin state of electrons trapped at the optically relevant defect is related to T_1^{opt} and ν_{KS} by Eq. (4.21). Furthermore, noting that from Eqs. (4.4), (4.6), (4.16) and (4.25),

$$\left|\nu_{KS}(r)\right|^2 T_1^{opt}(r) \;=\; \left|\nu_{KS}(0)\right|^2 T_1^{opt}(0)\,, \tag{4.43}$$

we may rewrite Eq. (4.21) as

$$(\omega_I - \omega_S)^2 \tau_c^{\,2} - \left(\frac{2\pi^2}{b^2 \left\langle S \right\rangle^2} \; T_1^{opt}(0)\, \nu_{KS}(0)^2 \right) \tau_c \;+\; 1 \;=\; 0. \tag{4.44}$$

Thus, in order that a physical (i.e., real) value of τ_c result from Eq. (4.44), it must be that

$$\left|\omega_I - \omega_S\right| \sim \left|\omega_S\right| \;\leq\; \left(\frac{\pi^2}{b^2 \left\langle S \right\rangle^2} \; T_1^{opt}(0)\, \nu_{KS}(0)^2 \right). \tag{4.45}$$

Inserting our results that $T_1^{opt}(0) = 16$ ms, $\langle S \rangle = 0.15$, and $\nu_{KS}(0) = 2.5$ kHz, and the corresponding parameter $b = 0.1091\overline{6}$, one finds the electron Larmor frequency corresponding to the maximum in Eq. (4.45):

$$\nu_S{}^{max} = (\omega_S{}^{max}/2\pi) \sim 586 \text{ MHz}. \tag{4.46}$$

Division of this result by the GaAs conduction-band electron gyromagnetic ratio,

$$\gamma_e = (g_e / g_0)\, \gamma_e{}^{free}, \tag{4.47}$$

where $g_e = -0.44$, yields the corresponding maximum field of ~95 mT, which is ~150 mT larger than the static field used in the experiments presented in this thesis. However, this apparent discrepancy is explicable as follows. In calculating the total field experienced by the localized electrons that are relevant to the present work, one must account for the influence of the optically pumped nuclear fields $\mathbf{B}_n^\alpha$ [see Eq. (1.20)] of each isotope α present in GaAs. These have been shown to be on the order of tens to hundreds of mT each.[4(e)] Furthermore, since the photoexcited electron spin is pumped antiparallel to $\mathbf{B}_0$ in our experiments, the $\mathbf{B}_n^\alpha$, which follow the electronic orientation, tend to cancel $\mathbf{B}_0$. This fact provides a plausible explanation for the surprisingly small upper bound on the electron Larmor frequency of Eq. (4.46) obtained when using our measured values for $T_1^{opt}(0)$, $\langle S \rangle$, and $\nu_{KS}(0)$. Furthermore, given that the $\mathbf{B}_n^\alpha$ are of the appropriate order of magnitude to sufficiently cancel (or overcome) $\mathbf{B}_0$, this calculation of the expected maximum field adds credence to the results of our relaxation experiments and to the fitting of the Knight-shift imaging spectra.

This analysis also highlights complexity in the phenomenon optically pumped nuclear spin relaxation that has not previously been considered. As noted in Paget's treatment of this problem,[7] determination of τ_c requires knowledge of each of $T_1^{opt}(0)$, ω_S and the magnitude of the hyperfine interaction. However, explicit inclusion of the effects of the $\mathbf{B}_n^{\alpha}$ was not discussed in his accompanying calculation of τ_c. Since Paget's experiments were performed at relatively high field and, furthermore, showed no apparent variation of measured $T_1^{opt}(0)$ values over the range $B_0 = 600 - 900$ mT, such omission may be valid in his application. However, at fields where the $\left|\mathbf{B}_n^{\alpha}\right|$ are comparable to B_0, their consideration gains importance. In such case, full rigor requires that one additionally consider the growth of the $\left|\mathbf{B}_n^{\alpha}\right|$ during ONP, which may yield corresponding time dependence in $T_1^{opt}(0)$. Explicit inclusion of such feedback in the nuclear-spin-relaxation dynamics is beyond the scope of this thesis. However, it is worthwhile at present to add the following comments aimed at gaining some sense of the significance of this omission.

If one takes Paget's[7] the calculated result, $\tau_c \sim 25$ ps, at face value, then, in the case where $\sum_{\alpha}\left|\mathbf{B}_n^{\alpha}\right|$ vanishes so that

$$\left|\omega_I - \omega_S\right| \sim \left|\omega_S\right| = 2\pi\gamma_e B_0, \tag{4.48}$$

the denominator in Eqs. (4.19) and (4.21) becomes

$$(1 + (\omega_I - \omega_S)^2 \tau^2) \sim 1.06 \tag{4.49}$$

4(e) Marohn, *et al*.[9] estimated nuclear spin polarization $P_n \sim 10\%$ under similar conditions on the same sample as that used here, while Eq. (1.20) provides, as Paget[6] found, $|B_n(^{75}\text{As}, ^{69}\text{Ga}, ^{71}\text{Ga}) / P_n| = 1.8$, 0.9 and 0.8 T, respectively.

for the experiments presented in this thesis. This result is exact at the start of ONP, which we recall is preceded by a saturation sequence, and, furthermore, should express the maximum deviation of the calculated quantity from unity provided that

$$\left| \mathbf{B}_0 + \sum\nolimits_{\alpha} \mathbf{B}_n^{\alpha} \right| \;\mathrm{d}\; B_0, \tag{4.50}$$

or equivalently,

$$\sum\nolimits_{\alpha} \left|\mathbf{B}_n^{\alpha}\right| \;\mathrm{d}\; 2\,B_0. \tag{4.51}$$

According to the estimates of the $\left|\mathbf{B}_n^{\alpha}\right|$ provided in footnote 4(d), this condition should hold at all times during both ONP and optical detection. Thus, even in our relatively low-field experiments, the product $\left(\omega_I - \omega_S\right)^2 \tau_c{}^2$ in Eqs. (4.19), (4.21) and (4.44) may be presumed negligible and, by association, so may the time dependence of $T_1^{opt}(0)$. However, to solidify this notion, a modified repetition of the experiments of Section C.2 for measure $T_1^{opt}(0)$, including investigation of its dependence on B_0, is indicated.

4. Empirical Radial Weighting

In the diffusion-free model, each of the factors determining the amplitude contributions $A(t_{ONP}, r_i)$ of single nuclear sites to the optically detected NMR signal depends on $|\Psi(\mathbf{r})|^2$. Thus, the analytical expression for $A(t_{ONP}, r_i)$ in Eq. (4.40) is rendered invalid when experiment timescales are sufficient for diffusion to transfer nuclear magnetization across sites where $|\Psi(\mathbf{r})|^2$ is distinguishable. In lieu of a separate analytical form that includes the complicated process of spin diffusion on a lattice of spins $\frac{3}{2}$, an experimental method of determining $A(t_{ONP}, r)$ is desirable. To this end, we have developed an approach that utilizes the one-to-one relationship between r and ν_{KS} of

Eq. (4.42), as established in short-ONP-time experiments, to convert any long-ONP-time Knight-shift spectrum into an image of the radial distribution of optically detected NMR signal amplitude at that value of t_{ONP}.

The mathematical formalism for this conversion is developed in Appendix C, while its step-by-step application to the previous results at $t_{ONP} = 3$ s is shown in Fig. 4.14. The procedure requires as input a Knight-shift-distribution spectrum at the ONP time of interest, knowledge of its underlying linewidth and the measured value of $\langle S \rangle$, the result is an empirical replacement for $A(t_{ONP}, r)$. Substituting r for the generalized coordinate ξ and Eqs. (4.4) – (4.6) and (4.16) for $\nu_{KS}(r)$ in Eq. (C.20) of Appendix C, we obtain the radial weighting for the total signal:

$$N_1(r)\, A(t_{ONP}, r) = \alpha r^2\, e^{-2r/a_d}\, \tilde{S}_d(t_{ONP}, \nu_1)\,, \tag{4.52}$$

where α is a constant for the overall scale, $N_1(r)$ is the radial density of nuclear spins given by Eq. (C.21), and the linewidth-deconvoluted Knight-shift distribution spectrum $\tilde{S}_d(t_{ONP}, \nu_1)$ is obtained as described in the caption of Fig. 4.14.

Figure 4.14(d) and (e) provides comparisons of the analytical and empirical functions at $t_{ONP} = 3$ s. Part (d) includes a plot of the data that corresponds to Eq. (4.52), as well as the empirical weighting function, which is a fit to that data, and the diffusion-free analytical function, which is given by the product of Eq. (4.40) and the quadratic radial dependence of $N_1(r)$. The empirical function reveals a redistribution of signal amplitude, relative to the analytical case, that matches the expectation that spin diffusion transfers optically pumped spin order from small to large r. The single-site weighting functions, obtained by dividing out $N_1(r)$, are plotted in part (e) of the figure.

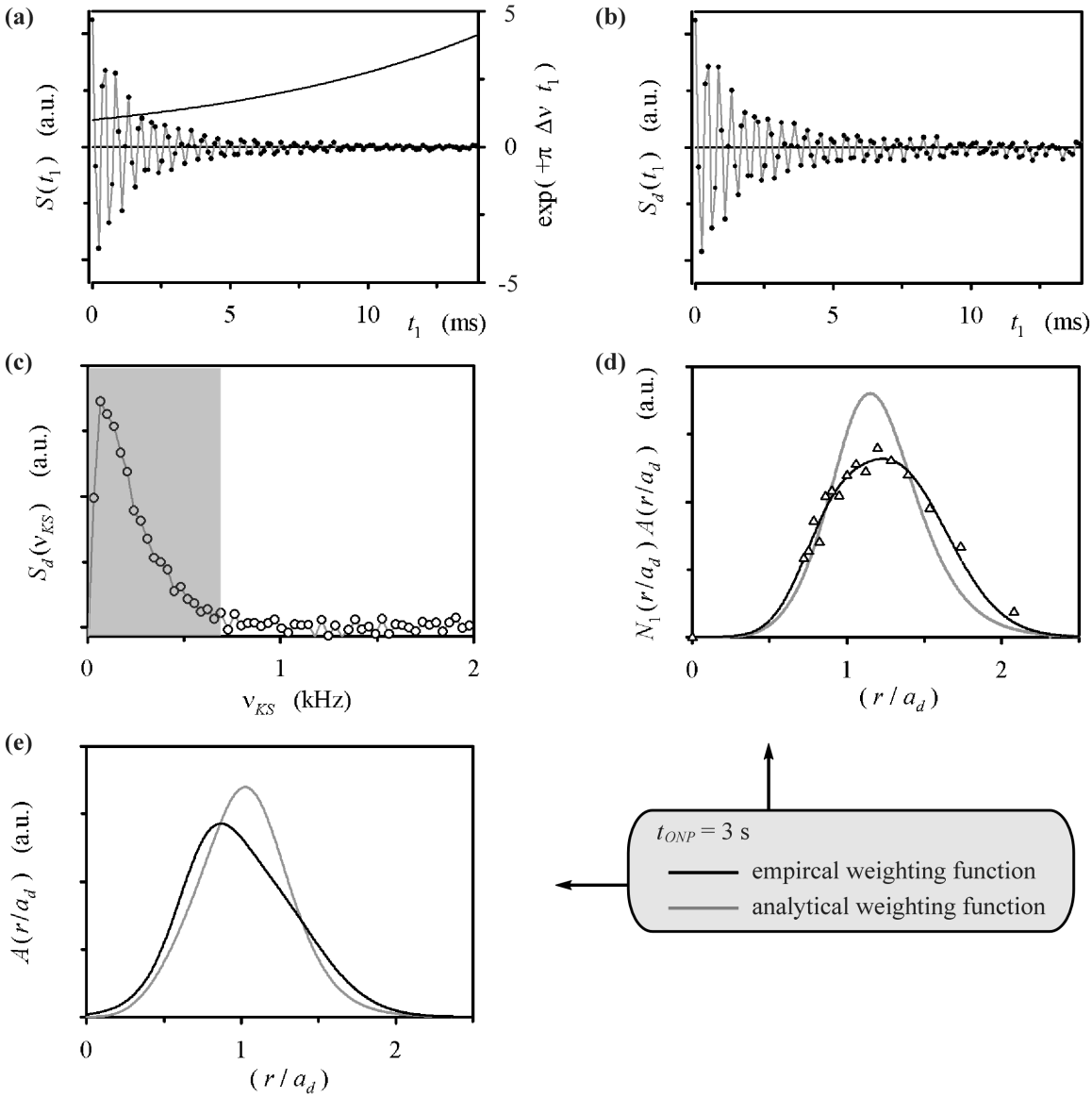

FIG. 4.14 Procedure for obtaining an empirical radial weighting function from a Knight-shift-distribution spectrum. Here, we treat the $t_{ONP} = 3$ s data presented in Figs. 4.10 and 4.13. **(a)** Plots of the time-domain spectrum $S(t_1)$ and the inverse decay, $e^{+\pi \Delta\nu\, t_1}$, of the corresponding light-off spectrum. **(b)** The linewidth-deconvoluted time-domain spectrum $S_d(t_1)$, which is the product of the two plots in (a). The lines connecting data points in both (a) and (b) serve only as a guide to the eye. **(c)** The linewidth-deconvoluted frequency domain spectrum $S_d(\nu_{KS})$ that results from Fourier transformation of (b) and subsequent referencing of $\nu_{KS} = 0$ to the homogeneous offset frequency in ν_1. Data in the shaded region is used in determining the empirical signal weights. **(d)** Radial weighting, $[N_1(r/a_d)\,A(r/a_d)]$, for the total optically detected NMR signal. The data points were obtained by conversion of the amplitudes in (c) according to Eq. (4.52), while the frequency axis was converted to one of radial position using Eq. (4.41) with the parameters of Table 4.2 and $\langle S \rangle = 0.15$. The empirical weighting function is a fit of two Gaussians to the combination of this data and a point inserted at $r = 0$, where the signal vanishes. The analytical function is the product of r^2 and Eq. (4.40) and is normalized here to yield the same total signal intensity as the empirical function. **(e)** The single-site radial weighting functions, which are the product of the weights in (d) and $(N_1(r))^{-1} \propto r^{-2}$ [see Eqs. (4.52) and (C.21)]. Parts (d) and (e) include similar results obtained from data collected at $t_{ONP} = 5$ s.

Replacing $A(t_{ONP} = 3\text{ s}, r_i)$ in Eq. (4.39) with the empirical function of Fig. 4.14(e) in simulation of the Knight-shift-distribution spectrum according to the procedure of Section C.3.*ii*, we obtain the result plotted in Fig. 4.15. The corresponding data and the earlier simulation that incorporated the diffusion-free analytical weights are also shown. The success of the new method is clear, as it yields apparently perfect overlap ($\chi^2 = 1.$) of the data and simulation. The true utility of the empirical weighting function, however, is its application with ONMR experiments in which the spectral observable does not exhibit a one-to-one relationship with the positions of contributing nuclei. In such a case, independent knowledge of the spatial dependence of the NMR observable, combined with the empirical function for the amplitude contributions, enables one to predict the experimental results with *no adjustable parameters*.[4(f)]

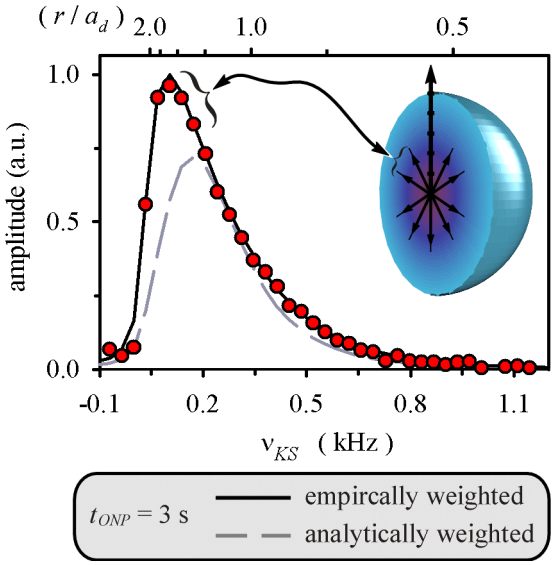

FIG. 4.15 Comparison of ^{71}Ga Knight-shift-distribution spectrum (points) with simulated results (lines) obtained using the analytical and empirical models for radial weighting. The inset indicates the influence of spin diffusion, which manifests in increased signal intensity in the small Knight-shift (large r) regime due to the transfer of optically pumped nuclear magnetization from near the center of localization out to the extremities of the electronic state. The empirical model successfully accounts for these effects.

[4(f)] The scale factor α in Eq. (4.52) is set by scaling the time-domain simulation to match the amplitude of the $t_1 = 0$ point with that of the observed spectrum, and thus is not a free parameter.

D. The Radial Electric Fields of Localized Electronic States

The POWER NMR measurements of the spatially varying Knight shift presented in the previous section demonstrate that the relevant electronic state is localized, and, furthermore, strongly indicate that the state is characterized by a radial wave function. However, distinct radial models, such as those corresponding to either a donor-bound electron or exciton, may be consistent with the observed distribution of Knight shifts. Meanwhile, these two particular cases do differ in the origin of the valence vacancy with which the photoexcited electron recombines to yield luminescence. In the excitonic case, a photoexcited hole accompanies the electron to the localization site, where the pair then recombines. In contrast, a donor-bound electron recombines at the localization site with a thermal vacancy that is initially spatially uncorrelated with the electron. Thus, as far as nuclei near the trapping site are concerned, optical excitation provides only an electron in the latter case, while both an electron and a hole arrive with photoexcitation and localization of an exciton.

In order to distinguish between these contending models and solidify our picture of the relevant electronic state, we require an experiment that is sensitive to the fate of the photoexcited hole. As noted in Section A.2 of the present chapter, POWER NMR characterization of the photoexcited LQSE measures the *light-induced change* in the local electric field, a quantity that reports on the presence of either type of charge carrier. We are left then with the task of distinguishing the spectral effects of an electric field that derives from either a bound *electron* or a bound *electron-hole pair*.

The remainder of this section is organized as follows. In Section D.1, the radial dependence of the localized photoexcited field for each of the noted electronic models is

derived, highlighting the measurable distinction between them. In Section D.2, POWER NMR experiments for high-resolution characterization of the optically induced LQSE are presented. These entail synchronization of optical pulses and the CLSW-16 sequence in a way that is similar to that used for characterization of the Knight-shift interaction, but here with $\mathbf{B}_0$ oriented along [110] for sensitivity to the LQSE. The results are compared with spectral predictions that are based on our knowledge of the angular dependence of the LQSE (see Section A.2), the empirical site-by-site amplitude-weighting model developed in the previous section, and the two contending models for the radial electronic state. Finally, in Section D.3, I propose an additional experiment, also characterizing the LQSE, which promises further insight into the nature of the electronic state characterized here, and which is of general utility for POWER NMR characterization of any quantum-confined electronic system via the LQSE.

1. Calculation of the Photoexcited Electric Field

For either a bound exciton or electron, the localized radial electronic state is described by a ground-state hydrogenic envelope centered at $r = 0$. Gauss' law provides the expression for a radial electric field,

$$\varepsilon(r) = \frac{q(r)}{4\pi\kappa\varepsilon_0} r^{-2}, \tag{4.53}$$

due to a confined spherical charge distribution centered at $r = 0$, where $q(r)$ is the fraction of the total charge bounded by the sphere of radius r. It remains then to determine the form of $q(r)$ for each of the contending electronic models. For this purpose, the electronic state is sufficiently described by an envelope function $\psi(r)$, i.e., we can ignore locality at the atomic level, such as the division of carrier density between Ga and As

sites in the unit cell, which was needed in calculation of the Knight shift. In general, the effective point charge at $r = 0$ experienced by a nucleus at r_i is

$$q(r_i) = q_0 \int_0^{2\pi}\int_0^{\pi}\int_0^{r_i} \left|\psi(r)\right| r^2 \sin\theta \, d\phi \, d\theta \, dr \,, \tag{4.54}$$

where the distribution of a single carrier with charge q_0 is given by $|\psi(r)|^2$. In the following, I evaluate the specific cases where $\psi(r)$ describes either a donor-bound electron or exciton.

i. The Donor-Bound Electron

The envelope wave function for the electron is $\psi_d(r)$ of Eqs. (4.6) and (4.7). Replacing $\psi(r)$ with $\psi_d(r)$ in Eq. (4.54), and inserting the result of the integration into Eq. (4.53) yields the radial electric field of a donor-bound electron:

$$\varepsilon_d(r_i) = \frac{-e}{4\pi\kappa\varepsilon_0} r_i^{-2} \left(1 - \left(1 + 2\left(r_i / a_d\right) + 2\left(r_i / a_d\right)^2\right) \exp(-2r_i / a_d)\right). \tag{4.55}$$

ii. A Fixed-Center-of-Mass Exciton

Derivation of the field distribution due to a trapped exciton is more complex. The most rigorous model for a bound exciton involves solution of a three-body problem that incorporates the excitonic pair and the fixed charge at the center of localization.[4(g)] The simplest model assumes an infinite hole mass, such that the electron and hole components of the exciton are described, respectively, by the donor envelope $\psi_d(r)$ of Eq. (4.54) and a point charge that coincides with the center of localization. Here, I develop a model of intermediate complexity in which a bound exciton is described in a coordinate system wherein the center of mass of the electron at $\mathbf{r}_e$ and the hole at $\mathbf{r}_h$ is taken to be fixed in

space at the center of localization. In the center-of-mass coordinate system, the exciton is described as a fictitious relative particle with the reduced mass,

$$\mu_x = \left(m_e^{-1} + m_h^{-1} \right)^{-1}, \tag{4.56}$$

of the electron-hole pair, and with a spatial distribution given by the radial envelope

$$\psi_x(r_x) = \left(\pi a_x^{\,3} \right)^{-1/2} \exp\left(-r_x / a_x \right), \tag{4.57}$$

where

$$a_x = a_B(\kappa/\mu_x) \tag{4.58}$$

is the effective Bohr radius of the relative particle, and

$$r_x = (r_e - r_h). \tag{4.59}$$

Using the relation

$$m_e r_e = m_h r_h \tag{4.60}$$

we have

$$\mathbf{r}_e = \left(r_e, \theta_e, \phi_e \right) \quad \text{and} \quad \mathbf{r}_h = \left(\frac{m_e}{m_h} r_e, \left(\theta_e + \tfrac{\pi}{2} \right), \left(\phi_e + \pi \right) \right), \tag{4.61}$$

where the origin $r = 0$ of the polar coordinate system locates the coincident centers of mass and localization of the electronic state. The combination of the expressions for these coordinates and Eq. (4.59) indicates that

$$r_x = r_e \left(1 + m_e / m_h \right) = r_h \left(1 + m_h / m_e \right). \tag{4.62}$$

Inspection of Eq. (4.62) reveals that the probabilities that the electron or hole is located within a region bounded by a spherical surface centered at $r = 0$ and with radius r_i are

---

[4(g)] Excitons are also known, for example, to trap on neutral donor sites,[68,69] in which case the solution of a four-body problem that accounts for the presence of a second trapped carrier is required.

equivalent to the integrated excitonic probability density out to values of the relative coordinate of

$$r_x^{\,e} = r_i\,(1 + m_e / m_h) \tag{4.63}$$

and

$$r_x^{\,h} = r_i\,(1 + m_h / m_e), \tag{4.64}$$

respectively. Thus, according to Eq. (4.54), the total individual-particle charges experienced by a nucleus at r_i and due to the electron and hole in this excitonic model are

$$q_e(r_i) = -e\int_0^{2\pi}\int_0^{\pi}\int_0^{r_i(1+m_e/m_h)} \left|\psi_x(r)\right| r^2 \sin\theta\, d\phi\, d\theta\, dr \tag{4.65}$$

and

$$q_h(r_i) = +e\int_0^{2\pi}\int_0^{\pi}\int_0^{r_i(1+m_h/m_e)} \left|\psi_x(r)\right| r^2 \sin\theta\, d\phi\, d\theta\, dr\,. \tag{4.66}$$

To find the corresponding contributions $\varepsilon_{x,\,e}(r_i)$ and $\varepsilon_{x,\,h}(r_i)$ to the distribution of the total electric field distribution, we insert Eq. (4.57) into Eqs. (4.65) and (4.66) and evaluate the integrals. Inserting those results into Eq. (4.53) and noting that

$$a_h^{-1} = a_x^{-1}\left(1 + m_h / m_e\right) \quad \text{and} \quad a_d^{-1} = a_x^{-1}\left(1 + m_e / m_h\right), \tag{4.67}$$

where

$$a_h = a_B\,(\kappa / m_h), \tag{4.68}$$

and a_d is the familiar Bohr radius of a donor-bound electron, we obtain

$$\varepsilon_{x,e}(r_i) = \varepsilon_d(r_i) \tag{4.69}$$

and

$$\varepsilon_{x,\,h}(r_i) = \frac{e}{4\pi\kappa\varepsilon_0}\, r_i^{-2}\left(1 - \left(1 + 2\left(r_i / a_h\right) + 2\left(r_i / a_h\right)^2\right)\exp(-2r_i / a_h)\right). \tag{4.70}$$

According to Eqs. (4.68) and (4.70), in the limit where $m_h \to \infty$, the total field distribution

$$\varepsilon_x(r_i) = \varepsilon_d(r_i) + \varepsilon_{x,\,h}(r_i) \tag{4.71}$$

of the fixed-center-of-mass exciton correctly reduces to that of a the donor-bound electron combined with a fixed positive charge at $r = 0$.

The radial profiles of the electric field corresponding to a donor-bound electron and a fixed-center-of-mass exciton that includes either a light or heavy hole are plotted in Fig. 4.16. Large differences exist between the profiles that correspond to each model, including changes in sign and magnitude of the field. In the following sections, the comparison of POWER NMR measurement of the optically induced LQSE with its simulation based on the profiles in Fig. 4.16 is used to distinguish between the contending electronic models.

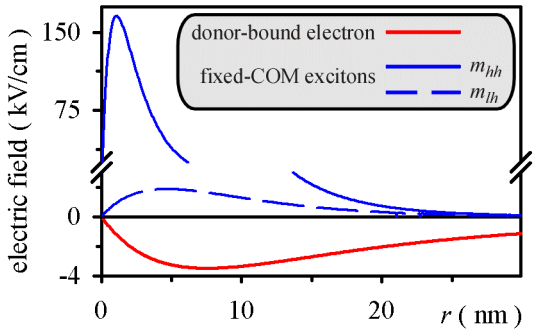

FIG. 4.16 Electric-field profiles for relevant localized radial electronic states. Note the change in scale after the break in the vertical axis.

2. POWER NMR Characterization of the Photoexcited Electric Field

i. Experimental Conditions and Parameters

Results were obtained using the standard timeline for pointwise evolution in t_1 with LBD in t_2. The inclusion of field-cycling delays [see Fig. 4.4(a)] allows for adiabatic reorientation of $\mathbf{B}_0$ such that it is parallel to [001] and the optical propagation axes during both ONP and detection, but along [110] during the NMR evolution period, as appropriate for sensitivity to the LQSE. The ONP time for each of the three primary isotopes in GaAs was 4.992 s, while ^{71}Ga and ^{75}As served as signal and reference nuclei, respectively. The duration of the detection period was $t_2^{max} = 2.256$ s, while, as in the

Knight-shift experiments of Section C, data from times $t_2 < t_2^{min} = 0.100$ s was excluded in integrating t_2 transients to obtain points in the 1D time-domain spectrum in t_1.

Comparison of spectra obtained with light-on and off versions of the CLSW-16 sequence provides the desired characterization of the photoexcited electric field. In the light-on case, the arrangement of optical pulses matches that shown in Fig. 4.17. For each experiment, we used σ_+ excitation at ~10 W/cm^2, a longitudinal field for ONP and detection of 246.5 mT, and a transverse evolution field of 57.8 mT, which corresponds to a ^{71}Ga resonance frequency of 750 kHz. For the particular results presented in this section, parameters of the rf excitation include $t_c = 120$ μs, $t_p = 4.00$ μs and $t_{off} = 200$ ns. Thus, according to the noted placement of optical pulses and Eq. (4.17), the light-on duty factor is $b = 0.2$.

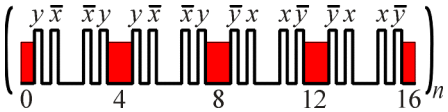

FIG. 4.17 The CLSW-16 sequence of rf pulses and optical pulses placed in evolution windows with labels matching those of Table A.1 in Appendix A.

ii. NMR Evolution under the Photoexcited LQSE

The single-site rotating-frame Hamiltonian $\tilde{\mathcal{H}}_{Q,i}$ that governs LQSE-induced nuclear spin evolution is obtained by insertion of the Euler angles $(\alpha, \beta, \gamma) = (\frac{\pi}{4}, \frac{\pi}{2}, 0)$, which correspond to the noted orientation of $\mathbf{B}_0$, into Eq. (4.13) for $\omega_{Q,i}(\alpha, \beta, \gamma)$, and that result into Eq. (3.13), to yield

$$\tilde{\mathcal{H}}_{Q,i}(\tfrac{\pi}{4}, \tfrac{\pi}{2}, 0) = \tfrac{1}{2}\,\omega_{Q,i}(\tfrac{\pi}{4}, \tfrac{\pi}{2}, 0)\,\left(I_{z,i}\right)^2 \tag{4.72}$$

in units of (radÿs^{-1}), where

$$\omega_{Q,i}(\tfrac{\pi}{4}, \tfrac{\pi}{2}, 0) = \frac{3eQC_{14}E_{001}(\mathbf{r}_i)}{2I(2I-1)\hbar}. \tag{4.73}$$

Except for the dependence of the electric field $E_{001}(\mathbf{r}_i)$ on nuclear position relative to the center of localization, this expression for $\omega_{Q,i}$ is identical in form to that of Eq. (3.18), which describes the influence of the interfacial field on nuclear spin evolution in a spin-echo experiment with the same orientation of $\mathbf{B}_0$. Because the interfacial field is not optically switched, its bearing on NMR evolution is averaged to zero by CLSW-16.

The average Hamiltonian that corresponds to Eq. (4.72) and the sequence of Fig. 4.17 is developed according to the process described in Section C.1 of Chapter 1. Executing that prescription with the toggling-frame trajectory of $I_z{}^2$ provided by Table A.1 of Appendix A, yields

$$\bar{\mathcal{H}}^{(0)}_{Q,i} = \tfrac{1}{2}\,\frac{b\,\omega_{Q,i}}{2\pi}\left(I_{z,i}\right)^2 = \tfrac{1}{2}\,\nu_{Q,i}\left(I_{z,i}\right)^2 \tag{4.74}$$

in units of Hz. Inserting $I = \frac{3}{2}$ into Eq. (4.73) and comparing with Eq. (4.74), we have

$$\nu_{Q,i} = \tfrac{1}{2}\,b\,e\,Q\,C_{14}\,E_{001}(\mathbf{r}_i)/h\,, \tag{4.75}$$

where the nuclear quadrupole moment Q and the constant C_{14} of the LQSE are given in Table 3.1. The total average Hamiltonian,

$$\bar{\mathcal{H}}^{(0)}_{i} = \nu_{off}\,I_{z,i} + \tfrac{1}{2}\,\nu_{Q,i}\left(I_{z,i}\right)^2, \tag{4.76}$$

that corresponds to the light-on sequence includes the homogeneous offsetting term provided by the modification of CLSW-16 presented in Fig. 1.13. Incidentally, although the optical excitation during the light-on sequence is circularly polarized, the Knight-shift interaction does not contribute to $\bar{\mathcal{H}}^{(0)}_{i}$, since the average photoexcited spin vanishes in the transverse field, and because, even if $\langle S\rangle \neq 0$, $\bar{\mathcal{H}}^{(0)}_{KS} = 0$ for this particular arrangement of optical pulses during the CLSW-16 sequence.

Single-site contributions to the NMR signal at times $t_1 = (n\, t_c)$ are given by

$$S_i(t_1) = A(t_{ONP}, r_i)\, e^{-\pi \Delta\nu\, t_1} \times \mathrm{Re}\left\{ Tr\left[I_+ \exp\left(-i\, \bar{\mathcal{H}}_i^{(0)}\, t_1\right) \rho(0) \exp\left(+i\, \bar{\mathcal{H}}_i^{(0)}\, t_1\right)\right]\right\}, \tag{4.77}$$

where $\rho(0) = I_y$ is the initial density operator provided by the $(\pi/2)_x$ preparation pulse on optically pumped nuclear spin magnetization and $\Delta\nu$ is the Lorentzian FWHM of the corresponding frequency domain light-off line shape. Inserting matrix representations for the spin operators in Eq. (4.77), we obtain

$$S_i(t_1) = A(t_{ONP}, r_i)\, e^{-\pi \Delta\nu\, t_1} \left[3\cos\left(2\pi(\nu_{off} - \nu_{Q,i})\, t_1\right) + 4\cos\left(2\pi \nu_{off}\, t_1\right) + 3\cos\left(2\pi(\nu_{off} + \nu_{Q,i})\, t_1\right)\right]. \tag{4.78}$$

According to this result, each nuclear site contributes homogeneously to a central transition at the offset frequency, but also provides position-dependent satellite peaks at $(\nu_{off} \pm \nu_{Q,i})$. Thus, we expect that the ensemble of sites that contribute to the total optically detected NMR signal provides a *distribution* of satellite intensity, which, according to Eq. (4.75) for $\nu_{Q,i}$, is determined by the site-by-site components along the [001] crystal axis of possible radial electric fields shown in Fig. 4.16.

Simulation of the experiment proceeds according to the site-by-site summation (see Section C.3.*ii*) of Eq. (4.78).[4(h)] At the 4.992 s ONP time used in the experiment, spin diffusion contributes to the signal dynamics during ONP and detection. Therefore, an empirical form of $A(t_{ONP}, r_i)$ is required to determine the radial distribution of signal intensity in simulation. The weighting function results from application of the procedure

[4(h)] The summation described in Section C.3.*ii* is over the positive octant of the lattice only. Care must be taken in application of that site-counting procedure to simulation of the LQSE, since $\nu_{Q,i} \propto E_{001}(\mathbf{r}_i)$ [see Eq. (4.75)] changes sign in certain other octants. The symmetry of Eq. (4.78) indicates that single-octant summation is sufficient in the present case; however, this is not true in general.

described above in Section C.4 to a Knight-shift-distribution spectrum collected with $t_{ONP} = 4.992$ s, as appropriate for modeling the present experiment.

No adjustable parameters of either the LQSE spin Hamiltonian or the electronic state were used in simulation. However, the central peak frequency in the light-on simulation was varied by ±2 Hz about $\nu_{off} = 1278.7$ Hz from the light-off experiment. This accounts for possible drift[4(i)] of the signal-nucleus resonance frequency from one experiment to the next. This yields small changes in the Rabi frequency ω_1, and hence, according to Eq. (1.35), in the homogeneous offset frequency. The center frequency yielding the best fits to the light-on data is ($\nu_{off} - 1.7$ Hz). Finally, the simulations used the underlying linewidth, $\Delta\nu = 20.3$ Hz, measured in the light-off experiment.

[4(i)] The primary suspect for drift of the resonance frequency is drift in the position of the laser spot on the sample relative to the center of the longitudinal field magnets. This may be due, for example, to a minute increase in the elevation of the cryostat (and probe) as boiloff reduces the volume of *l*-He therein.

iii. Predicted and Experimental Results

The light-on POWER NMR spectrum is plotted with the light-off reference data and simulations of each in Fig. 4.18(a). A broad distribution of electric-field-induced quadrupole splittings, most clearly evidenced by the amplitude reduction at $\nu_Q = 0$, is apparent in the light-on spectrum. The simulations shown in the figure predict the results in the cases where the photoexcited electronic state is a donor-bound electron or a fixed-center-of-mass exciton. Part (b) of the figure highlights differences between the light-on simulations that incorporate these two models. The buildup of satellite amplitude near the baseline for the donor-bound electron differs from the observed spectrum, which is closely matched by the fixed-exciton model. In the latter case, fast exchange between light- and heavy-hole excitons was assumed such that the radial field is given by

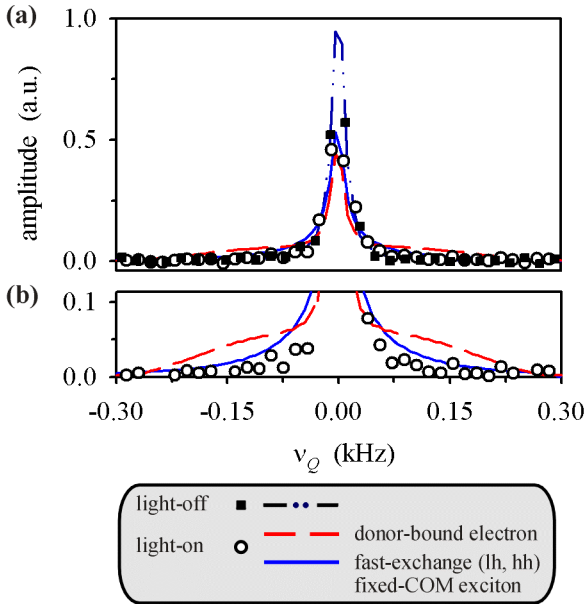

FIG. 4.18 **(a)** The light-on and off ^{71}Ga POWER NMR spectra (points) measuring the photoexcited LQSE and corresponding simulations (lines) calculated using the noted electronic models. Quadrupole splitting ν_Q is referenced to the light-off line position. **(b)** Expanded view highlighting the higher quality of the simulation that incorporated a fast-exchange fixed-center-of-mass exciton.

$$\varepsilon(r) = \varepsilon_d(r) + \tfrac{1}{2}\left(\varepsilon_{lh}(r) + \varepsilon_{hh}(r)\right), \tag{4.79}$$

where $\varepsilon_{lh}(r)$ and $\varepsilon_{hh}(r)$ are obtained by inserting m_{lh} and m_{hh} into Eqs. (4.68) and (4.70) for the component of the radial field due to the confined hole.

Table 4.4 contains the χ^2 values corresponding to the difference between the frequency domain data and light-on simulations for various models of the electronic state including those shown in Fig. 4.18. The rank order of the electronic models according to χ^2 is the same for several repetitions of the experiment. The donor-bound electron model is excluded from contention by these results. The model of a fixed-center-of-mass exciton provides the best fit to the data with the light-hole and fast-exchange cases yielding nearly identical χ^2 values. However, it is not possible to distinguish between such fine degrees of this simple model. Simulation with more realistic many-body states such as a neutral-donor-bound exciton may improve agreement between experiment and the excitonic simulation. Such relatively complex states share a radial distribution of electronic spin density and photocarrier field with those tested here and more easily reconcile with current knowledge of the *H*-band electronic states.[29,67]

Table 4.4 The χ^2 minima (with first non significant digit in subscript) resulting from comparison of the light-on frequency domain data shown in Fig. 4.18 with corresponding simulation of the photoexcited LQSE.

s	χ^2
donor-bound electron	$9_{.1}$
heavy-hole fixed-COM exciton ($m_h = 0.465\ m_0$)	$4_{.3}$
light-hole fixed-COM exciton ($m_h = 0.0.82\ m_0$)	$2_{.9}$
fast-exchange fixed-COM exciton	$2_{.9}$

3. An Alternative LQSE Reference: Homogeneous Quadrupolar Offsetting

One difficulty in interpreting the above experiments for measurement of the photoexcited electric field is that the satellite intensity provided by the LQSE is spread out near the base of the central transition. Since, to first-order, that peak is unaffected by quadrupolar effects,[102] both the light-off reference spectrum and the light-on

measurement of the photoexcited field present most of their signal intensity at $\nu_Q = 0$. Here, I propose an improvement upon the experiment, wherein the reference experiment is modified such that the corresponding spectrum includes homogeneously shifted satellite peaks. Thus, the spectral components that report on the spatially varying LQSE are resolved from the insensitive central transition.

The new approach requires the modification of CLSW-16 shown in Fig. 4.19. In this scheme, $\mathbf{B}_0$ remains along the [110] crystal axis; however, both the light-off and light-on versions incorporate externally applied rf electric-field pulses given by

$$\mathbf{E}(t) = E_0 \cos\left(\omega_E t\right) \hat{z}\,, \tag{4.80}$$

where $\hat{z}$ is the unit vector along the [001] axis and the phase of the rf electrical pulses and that of the nuclear rotating frame are set to zero. With ω_E set to twice the nuclear Larmor frequency and the pulses arranged during windows of CLSW-16 as shown in Fig. 4.19(a), we have the contribution

$$\bar{\mathcal{H}}^{(0)}_{Qoff,i}(\tfrac{\pi}{4}, \tfrac{\pi}{2}, 0) = \tfrac{1}{2}\, \omega_Q^{off}(\tfrac{\pi}{4}, \tfrac{\pi}{2}, 0)\, \left(I_{z,i}\right)^2, \tag{4.81}$$

to the total average Hamiltonian, where

$$\omega_Q^{off}(\tfrac{\pi}{4}, \tfrac{\pi}{2}, 0) = \left(e Q C_{14} E_0 / 12\hbar\right) \tag{4.82}$$

and E_0 is the positive amplitude of the applied cosinusoidal field. This result was obtained by inserting the Eq. (4.80) into Eqs. (B.18) and (B.21), discarding the remaining time-dependent parts of $\tilde{\mathcal{H}}_Q$ and averaging the toggling-frame representations of the time-independent terms as appropriate to their incorporation in the sequence in Fig. 4.19(a). This procedure is described in detail in one of our recent publications[25] and recounted ahead in Sections B.1 and B.2 of Chapter 5.

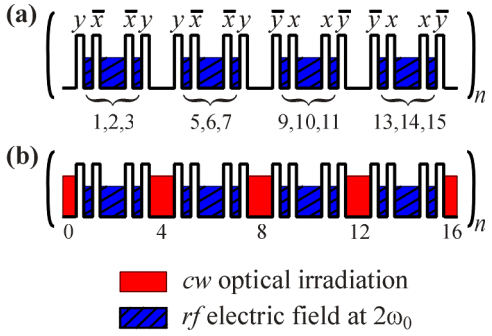

FIG. 4.19 Modified pulse sequences for POWER NMR measurement of the photoexcited LQSE with homogeneous contribution to the satellite offsets. **(a)** Light-off and **(b)** light-on versions. The rf magnetic modification of Fig. 1.13(b) is assumed for each sequence.

In the light-off reference experiment, $\bar{\mathcal{H}}^{(0)}_{Qoff,i}(\frac{\pi}{4}, \frac{\pi}{2}, 0)$ and the usual (magnetic) rf-induced offset term, $\bar{\mathcal{H}}^{(0)}_{off}$ of Eq. (1.35), are the lone contributors to the total average Hamiltonian. The result is a 3:4:3 symmetric triplet centered at ν_{off} with satellites separated from the central transition by

$$\left(\nu_Q^{off} / E_0\right) = \left(\omega_Q^{off} / 2\pi E_0\right) = 69\ \text{Hz} / (\text{kV/cm})\,, \tag{4.83}$$

which is obtained from Eq. (4.82) using the C_{14} and Q values that correspond to ^{71}Ga and which are listed on Table 3.1. The corresponding light-on sequence is shown in Fig. 4.19(b) and adds the site-dependent contribution $\bar{\mathcal{H}}^{(0)}_{Q,i}$ of Eq. (4.74) to the average Hamiltonian. The arrangement of optical pulses is identical to that in the previous section (see Fig. 4.17) and, since optical and rf electrical pulses occur in separate windows, enables one to probe the photoexcited states unperturbed by the applied electric field.

Simulated light-on and light-off spectra corresponding to the proposed sequences are shown in Fig. (4.20). Empirical radial weighting at t_{ONP} = 5 s and a 10 Hz Lorentzian FWHM of single-site contributions were used to calculate the results in parts (a) and (b) of the figure. As seen in part (a), the central transition of the light-on and light-off simulations directly overlap, while LQSE-induced structure appears only at the satellite peaks. Part (b) of the figure highlights the distributions of satellite intensity in light-on simulations including the photoexcited LQSE due to either a donor-bound electron or fast-exchange, fixed-center-of-mass excitons. These two cases are clearly distinguished in the simulation, benefiting from their separation from the uninteresting central transition.

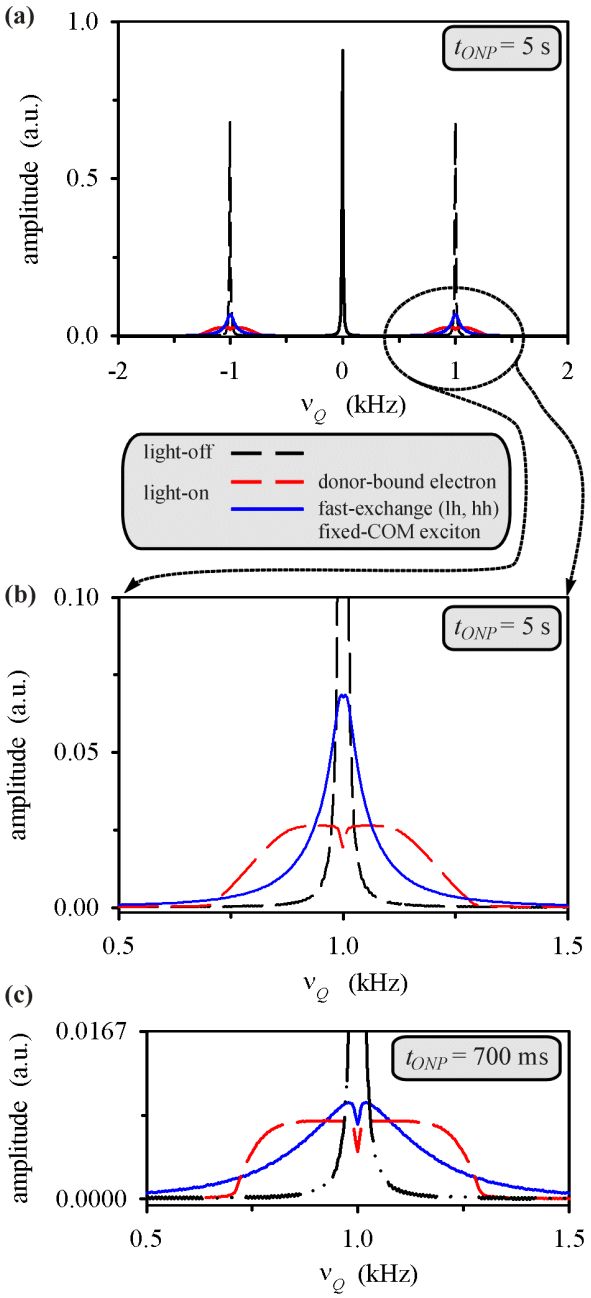

FIG. 4.20 Simulated results of POWER NMR experiments for measurement of the photoexcited LQSE with homogeneously offset quadrupolar reference satellites. **(a)** Long-ONP time simulation obtained using empirical radial weighting. **(b)** Expanded view of (a) highlighting the differences between the light-on simulations corresponding to the fast-exchange fixed-center-of-mass exciton and donor-bound electron models. **(c)** Similarly expanded view of simulated short-ONP time result.

Finally, part (c) of the figure shows the same simulations, but executed at $t_{ONP} = 700$ ms with the analytical amplitude weighting of Eq. (4.40). Qualitatively, the results show that, even barring reduction of the signal-to-noise ratio at short ONP times, it is more difficult to distinguish the electronic models using a short ONP time experiment. This is instructive for future experiments of this type, and, it must be stressed, highlights the utility of the empirical radial weighting model developed in Section C.4 and which is required to model the more informative long-ONP-time experiments.

E. Conclusions

I have presented the results of the first-ever high-resolution POWER NMR experiments. These have been used in conjunction with optically detected NMR to spatially image quantum-confined electronic states in GaAs. Radially resolved spectra characterize the microscopic spatial variation of the spin density and electric field associated with single photoexcited electronic states. Measurements of the relaxation constants governing the processes of ONP and spin-locked Larmor-beat optical detection of NMR complement the POWER NMR experiments. The resulting understanding of the diffusion-free signal dynamics enabled successful modeling of short-ONP-time Knight-shift distribution spectra in terms of single-spin physics summed over thousands of nuclear sites. The comparison of experimental and simulated POWER NMR Knight-shift images demonstrates that the photoexcited state responsible for the optical NMR signal is localized and radially symmetric with the Bohr radius expected for either a donor or an exciton. Further characterization of the nanoscale variation of the photoexcited LQSE supports the conclusion of Chapter 3 that excitonic recombination provides the *H*-band

luminescence in our single heterojunction sample, while *excluding* donor-bound electrons from contention.

The relatively long (~5 s) ONP times used for measurement of the photoexcited LQSE require a dynamic model of the NMR signal that accounts for the influence of spin diffusion during ONP and optical detection. Our novel empirical model for site-by-site weighting of contributions to the NMR signal accomplishes this feat. It is also noteworthy that our direct observations of the effects of spin diffusion on a spatially resolved signal present an opportunity for quantification of the corresponding dynamics and comparison with possible first-principle dynamics.

Finally, I have proposed a novel POWER NMR experiment for improved characterization of the photoexcited LQSE. The method is also applicable in experiments designed[103] to uncover the mechanism for recently observed[13] optically induced nuclear spin transitions, which we have suggested[25] are due to interactions of lattice nuclei with photoexcited electric fields similar to those characterized in this thesis

V. A Method for Atomic-Layer-Resolved Measurement of Polarization Fields

In this chapter I describe an NMR method of probing the dielectric response of quantum-confined carriers to an alternating electric field. The content here and in the related Appendices B and D is based directly on one of our recent publications.[25] The new method, which is applicable to non-centrosymmetric sites with nuclear spins $I > \frac{1}{2}$, utilizes an rf electric field to induce a linear quadrupole Stark effect (LQSE) at a multiple of the nuclear Larmor frequency. This perturbation is to be synchronized with an NMR multiple-pulse line-narrowing sequence according to the POWER NMR approach of the previous chapter. The application here extends that methodology to include conversion of nonsecular (off-diagonal) terms in the nuclear spin Hamiltonian into diagonal, first-order observables, which, in the present case, are quadrupole splittings of the nuclear resonance. A simulation of the ^{69}Ga spectrum for the nuclei within the 2D electron gas of a 10 nm quantum well predicts resolution of the NMR signals of individual atomic layers due to the spatial dependence of the polarization response of quantum-confined carriers to the applied field.

A. Introduction

In the early 1960s, Bloembergen and others studied the LQSE of the nuclear spin Hamiltonian in bulk GaAs, whereby an electric field gradient is induced at nuclear sites in proportion to the electric field at those sites.[60,61,80] Characterization of the spatial variation of the LQSE expected in single epitaxial structures requires high NMR sensitivity and spectral resolution. In recent decades the phenomena of optical nuclear polarization, equilibrium and optically induced Knight shifts, and several methods of optical detection have resulted in great gains in sensitivity, spatial selectivity and spectral resolution relative to the traditional solid-state NMR experiment.[3-5,7-9,11,13,94] This has allowed application of optical NMR to III-V heterostructures,[9] quantum wells[16,17,19,21,22] (QWs) and quantum dots[11].

Of particular relevance here are advances from our group enabling *high-resolution* time-domain optically detected NMR.[8,9] As noted in the previous chapter, the highest spectral resolution is achieved in experiments where perturbations of the sample, such as the electric field in the LQSE, are synchronized with time-suspension NMR multiple-pulse sequences to measure differences between the perturbed and unperturbed spin Hamiltonians: the POWER NMR approach. In the experiments presented in Chapter 4, we probed the shallow point defects at which optical excitations localize in AlGaAs/GaAs heterojunctions using two different examples of POWER NMR with secular, optically-induced spin Hamiltonians. The radial distribution of optically switched electron density was observed as a high-resolution Knight shift distribution, and

the associated changes in radial electric field were measured by the diagonal terms of the LQSE.[26]

Here we introduce a novel technique within the general class of POWER NMR, whereby a radiofrequency (rf) LQSE is used to measure a third electronic property, the polarization response to an rf electric field. In particular, we propose measurement of the response expected for electrons in an *n*-type GaAs QW. Our approach relies on conversion of nonsecular (off-diagonal) terms in the nuclear quadrupole Hamiltonian $\mathcal{H}_Q$ into an effective secular observable (a first-order splitting in the sample's NMR spectrum) by varying the electric-field-induced interaction at twice the nuclear Larmor frequency in selected windows of a time-suspension[50,51] NMR multiple-pulse sequence. Both this transformation of a nonsecular perturbation into a high-resolution secular observable and the proposed localized measurement of dielectric response are novel aspects of this work.

On bulk samples in experiments where resolution was limited by dipolar broadening, the rf LQSE has been used previously to depolarize nuclear spins in GaAs,[63,104] while the inverse of the rf LQSE has been used to realize electrically detected nuclear quadrupole resonance.[64,105] In contrast, we predict that, by employing POWER NMR and isotopic dilution, our technique can yield NMR line shapes with atomic-layer resolution that report on the rf LQSE in a GaAs QW sample. Generalizations of this spin physics may be useful in other situations where rf perturbations modulate nonsecular spin interactions.

An outline of the remaining text follows. In Section B, I derive the average nuclear spin Hamiltonian pertinent to POWER NMR manipulation of the rf LQSE. This development is grounded in the presentation of the physical basis for the general LQSE and the corresponding rotating-frame Hamiltonian in Appendix B. In Section C, I develop the form of the rf polarization response of *n*-type carriers in a QW and determine nuclear spin evolution due to synchronization of this response with NMR multiple-pulse line narrowing. The form obtained for the polarization response is justified by a second-order perturbation-theory treatment of a particle-in-a-box model presented in Appendix D. Finally, in Section D, I present and discuss the simulated NMR spectrum, predicting resolved features due to individual atomic layers.

B. Fundamental Concepts

The normally truncated terms of the rotating-frame quadrupole Hamiltonian $\tilde{\mathcal{H}}_Q$ of Eq. (B.18) are the terms of interest here for extending POWER NMR to include the conversion of nonsecular terms into diagonal, secular observables. If the electric-field perturbation of the LQSE oscillates at ω_0 or $2\omega_0$, then either the $V'_{2,\pm1}$ or $V'_{2,\pm2}$ coefficients, respectively, are time dependent in a way that partially cancels the time dependence of their corresponding rotating-frame operators, yielding a new static, but off-diagonal, observable in $\tilde{\mathcal{H}}_Q$.

Brun *et al*.[63,104] took advantage of this resonance phenomenon to characterize the combined influence of $\mathbf{B}_0$, thermal spin-lattice relaxation and rf-electric-field-induced $\Delta m = \pm 2$ transitions at $2\omega_0$ on the equilibrium magnetization of ^{69}Ga, ^{71}Ga and ^{75}As in bulk GaAs, including its angular dependence. Investigation of $\Delta m = \pm 1$ electric

transitions by the rf LQSE at ω_0 is problematic, due to possible incidental excitation of $\Delta m = \pm 1$ magnetic transitions. However, we note that recent unexplained observation[13] of optically induced NMR transitions with light pulsed at either ω_0 or $2\omega_0$ may be due to the rf LQSE induced by the photocarrier electric field.

1. The Double-Quantum Spin Hamiltonian

In the present work, we are interested in the $\tilde{T}_{2,\pm 2}$ interaction of $\tilde{\mathcal{H}}_Q$, which is described by Eqs. (B.9), (B.15), (B.18) and (B.20) of Appendix B. This "double-quantum" component of the quadrupole interaction may be reintroduced into the secular Hamiltonian using an external electric field,

$$\mathbf{E}(t) = E_0 \sin(2\omega_0 t + \phi_E)\, \hat{z}\,, \tag{5.1}$$

that is parallel to $\mathbf{B}_0$ and the [001] crystal-growth axis, which define $\hat{z}$. E_0 is the positive amplitude of the applied field and ϕ_E its phase with respect to the rotating-frame phase ϕ_{rf}. Before considering the possible additional response in a structured sample (e.g., of the electrons in an *n*-type QW), which we leave to Section C of the current chapter, we now consider the uniform effect of $\mathbf{E}(t)$ on the spin system. Inserting Eqs. (B.21) and (5.1) into Eq. (B.18), and substituting for the Euler angles, $\alpha = \beta = \gamma = 0$, that correspond to this orientation of $\mathbf{B}_0$, we obtain the part of $\tilde{\mathcal{H}}_Q$ that is proportional to $\tilde{T}_{2,\pm 2}$:

$$\tilde{\mathcal{H}}_{Q2} = \frac{i\, e\, Q\, C_{14}\, E_0}{2I\,(2I-1)\,\hbar}\ \sin(2\omega_0 t + \phi_E)\left(T_{2,-2}\ \mathrm{e}^{-2\,i\,\omega_0\,t} - T_{2,+2}\ \mathrm{e}^{+2\,i\,\omega_0\,t}\right), \tag{5.2}$$

where we have defined the rotating-frame phase $\phi_{rf} = 0$. Truncating the remaining time-dependent parts of $\tilde{\mathcal{H}}_{Q2}$ yields

$$\tilde{\mathcal{H}}_{Q2} = \frac{e\,Q\,C_{14}\,E_0}{4I\,(2I-1)\,\hbar}\,\left(T_{2,-2}\;e^{+i\,\phi_E} + T_{2,+2}\;e^{-i\,\phi_E}\right), \tag{5.3}$$

which, using Eq. (B.9), becomes

$$\tilde{\mathcal{H}}_{Q2} = \frac{e\,Q\,C_{14}\,E_0}{4I\,(2I-1)\,\hbar}\,\left((I_x{}^2 - I_y{}^2)\cos\phi_E + (I_x I_y + I_y I_x)\sin\phi_E\right). \tag{5.4}$$

Though secular, $\tilde{\mathcal{H}}_{Q2}$ remains off diagonal. In the next section, I describe how, using POWER NMR, $\tilde{\mathcal{H}}_{Q2}$ can be converted into a convenient diagonal form, and, it must be stressed, isolated from other spin interactions as the dominant source of spectral structure.

2. High-Resolution Evolution under the rf LQSE by POWER NMR

In order to best characterize the rf polarization response to $\mathbf{E}(t)$ at $2\omega_0$ by way of Eq. (5.4), we would like to eliminate, in so far as it is possible, other contributions to the linewidth. These may include static contributions to the secular quadrupole interaction from the equilibrium bonding environment (absent in the bulk GaAs lattice, but not necessarily so in structured epitaxial samples), from crystal strain or even from the LQSE due to static electric fields. Direct dipolar interactions of the target spin with like and/or unlike nuclei are ubiquitous, and here undesirable. Finally, a distribution of the Zeeman interaction due to inhomogeneity of the applied field, susceptibility effects or hyperfine fields can contribute to the linewidth.

As in Chapter 4, these deleterious contributions to the spin Hamiltonian are effectively removed in an evolution period governed by the time-averaged Hamiltonian $\bar{\mathcal{H}}^{(0)}$ provided by a time-suspension[50,51] pulse sequence such as CLSW-16. This sequence averages to zero the chemical shift interaction, dipolar couplings, heteronuclear *J*-couplings and quadrupolar terms that are not switched during the pulse sequence,

leaving only the rotationally invariant homonuclear *J*-coupling between spins *i* and *k*, with Hamiltonian

$$\tilde{\mathcal{H}}_J^{\,ik} = J_{ik}\,\mathbf{I}_i \cdot \mathbf{I}_k\,. \tag{5.5}$$

Figure 5.1 depicts the POWER NMR modification of CLSW-16 that is relevant for application during the evolution period of the proposed experiment timeline. The LQSE perturbation at $2\omega_0$ is included during the shaded windows of the sequence using the same value of ϕ_E in all application windows. The contribution $\bar{\mathcal{H}}_{Q2}^{(0)}$ of $\tilde{\mathcal{H}}_{Q2}$ to the total average Hamiltonian is obtained using the procedure outlined in Section C.1 of Chapter 1 and the toggling-frame trajectory of double-quantum spin operators listed in Table A.1 of Appendix A. This procedure provides

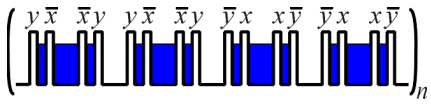

FIG. 5.1 Arrangement of rf electrical pulses at $2\omega_0$ during the CLSW-16 sequence.

$$\bar{\mathcal{H}}_{Q2}^{(0)} = \frac{e\,Q\,C_{14}\,E_0}{4I\,(2I-1)\,\hbar}\;(I_z{}^2 - \tfrac{1}{3}\mathbf{I}^2)\;\cos\phi_E \tag{5.6}$$

as the dominant term in $\bar{\mathcal{H}}^{(0)}$ for the proposed experiments.

Note that, though derived from Eq. (5.4), $\bar{\mathcal{H}}_{Q2}^{(0)}$ is diagonal due to transformation by the sequence shown in Fig. 5.1. Thus, for experiments that sample the magnetization only after an integral number of repetitions of the cycle, the effect of $\bar{\mathcal{H}}_{Q2}^{(0)}$ is analogous to that of the familiar static, secular quadrupolar Hamiltonian. For a spin $I = \frac{3}{2}$, Eq. (5.6) yields the familiar triplet pattern in the NMR spectrum given by Eq. (3.16). However, in the present case, the angular frequency separating the satellite transitions from the central transition is

$$\omega_Q = \frac{e\,Q\,C_{14}\,E_0}{6\,\hbar}\ \cos\phi_E\,, \tag{5.7}$$

and henceforth, we choose $\phi_E = 0$.

C. Application to *n*-Type QWs

The goal of this section is to describe a specific example, wherein the polarization response of quantum-confined electrons to $\mathbf{E}(t)$ is observable with the POWER approach via rf-LQSE-induced quadrupole splittings. As above, the directions of both $\mathbf{B}_0$ and the rf electric field are parallel to the [001] crystal axis. We evaluate the field at each layer of the quantum well as the sum of a homogeneous part, as would be present due to an applied voltage drop across bulk GaAs, and a part which is due to the 2D electron gas, as distorted by that homogeneous part. In Appendix D, the distribution of *n*-type carriers in the QW is calculated with a particle-in-a-box model of the ground-state electronic envelope $\psi(z)$ perturbed by the electric field. This wave function gives rise to the spatially varying part of the internal polarization field $\mathbf{E}_{\rm int}$ through Gauss' law

$$\nabla\cdot\mathbf{E}_{\rm int} = \frac{\partial}{\partial z}E_{int,z} = \frac{\rho_e(x,y)}{\kappa\varepsilon_0}\,|\psi(z)|^2\,, \tag{5.8}$$

where $\rho_e(x, y)$ is the sheet density of charge in the QW. Only the electric field of the quantum-confined space charge is included in $\mathbf{E}_{int}$ and the QW is taken to be symmetric.[5(a)] The perturbation theory treatment in Appendix D yields

[5(a)] The later assumption yields little effect on subsequent calculations presented here. We have calculated that if the initial QW wave function $\psi(z)$ were perturbed by a large 10 kV/cm *inherent* slant in the QW potential, the largest resulting fractional shift of any single quadrupole satellite in the rf LQSE spectrum of a 10 nm GaAs QW would be only 2×10^{-2}. If, however, it is desired to characterize such deviations from the flatband condition, POWER NMR experiments in which the carrier density is modulated in synchrony with NMR multiple-pulse line narrowing are more appropriate.

$$\psi(z) = a^{-1/2}\cos\left(\frac{\pi z}{2a}\right) - a^{1/2}c_0\sin\left(2\omega_0 t + \phi_E\right)\sin\left(\frac{\pi z}{a}\right), \tag{5.9}$$

where

$$c_0 = \frac{128\, m_e\, a\, \Phi_0}{27\,\hbar^2\pi^4}, \tag{5.10}$$

$2a$ is the width of the QW, and $\Phi_0 = 2\,a\,eE_0$ is the linear rise in the box potential from $z = -a$ to $z = a$ provided by $\mathbf{E}(t)$ in Eq. (5.1). It is sufficient to treat $\mathbf{E}(t)$ as a *stationary* perturbation to the 1D particle-in-a-box potential since it is weak and its frequency is much smaller than the lowest spatial Bohr frequency. After inserting Eq. (5.9) into Eq. (5.8), we integrate the resulting expression with respect to a dummy variable in place of z from $-a$ to z and from z to a. The latter of these two results is subtracted from the former, yielding

$$\begin{aligned} E_{int}(z,t) = \frac{-\rho_e(x,y)}{\kappa\varepsilon_0}\Bigg[&\left(\frac{1}{a} + \frac{c_0^2 a}{2}\right)z + \pi^{-1}\sin\left(\frac{\pi z}{a}\right) - \frac{c_0^2 a^2}{4\pi}\sin\left(\frac{2\pi z}{a}\right) \\ &+ \cos\left(4\omega_0 t + 2\phi_E\right)\left(\frac{c_0^2 a^2}{4\pi}\left(\sin\left(\frac{2\pi z}{a}\right) - \frac{2\pi z}{a}\right)\right) \\ &+ \sin\left(2\omega_0 t + \phi_E\right)\left(\frac{4c_0 a}{\pi}\left(\tfrac{1}{3}\cos\left(\frac{3\pi z}{2a}\right) + \cos\left(\frac{\pi z}{2a}\right)\right)\right)\Bigg]. \end{aligned} \tag{5.11}$$

There are three distinct components of $E_{int}(z, t)$: a time-independent component on the first line of Eq. (5.11), and components at $4\omega_0$ and $2\omega_0$. Each of the three terms induces an electric-field gradient with corresponding time dependence; however, we can ignore the contribution of the electric field oscillating at $4\omega_0$, which is both small and off-resonance, and of the dc term, which induces a stationary component in $V'_{2,\pm2}$ that does not cancel the time dependence of $\tilde{T}_{2,\pm2}$. The *total* electric field oscillating at $2\omega_0$, including the component

$$E_2(z) = \frac{-\rho_e(x,y)}{\kappa\varepsilon_0}\left(\frac{4c_0 a}{\pi}\left(\frac{1}{3}\cos\left(\frac{3\pi z}{2a}\right)+\cos\left(\frac{\pi z}{2a}\right)\right)\right) \quad (5.12)$$

from the last line in Eq. (5.11), is resonant with $\tilde{T}_{2,\pm 2}$; thus, we must replace E_0 in Eqs. (5.6) and (5.7) with $\left(E_0 + E_2(z)\right)$.

The contribution of $E_0(t)$ to the total electric field oscillating at $2\omega_0$ is spatially homogeneous, inducing a uniform contribution to nuclear quadrupole splitting independent of z. However, the spatial dependence of $E_2(z)$ adds atomic-layer-dependent fine structure to the uniform contribution. The uniform effect provides two advantages: (1) spectral resolution of the informative satellites from the unshifted central transition, and (2) calibration of the system response to a known voltage drop. The amplitude of the distribution of $E_2(z)$ across the QW is depicted in Fig. 5.2, while the corresponding LQSE-induced quadrupole splitting for ^{69}Ga, calculated from Eq. (5.7), is indicated on the right-hand vertical axis.

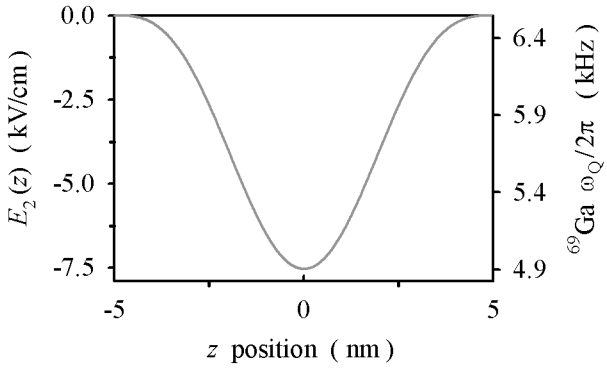

FIG. 5.2 The amplitude of $E_2(z)$, which is the component of $E_{int}(z, t)$ that is sinusoidally time dependent at twice the Larmor frequency of the NMR signal nucleus. The result was calculated for a symmetric 10 nm GaAs QW, assuming $\rho_e(x, y) = 1.6\times10^{-3}$ C/m^2, which corresponds to 10^{12} electrons/cm^2, $\kappa = 13.1$ and $m_e = 0.067\ m_0$. The amplitude of $E_0(t)$ used to obtain the result shown here was 30 kV/cm. The corresponding calculated ^{69}Ga quadrupole splitting of Eq. (5.7) and induced by the *total* field $[E_0(t) + E_2(z, t)]$ is given on the right-hand vertical axis.

D. Results and Conclusions

The time evolution of the transverse nuclear magnetization up to time $t = n\,t_c$, where t_c is the duration of the CLSW-16 sequence, is calculated using the density matrix formalism as

$$\langle I_+ \rangle(t) = Tr\left[I_+ \; U(t)\; \rho(0)\; U^\dagger(t) \right] \tag{5.13}$$

with

$$U(t) = \exp(-i\,\bar{\mathcal{H}}^{(0)} t)\,. \tag{5.14}$$

The initial condition $\rho(0)$ of the density matrix is taken to be I_x, as results from a $(\pi/2)_y$ preparation pulse prior to the start of the cycle.

In order to estimate the residual linewidth, we must consider the contribution to $\bar{\mathcal{H}}^{(0)}$ of the homonuclear *J*-coupling represented by $\tilde{\mathcal{H}}_J{}^{ik}$ in Eq. (5.5), which enters due to the non-equivalence of spins in adjacent atomic layers. Potter and Wu have used a novel echo-decay analysis of ^{69}Ga and ^{71}Ga NMR signals to estimate that for nearest-neighbor interactions of like spins (i.e., two-bond couplings) $J_{ik}(^{69}\text{Ga})/2\pi = 41$ Hz and $J_{ik}(^{71}\text{Ga})/2\pi = 60$ Hz.[106] Using these values, spectral features resulting from the homonuclear *J*-coupling have been included in a simulation where $\tilde{\mathcal{H}}_J{}^{ik}$ is truncated to a diagonal form by the difference in quadrupole coupling between layers. A given spin couples to a given number (between 0 and 12) of same-isotope nearest neighbors, thus spectra for each case, weighted both for the isotopic abundance of the species and for the number of ways to permute the given number of like nuclei among the twelve nearest-neighbor positions, were added. The envelope of the resulting distribution of frequency domain peaks was replaced by a best-fit Lorentzian. We expect that this gives an upper

bound to the width that would result from the actual many-body dynamics, which is not tractable with known methods. Using this approach, a 200 Hz FWHM linewidth is estimated for ^{71}Ga when present at its natural isotopic abundance of 39.6%. Such a linewidth obscures some of the atomic-layer information in simulation of the resulting ^{71}Ga spectrum, as shown in Fig. 5.3(a). However, the same linewidth-estimation procedure predicts a 10 Hz FWHM of the ^{69}Ga signal for a sample with 5% ^{69}Ga isotopic abundance, which is sufficient for atomic-layer resolution [see Fig. 5.3(b)]. Recall from Fig. 1.12 that linewidths < 5 Hz FWHM have been obtained experimentally with CSLW-16, proving that the other interactions can be removed to this degree in GaAs.

In simulation of the NMR experiment with the timeline shown in Fig. 5.1, we weighted each atomic layer's contribution to the signal expressed in Eq. (5.13) by the square of the QW's unperturbed ground-state envelope function at that layer. This is appropriate to optical detection methods based on the hyperfine coupling. However, as shown in Section C of Chapter 4, more complex weighting may be necessary to quantitatively account for amplitude variations due to optical nuclear polarization, spin diffusion, and hyperfine relaxation. Spectrally resolving individual layers would facilitate the investigation of these effects, by making information contained in the amplitude and frequency of the lines readily separable.

We summed the contributions from three separate calculations with 35, 36, and 37 atomic layers of Ga (~ 10 nm quantum wells) weighted by ½, 1 and ½, respectively, to obtain some sense of how predicted spectral features would be sensitive to the thickness variations typical of state-of-the-art epitaxial growth. The portion of the simulated ^{69}Ga (5% isotopic abundance) frequency domain spectrum containing satellite features is

presented in Fig. 5.3(b), where the atomic-layer-resolved fine structure of the positive frequency quadrupole satellite is clear. The uniform contribution to the quadrupole splitting of about ~6.5 kHz due to the homogeneous rf LQSE of $E_0(t)$ is apparent in the simulated result, which is aliased around a Nyquist frequency of $4.1\overline{6}$ kHz that corresponds to a practical CLSW-16 cycle time of 120 μs.

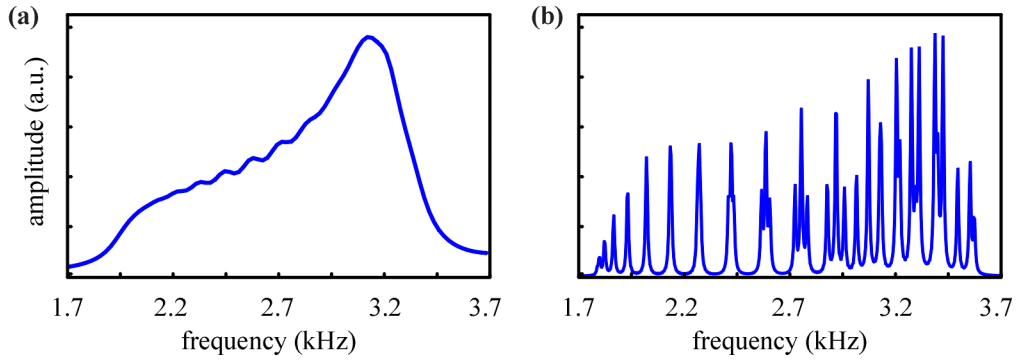

FIG. 5.3 **(a)** The simulated distribution and linewidth of ^{71}Ga quadrupole *satellites* of a 10 nm (36±1 atomic layers) GaAs quantum well (QW) with natural isotopic abundance. Central transition features (not shown) overlap at zero frequency in the rotating frame. The field distribution assumed in the simulation is the response of a quantum-confined carrier density of 10^{12} cm^{-2} to an applied rf electric field of 46 kV/cm along the [001] growth direction. The 200 Hz linewidth estimate of contributing features is discussed in the text. **(b)** The same simulation, but for ^{69}Ga with 5% isotopic abundance (10 Hz individual linewidths) and a 30 kV/cm rf electric field. Many of the resonances due to individual atomic layers are resolved. Pairs of atomic layers that are located symmetrically across the QW center contribute identically overlapping satellites to the simulation. The largest amplitude feature corresponds to the contribution of the pair at the center of the 36-layer QW, while the smallest amplitude features correspond to atomic layers at the QW edges. Because the contribution of a 36-layer QW is combined with ½-weighted 35 and 37-layer contributions to the simulation, some features appear as closely spaced triplets with each line arising from a layer in a QW of each width. Finally, note that because the simulation is aliased about the $4.1\overline{6}$ kHz Nyquist frequency, the depicted structrure is a reflection of the true frequency ordering of spectral lines into a mirror at the Nyquist frequency. Hence, the lines at right have the smallest net quadrupole splitting resulting from the partial cancellation of the applied field by the polarization response [E_2(z) of Fig. 5.2].

The simulations of Fig. 5.3 predict that atomic-layer-resolved spectroscopy should be possible in quantum wells using the rf LQSE with POWER NMR to provide an unprecedented local probe of electric fields and spin interactions. The analysis assumes

that the LQSE coefficients measured in the bulk are also appropriate to a quantum well, a question that deserves fuller theoretical examination. From simple electrostatics, the contribution to the quadrupole interaction due to the field gradient of the envelope of the electron gas itself is negligible, in contrast to the effect calculated here, which is mediated by the LQSE dominated by covalent electrons. The particle-in-a-box model could readily be modified to include the finite well depth, which would result in finite NMR amplitude at and beyond the interface with the AlGaAs barrier. However, for several layers around the interface, it is anticipated that the heterogeneity of the bonding will lead to static quadrupole interactions whose tensors are unknown, but likely of a sufficient magnitude ($\gtrsim 20$ kHz) that the multiple-pulse line narrowing as presented may fail for these few layers. Detailed simulation of these effects is possible and would aid in resolving and identifying the NMR transitions of interface layers, which has not been possible with methods applied to QWs to date.

Finally, it is worth noting that this new approach to high-resolution NMR may have useful analogs quite independent of the LQSE. For example, analogous nonsecular terms induced by sound waves (strain) are the basis for inducing transitions in nuclear acoustic resonance. The present work suggests a high-resolution analog based on the POWER approach.

Appendix A. Toggling-Frame Operators from the CLSW-16 Sequence

Contributions to the average Hamiltonian $\bar{\mathcal{H}}^{(0)}$ that governs nuclear spin evolution over an integer multiple of CLSW-16 cycles are transformations of rotating-frame operators into the toggling-frame interaction representation. As described in Section C.1 of Chapter 1, such transformation of an arbitrary rotating-frame operator $\tilde{O}$ for the i^{th} evolution window is given by

$$O_{\mathrm{T},i} = U_{\mathrm{T},i}\,\tilde{O}\,U_{\mathrm{T},i}^{\dagger}, \tag{A.1}$$

where $U_{\mathrm{T},i}$ and its Hermitian conjugate $U_{\mathrm{T},i}^{\dagger}$ are the unitary propagation operators corresponding to the $\pi/2$ pulses of CLSW-16. Finally, the corresponding average Hamiltonian is

$$\bar{\mathcal{H}}_{O}^{(0)} = t_{\mathrm{c}}^{-1}\sum\nolimits_{i}\tau_{i}\,O_{\mathrm{T},i}\,, \tag{A.2}$$

where τ_i is the duration of the i^{th} window and t_{c} is the duration of the cycle.

The propagators $U_{\mathrm{T},i}$ for the CLSW-16 sequence are listed in Table A.1. The corresponding toggling-frame representations of all operators needed for transformation of Hamiltonians relevant to spin interactions discussed in this thesis are also presented. These include: (1) $\tilde{\mathcal{H}}_{rf}$ of Eq. 1.32, which describes rf excitation used for homogeneous offsetting, (2) $\tilde{\mathcal{H}}_{KS}$ of Eq. (4.14), which governs the optically induced Knight shift interaction, and (3) $\tilde{\mathcal{H}}_{Q,i}$ of Eq. (4.60) and $\tilde{\mathcal{H}}_{Q2}$ of Eq. (5.4), which respectively describe the dc and double-quantum linear quadrupole Stark effect (LQSE) interactions. The operators relevant to the single-quantum LQSE are included for completeness.

Table A.1 CLSW-16 toggling-frame propagators and corresponding operator representations, including the $\{I_x, I_y, I_z\}$ basis and combinations thereof that are relevant to the zero (dc), single (SQ) and double (DQ) quantum LQSE.

window number	Propagator, U_T	basis operators			dc LQSE	SQ rf LQSE		DQ rf LQSE		window duration[(a)]
		I_x	I_y	I_z	I_z^2	$+[I_z, I_x]_{+}$	$+[I_z, I_y]_{+}$	$+[I_x, I_y]_{+}$	$(I_x^2 - I_y^2)$	
0	å	I_x	I_y	I_z	I_z^2	$+[I_z, I_x]_{+}$	$+[I_z, I_y]_{+}$	$+[I_x, I_y]_{+}$	$(I_x^2 - I_y^2)$	τ
1	$e^{i\frac{\pi}{2}I_y}$	$-I_z$	I_y	I_x	I_x^2	$-[I_z, I_x]_{+}$	$+[I_x, I_y]_{+}$	$-[I_z, I_y]_{+}$	$(I_z^2 - I_y^2)$	τ
2	$e^{i\frac{\pi}{2}I_y} e^{-i\frac{\pi}{2}I_x}$	$-I_z$	$-I_x$	I_y	I_y^2	$-[I_z, I_y]_{+}$	$-[I_x, I_y]_{+}$	$+[I_z, I_x]_{+}$	$(I_z^2 - I_x^2)$	2τ
3	$e^{i\frac{\pi}{2}I_y} e^{-i\pi I_x}$	$-I_z$	$-I_y$	$-I_x$	I_x^2	$+[I_z, I_x]_{+}$	$+[I_x, I_y]_{+}$	$+[I_z, I_y]_{+}$	$(I_z^2 - I_y^2)$	τ
4	$e^{i\frac{\pi}{2}I_y} e^{-i\pi I_x} e^{i\frac{\pi}{2}I_y}$	I_x	$-I_y$	$-I_z$	I_z^2	$-[I_z, I_x]_{+}$	$+[I_z, I_y]_{+}$	$-[I_x, I_y]_{+}$	$(I_x^2 - I_y^2)$	2τ
5	$e^{i\frac{\pi}{2}I_y} e^{-i\pi I_x} e^{i\pi I_y}$	I_z	$-I_y$	I_x	I_x^2	$+[I_z, I_x]_{+}$	$-[I_x, I_y]_{+}$	$-[I_z, I_y]_{+}$	$(I_z^2 - I_y^2)$	τ
6	$e^{i\frac{\pi}{2}I_y} e^{-i\pi I_x} e^{i\pi I_y} e^{-i\frac{\pi}{2}I_x}$	I_z	$-I_x$	$-I_y$	I_y^2	$-[I_z, I_y]_{+}$	$+[I_x, I_y]_{+}$	$-[I_z, I_x]_{+}$	$(I_z^2 - I_x^2)$	2τ
7	$e^{i\frac{\pi}{2}I_y} e^{-i\pi I_x} e^{i\pi I_y} e^{-i\pi I_x}$	I_z	I_y	$-I_x$	I_x^2	$-[I_z, I_x]_{+}$	$-[I_x, I_y]_{+}$	$+[I_z, I_y]_{+}$	$(I_z^2 - I_y^2)$	τ
8	$e^{i\frac{\pi}{2}I_y} e^{-i\pi I_x} e^{i\pi I_y} e^{-i\pi I_x} e^{i\frac{\pi}{2}I_y}$	I_x	I_y	I_z	I_z^2	$+[I_z, I_x]_{+}$	$+[I_z, I_y]_{+}$	$+[I_x, I_y]_{+}$	$(I_x^2 - I_y^2)$	2τ
9	$e^{i\frac{\pi}{2}I_y} e^{-i\pi I_x} e^{i\pi I_y} e^{-i\pi I_x}$	I_z	I_y	$-I_x$	I_x^2	$-[I_z, I_x]_{+}$	$-[I_x, I_y]_{+}$	$+[I_z, I_y]_{+}$	$(I_z^2 - I_y^2)$	τ
10	$e^{i\frac{\pi}{2}I_y} e^{-i\pi I_x} e^{i\pi I_y} e^{-i\frac{\pi}{2}I_x}$	I_z	$-I_x$	$-I_y$	I_y^2	$-[I_z, I_y]_{+}$	$+[I_x, I_y]_{+}$	$-[I_z, I_x]_{+}$	$(I_z^2 - I_x^2)$	2τ
11	$e^{i\frac{\pi}{2}I_y} e^{-i\pi I_x} e^{i\pi I_y}$	I_z	$-I_y$	I_x	I_x^2	$+[I_z, I_x]_{+}$	$-[I_x, I_y]_{+}$	$-[I_z, I_y]_{+}$	$(I_z^2 - I_y^2)$	τ
12	$e^{i\frac{\pi}{2}I_y} e^{-i\pi I_x} e^{i\frac{\pi}{2}I_y}$	I_x	$-I_y$	$-I_z$	I_z^2	$-[I_z, I_x]_{+}$	$+[I_z, I_y]_{+}$	$-[I_x, I_y]_{+}$	$(I_x^2 - I_y^2)$	2τ
13	$e^{i\frac{\pi}{2}I_y} e^{-i\pi I_x}$	$-I_z$	$-I_y$	$-I_x$	I_x^2	$+[I_z, I_x]_{+}$	$+[I_x, I_y]_{+}$	$+[I_z, I_y]_{+}$	$(I_z^2 - I_y^2)$	τ
14	$e^{i\frac{\pi}{2}I_y} e^{-i\frac{\pi}{2}I_x}$	$-I_z$	$-I_x$	I_y	I_y^2	$-[I_z, I_y]_{+}$	$-[I_x, I_y]_{+}$	$+[I_z, I_x]_{+}$	$(I_z^2 - I_x^2)$	2τ
15	$e^{i\frac{\pi}{2}I_y}$	$-I_z$	I_y	I_x	I_x^2	$-[I_z, I_x]_{+}$	$+[I_x, I_y]_{+}$	$-[I_z, I_y]_{+}$	$(I_z^2 - I_y^2)$	τ
16	å	I_x	I_y	I_z	I_z^2	$+[I_z, I_x]_{+}$	$+[I_z, I_y]_{+}$	$[I_x, I_y]_{+}$	$(I_x^2 - I_y^2)$	τ

[(a)] Window durations for the sequence are given in the δ-pulse approximation, whereas their actual duration is the noted value minus the $\pi/2$ pulse duration t_p.

Appendix B. The Linear Quadrupole Stark Effect

A. Electric-Field-Induced Quadrupole Interactions

The linear quadrupole Stark effect (LQSE) is a crystalline or molecular system's linear response to an electric field observed as the quadrupole interaction on nuclei with spin $I > \frac{1}{2}$ at a site lacking inversion symmetry. The nuclear quadrupole interaction exists between the charge distribution $\rho_n(\mathbf{r})$ of a nucleus and an electric potential $V(\mathbf{r})$ arising from fields of other nuclei, the sample's electron distribution, or an applied electric field. When $V(\mathbf{r})$ is expanded in a Taylor series about the nuclear position ($\mathbf{r} = 0$), the overall energy of this interaction is given by the integral over the nuclear volume,[102]

$$E_{\rho,V} = V(0)\int \rho_n(\mathbf{r})\, d^3\mathbf{r} + \sum_i V_i \int x_i \rho_n(\mathbf{r})\, d^3\mathbf{r} + \sum_{i,j} \tfrac{1}{2} V_{ij} \int x_i x_j \rho_n(\mathbf{r})\, d^3\mathbf{r} + \ldots . \tag{B.1}$$

The Cartesian position coordinates x_i and x_j, where i and j range over 1, 2 and 3, are arbitrary and the coefficients of the expansion are the derivatives

$$V_i = \left.\frac{\partial V}{\partial x_i}\right|_{r=0} \quad \text{and} \quad V_{ij} = \left.\frac{\partial V}{\partial x_i\, \partial x_j}\right|_{r=0} . \tag{B.2}$$

Since the first term in Eq. (B.1) is independent of nuclear orientation, it has no bearing on the NMR Hamiltonian, while the second vanishes by the inversion symmetry of the nucleus. The third term describes the energy of the nuclear quadrupole interaction, which is of interest here.

When an electric field **E** is applied to the sample, the components V_{ij} of the electric-field-gradient tensor may be expanded as a Taylor expansion about | **E** | = E = 0:

$$V_{ij} = (V_{ij})_{E=0} + \sum_k C_{ij,k} E_k + \ldots , \tag{B.3}$$

where the first term gives a component of the intrinsic electric-field-gradient tensor and the second describes the LQSE relating the V_{ij} to **E** via the third-rank tensor **C** with components

$$C_{ij,k} = \left(\frac{\partial V_{ij}}{\partial E_k} \right)_{E=0} . \tag{B.4}$$

Both the matrix of $(V_{ij})_{E=0}$ and the **C** tensor describe properties of the crystalline or molecular sample and, therefore, must be invariant under symmetry transformations within the point group of that system. In the case of bulk GaAs and the other III-Vs with zincblende symmetry, the crystal lattice belongs to the T_d point group, which, along with the equivalence of the coordinates, indicates that all components of $(V_{ij})_{E=0}$ must vanish, that $C_{ij,k} \neq 0$ only for $i \neq j \neq k$, and that these non-zero components are equivalent.[104]

The **C** tensor itself may be broken up into two contributing factors:

$$C_{ij,k} = R_{ij,k} + \sum_{mn} S_{ij,mn} d_{mn,k} , \tag{B.5}$$

where the coupling of the fourth-rank strain tensor **S** and third-rank piezoelectric tensor **d** describes the induced electric-field-gradient due to a relative shift of the Ga and As sublattices with **E**, and the third-rank tensor **R** describes the polarization-induced distortion of covalent electronic states in the crystal lattice. It has been shown[60,61,104] that the polarization of covalent electronic states is the dominant mechanism underlying the LQSE in GaAs, and some literature explicitly drops notation of the **S** tensor

contribution by equating **C** to **R**. However, the LQSE experimentally includes both terms.

Finally, we complete the form of the electric-field-gradient tensor, making the particular choice of associating $k = 1$, 2 and 3 with the [100], [010] and [001] crystal axes, respectively, using the Voigt notation (i.e., 11 = 1, 22 = 2, 33 = 3, 23 = 4, 13 = 5 and 12 = 6) to collapse the j and k indices of **C** into a single index and recalling that $C_{14} = C_{25} = C_{36}$. Thus, according to Eq. (B.3) and the GaAs lattice symmetry, the components of the induced electric-field-gradient tensor are

$$V_{ii} = 0 \quad \text{and} \quad V_{ij} = V_{ji} = C_{14} E_k \tag{B.6}$$

for i, j and k a permutation of the three axes.

B. The Nuclear Quadrupole Hamiltonian

In order to understand and manipulate the role of the LQSE in NMR evolution, we now review the general form of the spin Hamiltonian $\mathcal{H}_Q$ corresponding to the nuclear quadrupole interaction in terms of the spherical tensor basis of operators $T_{k,q}$ with the convention[33]

$$T_{2,0} = \tfrac{1}{\sqrt{6}}(3I_z^2 - I(I+1)), \tag{B.7}$$

$$T_{2,\pm1} = \mp\tfrac{1}{2}(I_z I_\pm + I_\pm I_z) \tag{B.8}$$

and

$$T_{2,\pm2} = \tfrac{1}{2} I_\pm^2 . \tag{B.9}$$

Here I_x, I_y and I_z are the components of the dimensionless nuclear spin angular momentum operator and $I_\pm = I_x \pm i\, I_y$. The spherical tensor coefficients that correspond to the $T_{k,q}$ are

$$V_{2,0} = \tfrac{3}{\sqrt{6}} V_{zz} = 0, \tag{B.10}$$

$$V_{2,\pm 1} = \mp (V_{zx} \pm i V_{zy}) = -iC_{14}(E_1 \mp iE_2) \tag{B.11}$$

and

$$V_{2,\pm 2} = \tfrac{1}{2}(V_{xx} - V_{yy}) \pm iV_{xy} = \pm iC_{14}E_3, \tag{B.12}$$

where the rightmost equivalence in each of Eqs. (B.10)-(B.12) follows from Eq. (B.6). To write $\mathcal{H}_Q$ in its most general form, we allow for arbitrary reorientation of the static magnetic field $\mathbf{B}_0$ from [001] in three successive rotations by the angles γ, β and α about the crystal-fixed [001], [010] and [001] axes, respectively. This rotation is represented by the transformation

$$V'_{2,q}(\alpha,\beta,\gamma) = \sum_{p=-2}^{+2} V_{2,p} e^{-i(\alpha p + \gamma q)} d^2_{pq}(\beta), \tag{B.13}$$

of the coefficients of Eqs. (B.10)-(B.12), where the $d^2_{pq}(\beta)$ are reduced Wigner rotation matrix elements.[33,107] These spatial and spin tensor elements are inserted into the general form of the nuclear quadrupole spin Hamiltonian[33]

$$\mathcal{H}_Q(\alpha,\beta,\gamma) = \frac{eQ}{2I(2I-1)\hbar} \sum_{q=-2}^{+2} (-1)^q \, V'_{2,q} \, T_{2,-q} \tag{B.14}$$

where Q is the nuclear quadrupole moment, e is the unit of electron charge, $\hbar$ is Planck's constant divided by 2π, and the expression is in units of (radÿs^{-1}). Literature values of Q for each nuclear isotope in GaAs are listed in Table 3.1, along with the measured values of C_{14} for the Ga and As sublattices in bulk GaAs.[62]

Table B.1 The reduced Wigner rotation matrices, $d^2_{pq}(\beta)$, relevant to transformation of $\mathcal{H}_Q$ with reorientation of $\mathbf{B}_0$ with respect to the GaAs crystal axes as discussed in the text.[33,107]

$d^2_{22}(\beta) = d^2_{-2-2}(\beta)$	$\cos^4\frac{\beta}{2}$
$d^2_{21} = -d^2_{12} = -d^2_{-2-1} = d^2_{-1-2}$	$-\frac{1}{2}(\sin\beta)(1+\cos\beta)$
$d^2_{20} = d^2_{02} = d^2_{-20} = d^2_{0-2}$	$\sqrt{\frac{3}{8}}\sin^2\beta$
$d^2_{2-1} = d^2_{1-2} = -d^2_{-21} = -d^2_{-12}$	$\frac{1}{2}(\sin\beta)(\cos\beta-1)$
$d^2_{2-2} = d^2_{-22}$	$\sin^4\frac{\beta}{2}$
$d^2_{11} = d^2_{-1-1}$	$\frac{1}{2}(2\cos\beta-1)(\cos\beta+1)$
$d^2_{1-1} = d^2_{-11}$	$\frac{1}{2}(2\cos\beta+1)(1-\cos\beta)$
$d^2_{10} = d^2_{0-1} = -d^2_{01} = -d^2_{-10}$	$-\sqrt{\frac{3}{2}}(\sin\beta)(\cos\beta)$
d^2_{00}	$\frac{1}{2}(3\cos^2\beta-1)$

The influence of $\mathcal{H}_Q$ on NMR evolution is best evaluated in the rotating frame defined by the phase ϕ_{rf} and angular frequency ω of the applied rf magnetic field in a pulsed NMR experiment, where, in practice, $\omega = \omega_0$, the nuclear Larmor frequency. The direction of $\mathbf{B}_0$ defines the z-axis. To enter the rotating frame, we transform the $T_{2,q}$ operators according to

$$\tilde{T}_{2,q}(t) = U_{rf}(t)\ T_{2,q}\ U^{\dagger}_{rf}(t)\,, \tag{B.15}$$

where

$$U_{rf}(t) = \exp[i(\omega_0 t + \phi_{rf})I_z] \tag{B.16}$$

and its Hermitian conjugate $U^{\dagger}_{rf}(t)$ are the unitary operators appropriate to this transformation. It is straightforward to show that

$$U_{rf}(t)\ I_{\pm}^{\,q}\ U^{\dagger}_{rf}(t) = \exp[\pm i\ q(\omega_0 t + \phi_{rf})]\ I_{\pm}^{\,q}\,, \tag{B.17}$$

while I_z commutes with $U_{rf}(t)$. Thus, according to Eqs. (B.7) – (B.9), and (B.14) – (B.17), the rotating-frame quadrupole Hamiltonian is

$$\tilde{\mathcal{H}}_Q(\alpha,\beta,\gamma) = \frac{eQ}{2I(2I-1)\hbar} \sum_{q=-2}^{+2} (-1)^q \; V'_{2,q} \; T_{2,-q} \; \exp[-i\, q(\omega_0 t + \phi_{rf})] \; . \qquad \text{(B.18)}$$

Only the term proportional to $T_{2,0}$ in Eq. (B.18) is stationary in the rotating frame, while effects of the oscillating terms on the spin system average to zero over time and are thus normally truncated to obtain the first-order form of $\tilde{\mathcal{H}}_Q$. The $T_{2,0}$ term gives rise to the dc LQSE. Inserting Eqs. (B.10) – (B.12) for the $V_{2,p}$ and the $d^2_{p,0}(\beta)$ values in Table 3.1 into Eq. (B.13), we find

$$V'_{2,0}(\alpha,\beta,\gamma) = \sqrt{\tfrac{3}{2}}\; C_{14} \left[\sin 2\beta \; (E_{100} \sin\alpha + E_{010} \cos\alpha) + E_{001} \sin^2\beta \; \sin 2\alpha \right], \quad \text{(B.19)}$$

which, inserted into Eq. (B.18), yields the dependence of the secular LQSE on the orientation of the magnetic field and the components of the electric field in the crystal frame. This is needed, for example, to describe the influence of the heterojunction interfacial field on the NMR line shape, as discussed in Chapter 3, as well as the optically induced POWER LQSE experiments of Chapter 4. For the case where $E_{100} = E_{010} = E_{001}$, Eq. (B.19) reduces to a particular case previously presented in the context of macroscopic dc E-fields.[60,61]

The normally truncated terms of $\tilde{\mathcal{H}}_Q$ are the terms of interest for extending POWER NMR to include the conversion of nonsecular terms into diagonal, secular observables, as in Chapter 5. Inserting Eqs. (B.8) – (B.12) for the $T_{2,\pm1}$, $T_{2,\pm2}$ and $V_{2,p}$, and the $d^2_{p,\pm1}(\beta)$ and $d^2_{p,\pm2}(\beta)$ values in Table 3.1 into Eq. (B.13), we obtain

$$\begin{aligned} V'_{2,\pm1}(\alpha,\beta,\gamma) \; = \; \mp C_{14} e^{\mp i\gamma} \big[& E_{100}(\cos 2\beta \; \sin\alpha \; \pm \; i \cos\beta \; \cos\alpha) \\ & + E_{010}(\cos 2\beta \; \cos\alpha \; \mp \; i \cos\beta \; \sin\alpha) \\ & + E_{001}(\tfrac{1}{2}\sin 2\beta \; \sin 2\alpha \; \pm \; i \sin\beta \; \cos 2\alpha) \big], \end{aligned} \qquad \text{(B.20)}$$

and

$$
\begin{aligned}
V'_{2,\pm 2}(\alpha,\beta,\gamma) \;=\; & \tfrac{1}{2} C_{14} e^{\mp 2i\gamma}\big[E_{100}(-\sin 2\beta\ \sin\alpha \mp 2i\ \sin\beta\ \cos\alpha) \\
& + E_{010}(-\sin 2\beta\ \cos\alpha \pm 2i\ \sin\beta\ \sin\alpha) \\
& + E_{001}(\ (\cos^2\beta + 1)\ \sin 2\alpha \pm 2i\ \cos\beta\ \cos 2\alpha)\big].
\end{aligned}
\tag{B.21}
$$

Appendix C. The Empirical Radial Weighting Function

In this appendix, the mathematical formalism for obtaining an empirical function for weighting nuclear site-by-site contributions to an optically detected NMR signal is developed. This procedure may be used to convert a Knight-shift-distribution spectrum at a given ONP time into an empirical replacement for $A(t_{ONP}, r)$ of Eq. (4.37). The present derivation is general in that the form of the wave function $\Psi(\mathbf{r})$ describing the electronic state that is responsible for the Knight shift is left unspecified. The input required to generate an empirical weighting function consists of the Knight-shift distribution spectrum, the underlying linewidth of individual contributions to that spectrum, $|\Psi(\mathbf{r})|^2$ and the corresponding average electronic spin $\langle S \rangle$. Therefore, while my interest for this thesis is primarily in application to a radial electronic state (see Sections C and D of Chapter 4), this novel weighting scheme is equally applicable to calculation of ONMR signals that derive from interaction of nuclei with electronic spins in a variety of quantum-confined systems, including quantum wells and dots.

The derivation begins with a general expression for the time-domain ONMR signal in t_1:

$$S(t_1) = \int d^3\mathbf{r} \left(\sum_j \delta(\mathbf{r} - \mathbf{r}_j)\, A(\mathbf{r})\, \cos\left(\omega(\mathbf{r})\, t_1\right) e^{-\Delta\nu(\mathbf{r})\, t_1} \right), \tag{C.1}$$

where

$$\omega(\mathbf{r}) = \omega_{hf}\, |\Psi(\mathbf{r})|^2 \tag{C.2}$$

is the position-dependent angular frequency of the Knight-shift, ω_{hf} is the magnitude of the hyperfine Hamiltonian at the maximum of $|\Psi(\mathbf{r})|^2$, and $\Delta\nu(\mathbf{r})$ is the FWHM of the

(presumably) Lorentzian contribution of a nucleus at **r** to the corresponding frequency domain spectrum. The signal in Eq. (C.2) is a summation of contributions from nuclear sites located at positions $\mathbf{r}_j$, while $\delta(\mathbf{r}-\mathbf{r}_j)$ is a Dirac delta function.

If the linewidth $\Delta\nu(\mathbf{r})$ is spatially uniform[C(a)] then it may be deconvoluted from the time-domain spectrum by multiplication of Eq. (C.1) by $e^{+\pi\Delta\nu t_1}$, to yield

$$S_d(t_1) = \int d^3\mathbf{r} \left(\sum_j \delta(\mathbf{r}-\mathbf{r}_j)\ A(\mathbf{r}) \cos(\omega(\mathbf{r})t_1) \right). \tag{C.3}$$

The Fourier transform of this linewidth-deconvoluted signal is

$$\tilde{S}_d(\omega_1) = \int d^3\mathbf{r} \left[\sum_j \delta(\mathbf{r}-\mathbf{r}_j)\ A(\mathbf{r}) \cos(\omega(\mathbf{r})t_1) \times (2\pi)^{-1/2} \int_{-\infty}^{\infty} dt_1 \left(e^{+i\omega_1 t_1} \cos(\omega(\mathbf{r})t_1) \right) \right], \tag{C.4}$$

which is equivalently written as

$$\tilde{S}_d(\omega_1) = \sqrt{\tfrac{\pi}{2}} \int d^3\mathbf{r} \left[\sum_j \delta(\mathbf{r}-\mathbf{r}_j)\ A(\mathbf{r}) \times (2\pi)^{-1} \int_{-\infty}^{\infty} dt_1 \left(e^{-i(\omega(\mathbf{r})-\omega_1)t_1} + e^{-i(-\omega(\mathbf{r})-\omega_1)t_1} \right) \right]. \tag{C.5}$$

In this expression, we recognize the Fourier transform representation[108]

$$\delta(\omega(\mathbf{r}) \pm \omega_1) = (2\pi)^{-1} \int_{-\infty}^{\infty} dt_1\ e^{-i(\pm\omega(\mathbf{r})-\omega_1)t_1} \tag{C.6}$$

of a delta function in angular frequency space, which, upon substitution into Eq. (C.5), yields

---

C(a) Conditions under which the line width may not be spatially uniform are described in footnote 1(b) (Section C.2 of Chapter 1).

$$\tilde{S}_d(\omega_1) = \sqrt{\tfrac{\pi}{2}} \int d^3\mathbf{r} \left[\sum_j A(\mathbf{r})\, \delta\left(\mathbf{r}-\mathbf{r}_j\right) \left(\delta\left(\omega(\mathbf{r})-\omega_1\right) + \delta\left(\omega(\mathbf{r})+\omega_1\right)\right)\right]. \quad \text{(C.7)}$$

A more convenient expression of $\tilde{S}_d(\omega_1)$ is in terms of the frequency $\nu_1 = (2\pi)^{-1}\omega_1$ and the frequencies ν_{hf} and $\nu(\mathbf{r})$ with angular counterparts ω_{hf} and $\omega(\mathbf{r})$. Substituting the relationship[108]

$$\delta\left(2\pi\left(\nu(\mathbf{r})\pm\nu_1\right)\right) = \tfrac{1}{2\pi}\,\delta\left(\nu(\mathbf{r})\pm\nu_1\right) \quad \text{(C.8)}$$

for $\delta\left(\omega(\mathbf{r})\pm\omega_1\right)$ in Eq. (C.7), we obtain

$$\tilde{S}_d(\nu_1) = \left(8\pi\right)^{-1/2} \int d^3\mathbf{r} \left[\sum_j A(\mathbf{r})\, \delta\left(\mathbf{r}-\mathbf{r}_j\right) \left(\delta\left(\nu(\mathbf{r})-\nu_1\right) + \delta\left(\nu(\mathbf{r})+\nu_1\right)\right)\right]. \quad \text{(C.9)}$$

The apparent contribution of two frequencies $\pm\nu_1$ in this result is an artifact of Fourier transformation of the non-quadrature signal of Eqs. (C.1) and (C.3), thus one of the δ-functions in Eq. (C.9) is subsequently dropped as a non-contributor to the ONMR signal. Furthermore, justification of this exclusion is also reasoned physically using the fact that a Knight shift due to interaction with a single sort of electronic state, while differing in magnitude among the ensemble of nuclear spins, does not vary in sign.

In most cases, the spatial dependencies of $\nu(\mathbf{r})$ and $A(\mathbf{r})$ in Eq. (C.9) are determined by a single scalar variable. For example, ONMR signals related to the system investigated throughout Chapter 4, wherein the electrons responsible for the Knight shift are trapped on point defects and characterized by a radial envelope $\psi(r)$, are determined by $\nu(r)$ and $A(r)$ of Eqs. (4.16) and (4.37). Similarly, in the case that such electrons are confined to a quantum well that has an isotropic in-plane distribution of carriers, the envelope $\psi(z)$ is appropriate and we have $\{\nu(\mathbf{r}), A(\mathbf{r})\} \rightarrow \{\nu(z), A(z)\}$. With these

important examples in mind, we now reduce spatial dependence of the ONMR signal such that it is given by an arbitrary scalar variable ξ. In this reduction, we make use of the relationships[109]

$$\delta(\mathbf{r}-\mathbf{r}_j) = \left|J(\mathbf{r},\underset{\sim}{\xi})\right|^{-1} \delta(\xi-\xi_j)\,\delta(\xi'-\xi'_j)\,\delta(\xi''-\xi''_j) \tag{C.10}$$

and

$$d^3\mathbf{r} = J(\mathbf{r},\underset{\sim}{\xi})\,d\xi\,d\xi'\,d\xi'', \tag{C.11}$$

where $J(\mathbf{r},\underset{\sim}{\xi})$ is the Jacobian that relates integration over spherical coordinates **r** to that over the arbitrary coordinates $\underset{\sim}{\xi} = (\xi,\xi',\xi'')$. Inserting Eqs. (C.10) and (C.11) into Eq. (C.9), assuming a positive Jacobian and replacing $A(\mathbf{r})$ and $\nu(\mathbf{r})$ with $A(\xi)$ and $\nu(\xi)$, we obtain

$$\begin{aligned}\tilde{S}_d(\nu_1) = (8\pi)^{-1/2} &\iiint d\xi\,d\xi'\,d\xi'' \\ &\left[\sum_j \delta(\xi-\xi_j)\,\delta(\xi'-\xi'_j)\,\delta(\xi''-\xi''_j)\,A(\xi)\,\delta(\nu(\xi)-\nu_1)\right],\end{aligned} \tag{C.12}$$

which, using the δ-function normalization property, becomes

$$\tilde{S}_d(\nu_1) = (8\pi)^{-1/2} \int d\xi \left[\sum_j \delta(\xi-\xi_j)\,A(\xi)\,\delta(\nu(\xi)-\nu_1)\right]. \tag{C.13}$$

It proves useful to define the function

$$g(\xi) = \nu(\xi) - \nu_1, \tag{C.14}$$

and exploit the relationship[108]

$$\delta(g(\xi)) = \sum_k \left|g'(\xi_k)\right|^{-1} \delta(\xi-\xi_k), \tag{C.15}$$

where the summation is over all values of $\xi = \xi_k$ at which $g(\xi_k) = 0$ and

$$g'(\xi_k) = \left[\frac{d\nu(\xi)}{d\xi}\right]_{\xi=\xi_k} \neq 0. \tag{C.16}$$

The interest here is in the case where a one-to-one relationship exists between ξ and ν, and thus, considering Eq. (C.14), the only term that contributes in Eq. (C.15) is that where $\xi_k = \xi(\nu_1)$. Inserting Eqs. (C.14) and (C.16) into Eq. (C.15) yields

$$\delta(\nu(\xi)-\nu_1) = \left|\left(\frac{d\nu(\xi)}{d\xi}\right)_{\xi=\xi(\nu_1)}\right|^{-1} \delta(\xi-\xi(\nu_1)), \tag{C.17}$$

which we in turn insert into Eq. (C.13), to obtain

$$\tilde{S}_d(\nu_1) = (8\pi)^{-1/2} \int d\xi \left[\sum_j \delta(\xi-\xi_j)\,\delta(\xi-\xi(\nu_1))\,A(\xi)\left|\left(\frac{d\nu(\xi)}{d\xi}\right)_{\xi=\xi(\nu_1)}\right|^{-1}\right]. \tag{C.18}$$

Executing the integration, we have

$$\tilde{S}_d(\nu_1) = (8\pi)^{-1/2} \sum_j{}' \left(A(\xi(\nu_1))\left|\left(\frac{d\nu(\xi)}{d\xi}\right)_{\xi=\xi(\nu_1)}\right|^{-1}\right), \tag{C.19}$$

where the sum has been primed to indicate that it is to be carried out only over those sites where $\xi = \xi(\nu_1)$. Furthermore, since there are no indexed factors on the right-hand side of Eq. (C.19), we recognize that the summation merely amounts to counting the number $N_1(\,\xi(\nu_1)\,)$ of sites for which $\xi = \xi(\nu_1)$. Therefore, the desired expression for the single-spin time-domain weighting function is

$$A(\xi(\nu_1)) = (8\pi)^{-1/2}\left[N_1(\xi(\nu_1))\right]^{-1}\left|\left(\frac{d\nu(\xi)}{d\xi}\right)_{\xi=\xi(\nu_1)}\right|\tilde{S}_d(\nu_1). \tag{C.20}$$

Determination of $N_1(\,\xi(\nu_1)\,)$ is specific to the system studied. In the case of a radial electronic state, where $\xi \to r$, the number of spins in an onion skin of infinitesimal thickness dr is

$$N_1(r) = 4\pi\,\Omega^{-1}\,r^2\,dr, \tag{C.21}$$

where Ω is the volume of the appropriate unit cell. In the case of a quantum well with an isotropic in-plane carrier distribution and uniform width, the relevant dimension is the growth direction z and N_1 is spatially uniform.

Appendix D. Perturbation-Theory Derivation of the QW Polarization Response

The QW is modeled as an infinite one-dimensional potential well, centered about $z = 0$, where z is position along the growth direction. The quantum-confined eigenstates $\psi_n(z)$ of the symmetric well can be categorized into even ($n = j$) and odd ($n = k$) states given by

$$\psi_j(z) = a^{-1/2}\cos(\tfrac{j\pi z}{2a}) \tag{D.1}$$

and

$$\psi_k(z) = a^{-1/2}\sin(\tfrac{k\pi z}{2a}), \tag{D.2}$$

where $j = 1, 3, 5, \ldots$, $k = 2, 4, 6, \ldots$, and $2a$ is the width of the QW. The energy of the n^{th} state is

$$E_n = \frac{n^2\pi^2\hbar^2}{8m^*a^2}. \tag{D.3}$$

An E field applied across the QW introduces a linear term in the potential well ($\Phi(z) = \Phi_0\frac{1}{2a}(z+a)$ from $z = -a$ to $z = a$), which is treated as a small perturbation to the symmetric box Hamiltonian.

The first-order perturbation-theory correction to the wave function describing the ground state is

$$\psi_1^{(1)}(z) = \sum_{n>1}\left[\frac{\left\langle\psi_n^{(0)}\right|\left(\Phi_0\tfrac{z}{2a}\right)\left|\psi_1^{(0)}\right\rangle}{E_1^{(0)} - E_n^{(0)}}\ \psi_n^{(0)}(z)\right], \tag{D.4}$$

where the superscripts (i) indicate i^{th}-order perturbation corrections to the wave function and energy solutions of the Schrödinger equation. By symmetry, only the states $\psi_k^{(0)}(z)$

of odd parity will contribute to the first-order correction of the even ground-state wave function. Inserting the expression for $\psi_k^{(0)}(z)$ from Eq. (D.2) and the corresponding energy given by Eq. (D.3) into Eq. (D.4) yields

$$\psi_1^{(1)}(z) = \frac{2^6 m^* a^{3/2} \Phi_0}{\hbar^2 \pi^4} \sum_k \left[\frac{(-1)^{k/2} k}{(k^2-1)^3} \sin(\tfrac{k\pi z}{2a}) \right]. \tag{D.5}$$

The term contributing at $k = 4$ is only 1.6% of the magnitude of the term at $k = 2$. Truncating the above series at $k = 2$ yields

$$\psi_1^{(1)}(z) = \frac{-2^7 m^* a^{3/2} \Phi_0}{27 \hbar^2 \pi^4} \sin(\tfrac{\pi z}{a}). \tag{D.6}$$

The sufficiency of the first-order perturbation-theory treatment of this problem is validated by derivation of the expression for the second-order correction to the ground-state wave function, which is

$$\psi_1^{(2)}(z) = -\left(\frac{\Phi_0}{2a}\right)^2 \sum_{n>1} \sum_{l>1} \left[\frac{\left\langle \psi_l^{(0)} \middle| z \middle| \psi_1^{(0)} \right\rangle \left\langle \psi_n^{(0)} \middle| z \middle| \psi_l^{(0)} \right\rangle}{(E_1^{(0)} - E_l^{(0)})\,(E_1^{(0)} - E_n^{(0)})} \psi_n^{(0)}(z) \right]. \tag{D.7}$$

Substituting the explicit forms of the zero-order wave function and energy expressions into Eq. (D.7), and then taking parity considerations ($n = j$ with $j > 1$ only, and $l = k$ only) into account, provides the expression

$$\psi_1^{(2)}(z) = \frac{-2^{12} a^{7/2} (m^* \Phi_0)^2}{\hbar^4 \pi^8} \times \sum_{j>1} \sum_k \left[\frac{(-1)^{(j-1)/2}\, j\, k^2}{(k^2-1)^3\,(j^2-1)\,(j^2-k^2)^2} \cos(\tfrac{j\pi z}{2a}) \right]. \tag{D.8}$$

The size of the second-order correction to the ground-state wave function can be calculated neglecting terms other than that with $(j, k) = (3, 2)$, which is more than 30

times greater than the magnitude of the second-largest term in Eq. (D.8). This approximation yields

$$\psi_1^{(2)}(z) = \left(\frac{2^6 m^* a^2 \Phi_0}{\hbar^2 \pi^4}\right)^2 \frac{a^{-1/2}}{450} \cos(\tfrac{3\pi z}{2a}). \tag{D.9}$$

The relative size of the coefficients of the second-order correction of Eq. (D.9) to those of the first-order correction of Eq. (D.6) is

$$\frac{48 m^* a^2 \Phi_0}{25 \hbar^2 \pi^4} = (1.62\times10^{36}\ \mathrm{J^{-1}\cdot m^{-2}})\, a^2 \Phi_0 m_0 / m^* \tag{D.10}$$

where m_0 is the electron rest mass. The three parameters determining the validity of the first-order perturbation-theory treatment are Φ_0, a, and (m^*/m_0). In the case of a 10 nm GaAs QW, where $(m^*/m_0) = 0.067$, the relative size given in Eq. (D.10) is $\sim (2.7\times10^{20}\ \mathrm{J^{-1}} \times \Phi_0)$, which limits Φ_0 to be less than 1.8×10^{-20} J if the second-order term is to be < 5% of the first-order correction. This limit corresponds to an applied E field of ~115 kV/cm, which is well above the magnitude of the E field to be applied to the sample using the method we present; thus, the first-order perturbation-theory treatment is sufficient.

The normalized form of the QW ground-state wave function is then

$$\psi_1(z) = \left(1+(a\,c_0)^2\right)^{-1/2}\left(a^{-1/2}\cos(\tfrac{\pi z}{2a}) - a^{1/2}c_0 \sin(\tfrac{\pi z}{a})\right), \tag{D.11}$$

where c_0 is given by Eq. (5.10) and $a^2 c_0^2 \approx (4.5\times10^{37}\ \mathrm{J^{-2}} \times \Phi_0^2)$. Even in the case where the maximum, first-order-perturbation-theory-limited field of 115 kV/cm is applied to the QW sample, $(a\,c_0)^2 \ll 1$, and so the normalization coefficient in Eq. (D.11) is set to unity.

Bibliography

[1] Resonance Absorption by Nuclear Magnetic Moments in a Solid
E.M. Purcell, H.C. Torrey, and R.V. Pound, *Phys. Rev.* **69**, 37 (1946).

[2] Nuclear Induction
F. Bloch, W.W. Hansen, and M. Packard, *Phys. Rev.* **70**, 474 (1946).

[3] Nuclear Dynamic Polarization by Optical Electronic Saturation and Optical Pumping in Semiconductors
G. Lampel, *Phys. Rev. Lett.* **20** (10), 491 (1968).

[4] *Optical Orientation*
F. Meier and B.P. Zakharchenya, (North-Holland, Amsterdam, 1984).

[5] Optical Electron-Nuclear Resonance in Semiconductors
A.I. Ekimov and V.I. Safarov, *JETP Lett.* **15**, 319 (1972).

[6] Low Field Electron-Nuclear Spin Coupling in Gallium Arsenide Under Optical Pumping Conditions
D. Paget, G. Lampel, B. Sapoval, and V.I. Safarov, *Phys. Rev. B* **15** (12), 5780 (1977).

[7] Optical-Detection of NMR in High-Purity GaAs: Direct Study of the Relaxation of Nuclei Close to Shallow Donors
D. Paget, *Phys. Rev. B* **25** (7), 4444 (1982).

[8] Time-Sequenced Optical Nuclear Magnetic Resonance of Gallium Arsenide
S.K. Buratto, D.N. Shykind, and D.P. Weitekamp, *Phys. Rev. B* **44** (16), 9035 (1991).

[9] Optical Larmor Beat Detection of High-Resolution Nuclear Magnetic Resonance in a Semiconductor Heterostructure
J.A. Marohn, P.J. Carson, J.Y. Hwang, M.A. Miller, D.A. Shykind, and D.P. Weitekamp, *Phys. Rev. Lett.* **75** (7), 1364 (1995).

[10] Spectrally Resolved Overhauser Shifts in Single GaAs/$Al_xGa_{(1-x)}$As Quantum Dots
S.W. Brown, T.A. Kennedy, D. Gammon, and E.S. Snow, *Phys. Rev. B* **54** (24), 17339 (1996).

[11] Nuclear Spectroscopy in Single Quantum Dots - Nanoscopic Raman Scattering and Nuclear Magnetic Resonance
D. Gammon, S.W. Brown, E.S. Snow, T.A. Kennedy, D.S. Katzer, and D. Park, *Science* **277** (5322), 85 (1997).

[12] Optical NMR from Single Quantum Dots
S.W. Brown, T.A. Kennedy, and D. Gammon, *Solid State NMR* **11** (1-2), 49 (1998).

[13] All-Optical Nuclear Magnetic Resonance in Semiconductors
J.M. Kikkawa and D.D. Awschalom, *Science* **287** (5452), 473 (2000).

[14] See for example: K. v. Klitzing, G. Dorda and M. Pepper, New Method for High-accuracy Determination of the Fine-Structure Constant Based on Quantized Hall Resistance, *Phys. Rev. Lett.* **45** (6), 494, 1980; D.C. Tsui, H.L. Stormer and A.C. Gossard, Two-Dimensional Magnetotransport in the Extreme Quantum Limit, *Phys. Rev. Lett.* **48** (22), 1559, 1982; R.B. Laughlin, Anomalous Quantum Hall Effect: An Incompressible Quantum Fluid with Fractionally Charged Excitations, *Phys. Rev. Lett.* **50** (18), 1395, 1983; S.E. Barrett, G. Dabbagh, L.N. Pfeiffer, K.W. West, and R. Tycko, Optically Pumped NMR Evidence For Finite-Size Skyrmions in GaAs Quantum Wells Near Landau Level Filling ν=1, *Phys. Rev. Lett.* **74** (25), 5112, 1995.

[15] Optically Detected Conduction Electron-Spin-Resonance, Overhauser Shift and Nuclear-Magnetic-Resonance in *p*-GaAlAs/GaAs Heterostructures
M. Krapf, G. Denninger, H. Pascher, G. Weimann, and W. Schlapp, *Superlattices and Microstructures* **8** (1), 91 (1990).

[16] Optical Polarization of Nuclei in GaAs/AlGaAs Quantum Well Structures
V.K. Kalevich, V.L. Korenev, and O.M. Fedorova, *JETP Lett.* **52** (6), 349 (1990).

[17] Optically Detected Nuclear Magnetic Resonance of Nuclei in a Quantum Well
G.P. Flinn, R.T. Harley, M.J. Snelling, A.C. Tropper, and T.M. Kerr, *Semicond. Sci. Technol.* **5**, 533 (1990).

[18] Optically Detected Nuclear Magnetic Resonance and Knight-Shift in $Al_xGa_{(1-x)}As$ /GaAs Heterostructures
M. Krapf, G. Denninger, H. Pascher, G. Weimann, and W. Schlapp, *Solid State Commun.* **78** (5), 459 (1991).

[19] Optically Pumped NMR Evidence for Finite-Size Skyrmions in GaAs Quantum Wells near Landau Level Filling $\nu = 1$
S.E. Barrett, G. Dabbagh, L.N. Pfeiffer, K.W. West, and R. Tycko, *Phys. Rev. Lett.* **74** (25), 5112 (1995).

[20] Electronic States in Gallium Arsenide Quantum Wells Probed by Optically Pumped NMR
R. Tycko, S.E. Barrett, G. Dabbagh, L.N. Pfeiffer, and K.W. West, *Science* **268** (5216), 1460 (1995).

[21] Optical NMR from Single GaAs/AlGaAs Quantum-Wells
S.W. Brown, T.A. Kennedy, E.R. Glaser, and D.S. Katzer, *J. Phys. D* **30** (10), 1411 (1997).

[22] Optically Pumped Nuclear Magnetic Resonance Measurements of the Electron Spin Polarization in GaAs Quantum Wells near Landau Level Filling Factor $\nu = 1/3$
P. Khandelwal, N.N. Kuzma, S.E. Barrett, L.N. Pfeiffer, and K.W. West, *Phys. Rev. Lett.* **81** (3), 673 (1998).

[23] Optically Pumped NMR Studies of Electron Spin Polarization and Dynamics: New Contraints on the Composite Fermion Description of $\nu = 1/2$
A.E. Dementyev, N.N. Kuzma, P. Khandelwal, S.E. Barrett, L.N. Pfeiffer, and K.W. West, *Phys. Rev. Lett.* **83** (24), 5074 (1999).

[24] Can Nuclear Magnetic Resonance Resolve Epitaxial Layers?
S.K. Buratto, D.N. Shykind, and D.P. Weitekamp, *J. Vac. Sci. Technol. B* **10** (4), 1740 (1992).

[25] Method for Atomic-Layer-Resolved Measurement of Electric Polarization Fields by Nuclear Magnetic Resonance
J.G. Kempf and D.P. Weitekamp, *J. Vac. Sci. Technol. B* **18** (4), 2255 (2000).

[26] J.G. Kempf, B.M. Lambert, M.A. Miller, and D.P. Weitekamp, (in preparation).

[27] New Photoluminescence Effects of Carrier Confinement at an AlGaAs/GaAs Heterojunction Interface
Y.R. Yuan, M.A.A. Pudensi, G.A. Vawter, and J.L. Merz, *J. Appl. Phys.* **58** (1), 397 (1985).

[28] Radiative Recombination of a 3D-Electron with a 2D-Hole in *p*-type GaAs/(AlGa)As Heterojunctions
W. Ossau, E. Bangert, and G. Weimann, *Solid State Commun.* **64** (5), 711 (1987).

[29] Exciton Dynamics in $GaAs/Ga_{(1-x)}Al_xAs$ Heterojunctions and GaAs Epilayers
J.X. Shen, R. Pittini, Y. Oka, and E. Kurtz, *Phys. Rev. B* **61** (4), 2765 (2000).

[30] Time-Dependent Heterointerfacial Band Bending and Quasi-Two-Dimensional Excitonic Transport in GaAs Structures
G.D. Gilliland, M.S. Petrovic, H.P. Hjalmarson, D.J. Wolford, G.A. Northrop, T.F. Kuech, L.M. Smith, and J.A. Bradley, *Phys. Rev. B* **58** (8), 4728 (1998).

[31] Spin Echoes
E.L. Hahn, *Phys. Rev.* **80** (4), 580 (1950).

[32] *High Resolution NMR in Solids: Selective Averaging*
U. Haeberlen, (Academic Press, New York, 1976).

[33] *Principles of High Resolution NMR in Solids*
M. Mehring, (Springer-Verlag, Berlin, 1983).

[34] *Low-Dimensional Semiconductors: Materials, Physics, Technology, Devices*
M.J. Kelly, (Clarendon Press, Oxford, 1995).

[35] Hole Relaxation and Luminescence Polarization in Doped and Undoped Quantum Wells
T. Uenoyama and L.J. Sham, *Phys. Rev. Lett.* **64**, 3070 (1990).

[36] Spin Relaxation Dynamics in GaAs Quantum Wells: Free Carriers and Excitons
L. Vina, T.C. Damen, J.E. Cunningham, J. Shah, and L.J. Sham, *Superlattices and Microstructures* **12** (3), 379 (1992).

[37] Über Mangetische Beeingflussung der Polarization der Resonanzfluoreszenz
W. Hanle, *Z. Phys.* **30**, 93 (1924).

[38] Optical Orientation of the Coupled Electron-Nuclear Spin System of a Semiconductor
V.G. Fleischer and I.A. Merkulov, in *Optical Orientation*, edited by F. Meier and B.P. Zakharchenya (North-Holland, Amsterdam, 1984), Vol. 8, pp. 173.

[39] Time-Sequenced Optical Nuclear Magnetic Resonance of Gallium Arsenide
S.K. Buratto, Ph.D. Thesis, California Institute of Technology, 1993.

[40] Fourier-Transform Time-Sequenced Optical Nuclear Magnetic Resonance of Gallium Arsenide
S.K. Buratto, J.Y. Hwang, N.D. Kurur, D.N. Shykind, and D.P. Weitekamp, *Bull. Magn. Reson.* **15**, 190 (1993).

[41] NMR of Dilute Sites in GaAs
J.Y. Hwang, Ph.D. Thesis, California Institute of Technology, 1994.

[42] I. Multiple-Pulse Radio-Frequency Gradient Nuclear Magnetic Resonance Imaging of Solids, and II. Optical Nuclear Magnetic Resonance Analysis of Gallium Arsenide Structures
J.A. Marohn, Ph.D. Thesis, California Institute of Technology, 1996.

[43] I. Ultrasensitive Surface NMR Using Parahydrogen Spin Labeling, and II. High-Resolution Optical NMR of Semiconductor Heterostructures Using Larmor Beat Detection
P.J. Carson, Ph.D. Thesis, California Institute of Technology, 1997.

[44] Time-Domain Multiple-Quantum NMR
D.P. Weitekamp, *Adv. Magn. Reson.* **11**, 111 (1983).

[45] Nuclear Magnetic Resonance Spectra from a Crystal Rotated at High Speed
E.R. Andrew, A. Bradbury, and R.G. Eades, *Nature* **182**, 1659 (1958).

[46] Removal of Dipolar Broadening of Nuclear Magnetic Resonance Spectra of Solids by Specimen Rotation
E.R. Andrew, A. Bradbury, and R.G. Eades, *Nature* **183**, 1802 (1959).

[47] Free Induction Decays of Rotating Solids
I. Lowe, *Phys. Rev. Lett.* **2** (7), 285 (1959).

[48] Approach to High-Resolution NMR in Solids
J.S. Waugh, L.M. Huber, and U. Haeberlen, *Phys. Rev. Lett.* **20** (5), 180 (1968).

[49] Coherent Averaging Effects in Magnetic Resonance
U. Haeberlen and J.S. Waugh, *Phys. Rev.* **175**, 453 (1968).

[50] Nutation Sequences for Magnetic Resonance Imaging in Solids
H.M. Cho, C.J. Lee, D.N. Shykind, and D.P. Weitekamp, *Phys. Rev. Lett.* **55** (18), 1923 (1985).

[51] Time-Suspension Multiple-Pulse Sequences: Applications to Solid-State Imaging
D.G. Cory, J.B. Miller, and A.N. Garroway, *J. Magn. Reson.* **90**, 205 (1990).

[52] Quantitative Aspects of Coherent Averaging. Simple Treatment of Resonance Offset Processes in Multiple-Pulse NMR.
A. Pines and J.S. Waugh, *J. Magn. Reson.* **8**, 354 (1972).

[53] Fourier Transform Multiple Quantum Nuclear Magnetic Resonance
G. Drobny, A. Pines, S. Sinton, D.P. Weitekamp, and D. Wemmer, *Symp. Faraday Soc.* **13**, 49 (1979).

[54] Advances in Multiple-Pulse Radio-Frequency Gradient Imaging of Solids
J.A. Marohn, D.N. Shykind, M.H. Werner, and D.P. Weitekamp, in *Review of Progress in Quantitative Nondestructive Evaluation*, edited by D.O. Thomson and D.E. Chimenti (Plenum Publishing, NY, NY, 1993), Vol. 12-A, pp. 687.

[55] *Experimental Low-Temperature Physics*
A. Kent, (American Institute of Physics, New York, 1993).

[56] Theory of Optical Spin Orientation of Electrons and Nuclei in Semiconductors
M.I. Dyakonov and V.I. Perel, in *Optical Orientation*, edited by F. Meier and B.P. Zakharchenya (North-Holland, Amsterdam, 1984), Vol. 8, pp. 11.

[57] Optical Orientation in a System of Electrons and Lattice Nuclei in Semiconductors. Experiment
V.L. Berkovits, A.I. Ekimov, and V.I. Safarov, *Sov. Phys. - JETP* **38** (1), 169 (1974).

[58] Optical Orientation in a System of Electrons and Lattice Nuclei in Semiconductors. Theory
M.I. D'yakonov and V.I. Perel', *Sov. Phys. - JETP* **38** (1), 177 (1974).

[59] Nuclear Magnetic Resonance Saturation and Rotary Saturation in Solids
A.G. Redfield, *Phys. Rev.* **98**, 1787 (1955).

[60] Electric Shifts in Magnetic Resonance
N. Bloembergen, in *Proceedings of the 11th Colloque Ampere Conference on Electric and Magnetic Resonance*, Eindhoven, July 1962, edited by J. Smidt, (North-Holland, Amsterdam, 1963), p. 225.

[61] Linear Stark Splitting of Nuclear Spin Levels in GaAs
D. Gill and N. Bloembergen, *Phys. Rev.* **129** (6), 2398 (1963).

[62] Electrically Induced Shifts of the GaAs Nuclear Spin Levels
K.A. Dumas, J.F. Soest, A. Sher, and E.M. Swiggard, *Phys. Rev. B* **20** (11), 4406 (1979).

[63] Spin Transitions Induced by External rf Electric Fields in GaAs
E. Brun, R. Hahn, W. Pierce, and W.H. Tantilla, *Phys. Rev. Lett.* **8** (9), 365 (1962).

[64] Nuclear Electric Quadrupole Induction of Atomic Polarization
T. Sleator, E.L. Hahn, M.B. Heaney, C. Hilbert, and J. Clarke, *Phys. Rev. Lett.* **57** (21), 2756 (1986).

[65] *Principles of Nuclear Magnetism*
A. Abragam, (Clarendon Press, Oxford, 1961).

[66] The Characteristics of Photoluminescence at a GaAs/AlGaAs Interface
Y.R. Yuan, J.L. Merz, and G.A. Vawter, *J. Lumin.* **40-1**, 755 (1988).

[67] Photoluminescence in Modulation-Doped GaAs/$Ga_{(1-x)}Al_xAs$ Heterojunctions
J.X. Shen, Y. Oka, C.Y. Hu, W. Ossau, G. Landwehr, K.J. Friedland, R. Hey, K. Ploog, and G. Weimann, *Phys. Rev. B* **59** (12), 8093 (1999).

[68] *Properties of Gallium Arsenide*
M.R. Brozel and G.E. Stillman, Third ed. (Inspec, The Institution of Electrical Engineers, London, 1996).

[69] *Handbook on Physical Properties of Ge, Si, GaAs and InP*
A. Dargys and J. Kundroths, (Science and Encyclopedia Publishers, Vilnius, 1994).

[70] Photoluminescence Related to the Interface of GaAs/(GaAl)As Heterojunctions
W. Ossau, E. Bangert, G. Landwehr, and W. Weimann, *J. Lumin.* **40-1**, 763 (1988).

[71] Vertical Transport of Photo-Excited Carriers for Excitonic Recombinations in Modulation Doped GaAs/$Ga_{(1-x)}Al_xAs$ Heterojunctions
J.X. Shen, Y. Oka, W. Ossau, G. Landwehr, K.J. Friedland, R. Hey, K. Ploog, and G. Weimann, *Solid State Commun.* **106** (8), 495 (1998).

[72] Theory of Transient Excitonic Optical Nonlinearities in Semiconductor Quantum-Well Structures
S. Schmitt-Rink, D.S. Chemla, and D.A.B. Miller, *Phys. Rev. B* **32** (10), 6601 (1985).

[73] High-Speed Optical Modulation with GaAs/GaAlAs Quantum Wells in a *p-i-n* Diode Structure
T.H. Wood, C.A. Burrus, D.A.B. Miller, D.S. Chemla, T.C. Damen, A.C. Gossard, and W. Wiegmann, *Appl. Phys. Lett.* **44** (1), 16 (1984).

[74] Band-Edge Electroabsorption in Quantum Well Structures: The Quantum-Confined Stark Effect
D.A.B. Miller, D.S. Chemla, T.C. Damen, A.C. Gossard, W. Wiegmann, T.H. Wood, and C.A. Burrus, *Phys. Rev. Lett.* **53** (2), 2173 (1984).

[75] Toward a Unified Theory of Urbach's Rule and Exponential Absorbtion Edges
J.D. Dow and D. Redfield, *Phys. Rev. B* **5** (2), 594 (1972).

[76] *Quantum Mechanics*
E. Merzbacher, Second ed. (Wiley, New York, 1970).

[77] *Quantum Chemistry and Molecular Spectroscopy*
C.E. Dykstra, (Prentice Hall, Englewood Cliffs, 1992).

[78] Resolved Free-Exciton Transitions in the Optical-Absorption Spectrum of GaAs
D.D. Sell, *Phys. Rev B* **6** (10), 3750 (1972).

[79] *Introduction to Solid State Physics*
C. Kittel, 5th ed. (Wiley, New York, 1976).

[80] Linear Stark Effect in Magnetic Resonance Spectra
N. Bloembergen, *Science* **133**, 1363 (1961).

[81] Shift of Nuclear Quadrupole Resonance Frequency by Electric Field
T. Kushida and S. Kuniomi, *Phys. Rev. Lett.* **7** (1), 9 (1961).

[82] Microscopic Interpretation of Optically Pumped NMR Signals in GaAs
C.R. Bowers, *Solid State NMR* **11** (1-2), 11 (1998).

[83] High-Resolution Spectroscopy of Individual Quantum Dots in Wells
D. Gammon, *MRS Bulletin* **23** (2), 44 (1998).

[84] Coherent Optical Control of the Quantum State of a Single Quantum Dot
N.H. Bonadeo, J. Erland, D. Gammon, D. Park, D.S. Katzer, and D.G. Steel, *Science* **282** (5393), 1473 (1998).

[85] Nonlinear Nano-Optics: Probing One Exciton at a Time
N.H. Bonadeo, G. Chen, D. Gammon, D.S. Katzer, D. Park, and D.G. Steel, *Phys. Rev. Lett.* **81** (13), 2759 (1998).

[86] Imaging Spectroscopy of Two-Dimensional Excitons in a Narrow GaAs/AlGaAs Quantum Well
Q. Wu, R.D. Grober, D. Gammon, and D.S. Katzer, *Phys. Rev. Lett.* **83** (13), 2652 (1999).

[87] Electrons in Artificial Atoms
D. Gammon, *Nature* **405** (6789), 899 (2000).

[88] Room-Temperature Spin Memory in Two-Dimensional Electron Gases
J.M. Kikkawa, I.P. Smorchkova, N. Samarth, and D.D. Awschalom, *Science* **277**, 1284 (1997).

[89] Resonant Spin Amplification in *n*-Type GaAs
J.M. Kikkawa and D.D. Awschalom, *Phys. Rev. Lett* **80** (19), 4313 (1998).

[90] Lateral Drag of Spin Coherence in Gallium Arsenide
J.M. Kikkawa and D.D. Awschalom, *Nature* **397**, 139 (1999).

[91] Electron Spin Coherence and Optical Coherence in Semiconductors
J.M. Kikkawa and D.D. Awschalom, *Phys. Today* **52** (6), 33 (1999).

[92] Coherent Transfer of Spin through a Semiconductor Heterointerface
I. Malajovich, J.M. Kikkawa, D.D. Awschalom, J.J. Berry, and N. Samarth, *Phys. Rev. Lett.* **84** (5), 1015 (2000).

[93] Resonant Amplification of Spin Transferred across a GaAs/ZnSe Interface
I. Malajovich, J.M. Kikkawa, D.D. Awschalom, J.J. Berry, and N. Samarth, *J. Appl. Phys.* **87** (9), 5073 (2000).

[94] Directly Detected Nuclear Magnetic Resonance of Optically Pumped GaAs Quantum Wells
S.E. Barrett, R. Tycko, L.N. Pfeiffer, and K.W. West, *Phys. Rev. Lett.* **72** (9), 1368 (1994).

[95] Ultraslow Electron Spin Dynamics in GaAs Quantum Wells Probed by Optically Pumped NMR
N.N. Kuzma, P. Khandelwal, S.E. Barrett, L.N. Pfeiffer, and K.W. West, *Science* **281** (5377), 686 (1998).

[96] *Quantum Mechanics, Volume 2*
C. Cohen-Tannoudji, B. Diu, and F. Laloë, (John Wiley & Sons, New York, 1977).

[97] *Physical Chemistry*
P. Atkins, 5th ed. (W.H. Freeman, New York, 1994).

[98] The Theory of Relaxation Processes
A.G. Redfield, *Adv. Magn. Reson.* **1**, 1 (1965).

[99] Line Shapes in High-Resolution NMR
R. Hoffman, *Adv. Magn. Reson.* **4**, 87 (1970).

[100] Dynamic Nuclear Polarization Near Defects in a GaAs/AlGaAs Heterojunction *in* Nuclear Magnetic Resonance Investigations in III-V Semiconductor Structures: Theory and Experiment
B.M. Lambert and D.P. Weitekamp, (unpublished).

[101] Nuclear-Spin Relaxation in AlGaAs/GaAs Heterostructures Observed via Optically Detected Magnetic Resonance (ODMR) Experiments
M. Schreiner, H. Pascher, G. Denninger, S.A. Studenikin, G. Weimann, and R. Losch, *Solid State Commun.* **102** (10), 715 (1997).

[102] *Principles of Magnetic Resonance*
C.P. Slichter, 3rd (Corrected 2nd Printing) ed. (Springer-Verlag, New York, 1992).

[103] Shedding Light on the Mechanism of All-Optical NMR
J.G. Kempf and D.P. Weitekamp, (unpublished).

[104] Electrically Induced Nuclear Quadrupole Spin Transitions in a GaAs Single Crystal
E. Brun, R.J. Mahler, H. Mahon, and W.L. Pierce, *Phys. Rev.* **129** (5), 1965 (1963).

[105] Detection of Two-Quantum Nuclear Coherence by Nuclear-Quadrupole-Induced Electric Polarization
D.C. Newitt and E.L. Hahn, *J. Magn. Res. Series A* **106**, 140 (1994).

[106] NMR Measurements of Homonuclear Indirect Couplings In GaAs
L.D. Potter and Y. Wu, *J. Magn. Reson. A* **116** (1), 107 (1995).

[107] *Angular Momentum*
D.M. Brink and G.R. Satchler, Third Ed. ed. (Oxford University Press, Oxford, 1993).

[108] Quantum Mechanics, Appendix II
C. Cohen-Tannoudji, B. Diu, and F. Laloë, (John Wiley & Sons, New York, 1977), Vol. 2, pp. 1468.

[109] *Classical Electrodynamics*
J.D. Jackson, (Wiley, New York, 1979).